J.W. van der Arend

Improving the anode subsystem water management of a PEM fuel cell system

A simulation study towards enhanced power density and lifetime

Improving the anode subsystem water management of a PEM fuel cell system

A simulation study towards enhanced power density and lifetime

By

J.W. van der Arend

in partial fulfilment of the requirements for the degree of

Master of Science
in Mechanical Engineering

at Delft University of Technology,
to be defended publicly on Tuesday August 14, 2023 at 10:00 AM.

Thesis committee:	Prof. dr. ir. W. de Jong	
	Dr. ir. L. van Biert	
	Dr. ing. S. Bohatsch	PowerCell Group

Abstract

The increasing awareness and urgency of climate change have led to an increase in investments and research into power sources not reliant on fossil fuels. Proton exchange membrane (PEM) fuel cells are a promising technology for automotive, maritime, and auxiliary power applications converting chemical energy into electricity. In order for this upcoming technology to compete with well-established alternatives such as diesel generators and combustion engines, it is of vital importance to improve the power density and durability.

PEM fuel cells produce water and heat during operation. The presence of superfluous liquid water in the fuel cell stack gives rise to flooding of the electrodes, which hampers operation and induces degradation processes. On the other hand, it is of great importance to maintain a high membrane humidification to reduce Ohmic losses over the membranes and avoid the formation of cracks. Therefore, water management plays a vital role both in maintaining the power density and guaranteeing durability.

This thesis is written under the auspices of both TU Delft and PowerCell Group, a manufacturer of PEM fuel cell systems located in Gothenburg, Sweden. Currently, a substantial amount of water condenses in the anode subsystem of PowerCell's PEM fuel cells in certain operating ranges which subsequently enters the fuel cell stack. This study identifies the influence of certain system operating parameters on responses as the water crossover through the membranes, the relative humidity at the stack inlet, the temperature at the inlet of the stack, the condensation rate in the mixing chamber of the recirculation loop, and the mass flow rates of liquid water and water vapor in and out of the stack. Multiphysics simulation software provided by Gamma technologies is used to simulate 5600 operating points in which the system operating parameters are varied according to the Latin Hypercube sampling method. These simulations give a clear overview of the influence of the operating parameters on the aforementioned responses over the entire operating range of PowerCell's PS-100 system.

The simulated experiments are subsequently used as a basis to construct metamodels. These metamodels predict the behavior of the system based on the operating parameters varied in the 5600 simulations. The metamodels are constructed both as Krigings and as multilayer perceptrons (MLPs). Kriging is a statistical method which produces an output for a certain response based on known input data where input points which resemble the unknown point are given a greater weight. MLPs are neural networks which recognise patterns in input data and use those to predict an output for a certain response. Finally, the operating parameters are optimized using the metamodels to minimize the liquid water mass flow rate into the stack, to prevent condensation in the mixing chamber of the anode subsystem, and to target a certain inlet relative humidity of the hydrogen feed to the stack. Concluding from these optimizations it would be beneficial to preheat the hydrogen before it reaches the mixing chamber. A number of alternative designs for the anode loop are proposed in which the findings from the simulation study are considered which require further investigation.

List of Contents

Nomenclature

MEA – Membrane electrode assembly
NWTC – Net water transport coefficient
PEMFC – Proton exchange membrane fuel cell
GDL – Gas diffusion layer
DoE – Design of experiments

List of figures

List of tables

1 Introduction

The 19th century was an era of rapid advancement in natural sciences. A plethora of natural phenomena were discovered and documented. At the dawn of the century, in 1800, the process of decomposing water into hydrogen and oxygen by means of an electric current (electrolysis) was discovered by William Nicholson and Anthony Carlisle. Some decades later, in 1838, reverse electrolysis was discovered by Christian Friedrich Schönbein [1]. In 1842, a Welsh lawyer named William Grove developed a device based on Schönbein's research [2]. Grove's device delivered an electric current and produced water while consuming hydrogen and oxygen. In essence, it was a gas battery in which two platinum electrodes were emerged in nitric acid on one end, while the other ends were kept in sealed oxygen and hydrogen containers. However primitive, Grove's gas battery was the first device which could be referred to as what today is known as a fuel cell. An application was found in powering the upcoming telegraphing industry. This was short-lived as it turned out that Grove cells produced nitrogen dioxide, a poisonous gas which presented an occupational hazard for the telegraph operators.

During the second half of the 19th century, various scientists launched competing theories to explain the physics and chemistry behind Grove's gas battery. It was Friedrich Wilhelm Ostwald [3], who in 1893, finally laid the foundations for the science of electrochemistry in when he experimentally demonstrated the purpose of various fuel cells components, such as the electrodes and the electrolyte.

For a long time, fuel cells remained an academic curiosity for which no practical application could be found. The space race between the United States of America and the Soviet Union changed that. Fuel cells, manufactured by General Electric, [4] found their first practical application in NASA's early to mid-60s Gemini project. During 1965 and 1966 ten manned flights were undertaken in an orbit around planet earth. The concept of NASA's fuel cell had been conceived in the late 1950s by W. Thomas Grubb and Leonard Niedrach, two General Electric chemists. In this type of fuel cell, the proton exchange membrane fuel cell (PEMFC), a membrane capable of transporting protons acted as the electrolyte [5]. The fuel cells in the Gemini project were used as auxiliary power supply units for the space craft and their supporting satellites and probes. Later, fuel cells were also used during the Apollo programme in which mankind first set foot on the moon [6], and the space shuttle programme [7].

The threat of climate change has sparked an interest in fuel cells outside the field of space flight. Nowadays, the main applications for PEM fuel cells are in transportation and auxiliary power. PEM fuel cells distinguish themselves from other types of fuel cells through a low operating temperature (60-80 ºC), high power density, and scalability. [8] The need for auxiliary power sources and power trains in automotive, maritime, and aviation applications with a small carbon footprint, has led to a growing fuel cell industry which originated in the early 1990s. A major technological advancement in PEM fuel cells, was the reduced platinum use in the manufacturing of catalysts in the late 1990s. This has stimulated the commercialization of PEM fuel cells in the early 21st century. [9]

PowerCell Group, located in Gothenburg, is a company which is active in the PEM fuel cell industry. The company offers stationary power systems, including the PS100 and the PS200 which deliver up to 100 kW and 200 kW, respectively. The core component of these systems is the fuel cell stack. Furthermore, the systems consist of components which allow the fuel cell stack to operate and to harvest the generated power by the stack. These components constitute the cooling loop, the anode loop, the cathode loop, and power electronics.

During operation of a PEM fuel cell system, water and heat are produced at the cathodes of the cells in the stack. Some of the water crosses over through the membranes to the anode side of the stack. The power density and durability of PEM fuel cell stacks are sensitive to the degree of humidity in the membranes. A sufficiently and evenly humidified anode improves the life span of the fuel cell stack and enables stable operation. A sufficient amount of water vapour in the anode loop is vital in hydrating the anode side of the membranes. When water vapour condenses in the loop and enters the stack, the pathways to the catalyst sites in the electrodes can be blocked. This phenomenon is referred to as flooding. Liquid water fills the voids in the porous electrodes and gas flow channels and prevents the reactants from reaching the catalyst sites. Flooding can also occur as a consequence of insufficient draining of water from the stack. A consequence of flooding is reactant starvation at the catalyst sites. This negatively affects the power density and can lead to permanent damage of the electrode through carbon corrosion. This occurs when the carbon backbone of electrodes react with water to carbon dioxide, protons, and electrons. Electrolysis of the water occurs simultaneously as well in this process. The oxygen produced in electrolysis of water and oxygen crossover from the cathode to the anode, exacerbates the flooding as it reacts with hydrogen and forms additional water. These processes lead to a reverse current in the affected cells. In conclusion, sound water management of the anode loop entails maintaining a sufficiently high relative humidity of the hydrogen fed to the stack while minimizing condensation. This can be attained by properly managing the auxiliary components in the anode loop.

Currently, a high degree of liquid water entering the stack in the anode loop of PowerCell’s PS100 systems is a problem that should be resolved. A significant amount of liquid water accumulates in the gas flow channels on the anode side of the cells. The aim of the research conducted in this thesis is to propose a range of suitable operating parameters of the auxiliary components in the anode loop of the PS100 system to resolve this issue over the full operating range. Proper management of the auxiliary subsystems guaranteed high-efficiency operation of the stack and durability. The anode loop of the PS100 will be modelled in a simulation study in GT-Suite. If necessary, design modifications to the anode loop will be proposed to attain said operating parameters. The rate of water crossover to the anode and condensation of water in the anode loop are also influenced by the material properties of the membranes and electrodes. The scope of this thesis will however be limited to improving the operating parameters of the system given the current membrane electrode assembly (MEA).

Research question

In pursuit of improving the water management of the anode loop of the PS100, the following research question needs to be answered:

“How can modifications to the operating parameters and design of the PS100 system´s anode subsystem, improve water management, maintain the stack’s power density, and prolong its lifetime? “

In order to answer the main research question, the following sub questions have been formulated which consider the anode loop water management from multiple angles:

1. *“What transport mechanisms of water crossover across the membrane are dominant, and how are they affected by the system and stack operating parameters? “*
2. *“What are the effects of the water content and phase composition in different parts of the stack on its power density and lifetime? “*
3. *“How can the water crossover across the membrane be modelled accurately?”*
4. *“How can the auxiliary components be used to maintain an adequate humidity and prevent condensation in the anode loop? “*

5. *“What are the optimal operational parameters of the auxiliary components regarding the water management of the anode loop over the full operational range?”*
6. *“Which modifications are required in the anode loop design?”*

Structure

This thesis is divided into two constituent parts. First of all, a literature study will be conducted in which the system set-up, general electrochemical concepts, and theory relevant to the sub-questions will be lined out. Chapter 2 of the literature study outlines the subsystems of a PEM fuel cell system and gives an overview of the essential auxiliary components in the anode subsystem. Chapter 3 touches upon the anatomy of a PEM fuel cell stack. Chapter 4 of the literature review dives into the electrochemical and thermodynamic theory relevant to the performance and degradation mechanisms occurring in a PEM fuel cell stack. Finally, chapter 5 discusses the water transport mechanisms across the membrane and several experimental models attempting to quantify them.

After this initial stage, a simulation study in GT-Suite will be carried out. The effect of the system operating parameters on the water crossover, the relative humidity at the anode inlet of the stack, the mass flow rate of liquid water at the stack inlet, the condensation rate in the mixing chamber and other responses is investigated in this simulation study. The methodology of modelling the stack and the anode subsystem will be presented in chapter 6 and 7. In chapter 8 and 9 the results of the simulation study are exhibited. A discussion regarding the methodology and results are included in chapter 10. At last, the conclusions of this thesis are presented in chapter 11. This chapter furthermore includes recommendations for further study.

I

Literature Review

2 System definition and description

In this opening chapter of the literature review, a concise overview of the subsystems of a PEM fuel cell system will be given. A PEM fuel cell system can be divided into a cathode, anode, cooling, and electrical subsystem. In figure 1, the connections between the components of the subsystems are represented by blue, purple, green, and red arrows. The connections between the components of the cathode subsystem are depicted with blue arrows. The purple arrows represent the electrical connection between the load and the stack. The green arrows represent the connections between the components of the cooling loop. Finally, the red arrows connect the components of the anode loop.

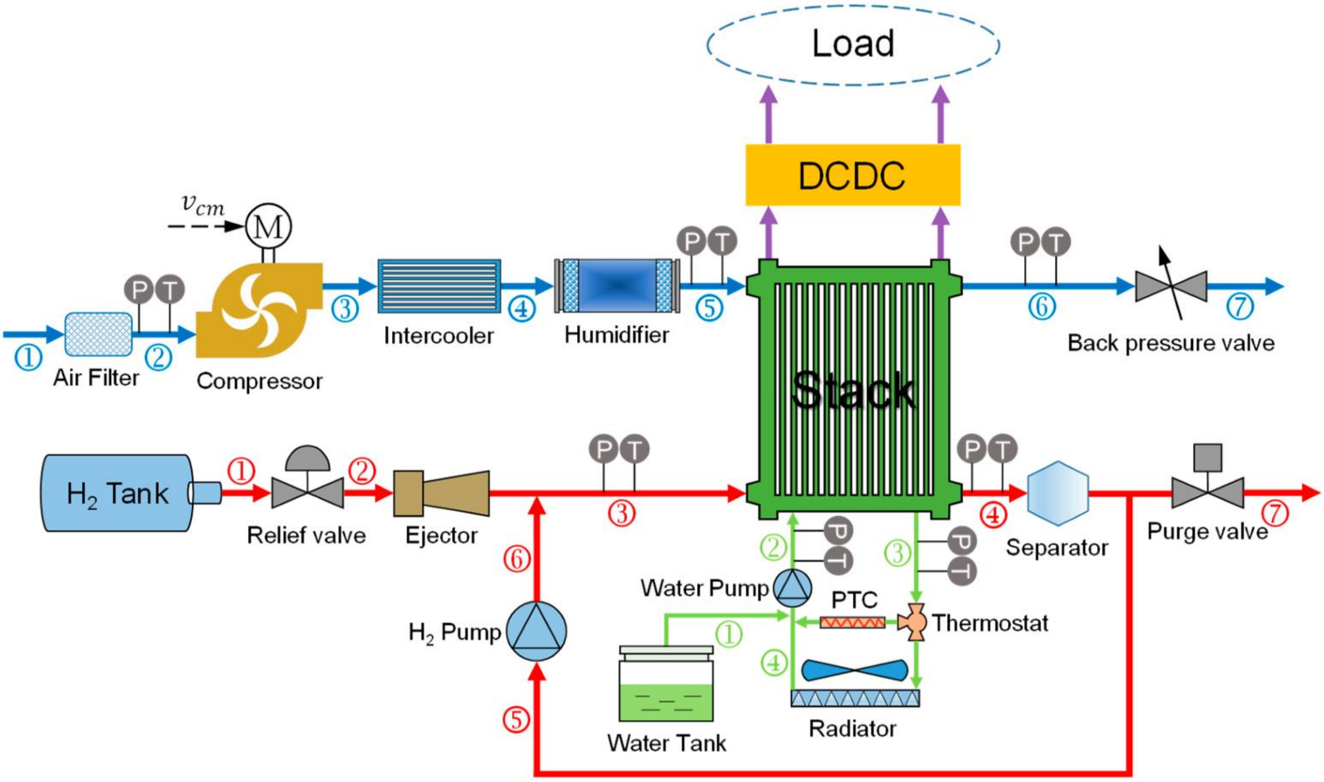

Figure 2.1: Schematic overview of a PEM fuel cell system [10]

The combined task of the components of the cathode subsystem is to feed air to the stack at a certain pressure, temperature, and humidity. The cooling loop maintains the stack temperature in an acceptable range. The main function of the anode subsystem is to feed hydrogen to the stack at a certain pressure, temperature, and humidity. As the scope of this thesis is limited to the water management of the anode subsystem, the functioning of its components will now be elaborated on. It should be noted however, that regarding water mass transfer phenomena, the anode subsystem does not operate as an isolated system. The other subsystems influence the water mass transfer processes in the anode subsystem through the physical subsystem boundaries which meet in the stack.

A well-designed and operated anode subsystem prevents hydrogen starvation in the stack and facilitates suitable conditions to limit stack degradation processes to a minimum. Ideally, the components comprising the anode subsystem are few in number, economical, and robust. [11]

Hydrogen supply

Hydrogen can be supplied to a PEM fuel cell system from various sources. In practice, hydrogen in commonly fed from storage tanks at high pressure as displayed in figure 2.1. The hydrogen is brought to a lower pressure by a relief valve and subsequently fed to the stack at the desired pressure. This valve controls the mass flow rate of hydrogen into the system.

Anode subsystem configurations

The anode subsystem can exist in four different configurations depending on the presence of a hydrogen recirculation loop. [12] The example anode subsystem in figure 2.1, is a subsystem containing a recirculation loop powered by a hydrogen compressor and ejector. Besides this set-up with a hybrid recirculation loop, recirculation loops can also solely be powered by either an ejector or pump. Finally, it is also possible for an anode subsystem to operate in a dead-end configuration in which no hydrogen is recirculated. These configurations will now shortly be discussed.

Dead-end configuration

In the dead-end configuration no hydrogen is recirculated. Hydrogen is fed to the stack at a certain pressure through a pressure regulating valve and an injector valve. (Figure 2.2) Periodically, a purge valve is opened in order to evacuate water and nitrogen which have crossed over from the cathode in the stack. When the purge valve is opened, the resulting pressure drop forces water, nitrogen, and hydrogen out of the gas flow channels of the stack. By increasing the hydrogen speed, the extent to which nitrogen and water can be forced out of the gas flow channels increases. This will also increase the loss of hydrogen in the purging moments, however.

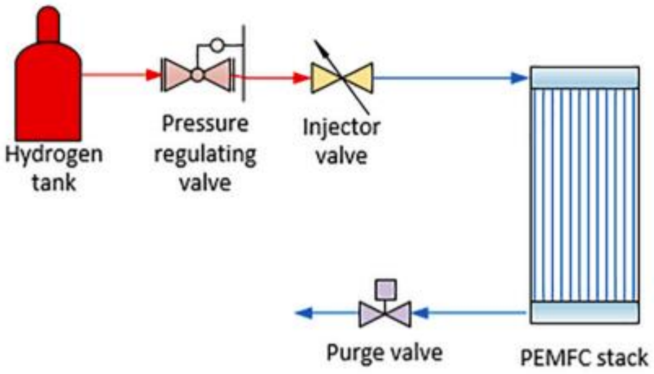

(a) Dead-end anode

Figure 2.2: Anode subsystem in dead-end configuration [12]

The dead-end anode subsystem contains the least components out of the four configurations. Its simplicity is the main reason to opt for this set-up. The main challenges of the dead-end configuration are achieving an equal mass flow rate of hydrogen in every cell and the loss of hydrogen in the purging intervals. It is therefore not suitable for higher systems in which the stack contains a great number of cells. [11]

Anode subsystem with recirculation loop

A hydrogen recirculation loop can be incorporated in the anode subsystem to prevent hydrogen waste, to increase the system efficiency and to achieve an even reactant distribution in the stack.

For high power applications an excess supply of hydrogen is required to avoid hydrogen starvation at the electrodes. [12] Three anode subsystem configurations containing a hydrogen recirculation loop can be distinguished. The hydrogen which hasn't partaken in the electrochemical reaction in the stack can be recirculated by either a pump, an ejector, or a combination of both as shown in figure 2.1. Furthermore, a pump can be used to increase the velocity of the hydrogen in the anode flow channels to force liquid water out of them. An added benefit of a recirculation subsystem is that water which has crossed over the membrane from the cathode will be recycled as well and aids in humidifying the membrane. This eliminates the need for a humidifier in the anode structure. A vapor-liquid separator is placed after the stack to remove liquid water from the recirculation loop. (Figure 2.1)

Nitrogen which crosses over from the cathode to the anode will also be recirculated. Therefore, a purge valve which prevents the build-up of nitrogen in the recirculation loop is also an essential component of these anode subsystems. A build-up of nitrogen in the stack prevents the hydrogen from accessing the reaction sites. This is noticeable through a drop in the cell voltage. A certain nitrogen fraction in the recirculated flow is also favorable as it aids in pushing out liquid water of the stack. When the purge valve is opened hydrogen is lost as well. In a sound purging strategy, the purge valve is only opened when a drop in the cell voltage due to a build-up of nitrogen is measured. [11]

Recirculation loop powered by a pump

The most conventional anode subsystem including a recirculation loop, is the pump-powered variant. In this configuration, a pump is located between the vapor-liquid separator and the mixing chamber where newly introduced and recirculated hydrogen meet, as shown in figure 2.3. This pump provides momentum to the hydrogen which hasn't taken part in the electrochemical reaction in the stack to transport it to the mixing chamber. Various types of pumps have been applied in PEM fuel cell systems. These include roots, scroll, centrifugal and regenerative pumps.

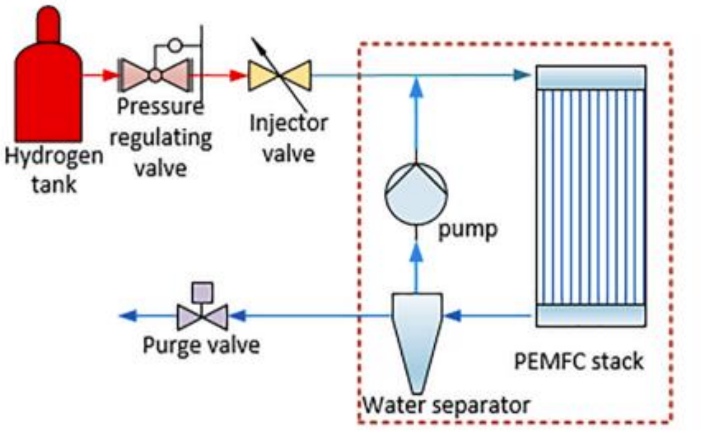

Figure 2.3: Anode loop with pump recirculation subsystem [12]

The characteristics of the aforementioned pumps will not be considered in depth as the type of pump does not significantly influence the water management of the anode subsystem. It is worth mentioning that the main requirement on pumps used in PEM fuel cell systems are low levels of vibrations, and the absence of lubrication oil as contaminants in the hydrogen flow would damage the stack. Although pumps can be easily controlled to operate at any mass flow rate, the drawback is the parasitic power consumption which lowers the system efficiency.

Recirculation loop powered by an ejector

The downside of parasitic power consumption associated with the integration of a pump in the recirculation loop, has led to a quest for alternative power sources. Ejector-based recirculation loops have therefore received widespread attention in the last two decades. Two major advantages of ejector-based recirculation loops over recirculation loops relying on pumps, are the absence of a parasitic power loss and the low capital costs of integration. The ejector consists of a mixing chamber and a diffuser. The flows entering the ejector come from the hydrogen storage tank and the vapor-liquid (water) separator. (Figure 2.4)

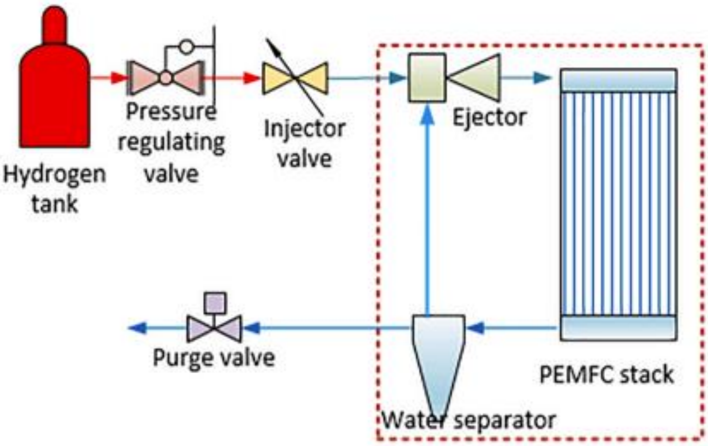

Figure 2.4: Anode loop with ejector recirculation subsystem [12]

In the ejector, a flow at high velocity entrains a flow at a lower velocity. In the case of the integration in an anode subsystem, the flow at low velocity is the hydrogen feed from the hydrogen storage tank, whereas the recirculated hydrogen enters the ejector at a relatively high velocity.

The geometry of the ejector determines the degree to which entrainment of the recirculated hydrogen is successful. Due to the wide operational range of a PEM fuel cell system, it is difficult to design an ejector which successfully entrains the recirculated hydrogen over the entire range of operating points.

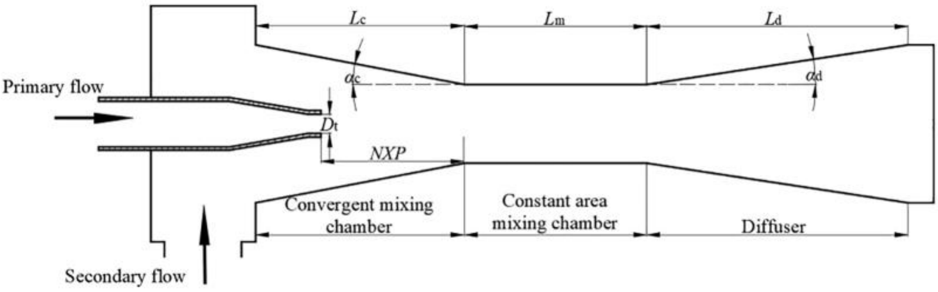

Figure 2.5: Cross-section of an ejector [12]

In figure 2.5, a cross-section of an ejector as used in the recirculation loop is shown for further illustration. The primary flow, which is the hydrogen feed, enters the ejector through a nozzle. The velocity of the hydrogen feed increases as the diameter of the nozzle decreases to D_t. The secondary flow which consists of recirculated hydrogen, water vapor and nitrogen is entrained by the primary flow due to the shear force of the primary flow at high velocity. The primary and secondary flow are subsequently mixed in the convergent mixing chamber and in the mixing chamber of constant diameter. In the diffuser the pressure of the mixed flow increases due to the increasing diameter.

The entrainment performance of an ejector depends on its geometrical parameters such as the diameter of the primary nozzle outlet D_t, the distance of the primary nozzle outlet to the mixing chamber NXP, the lengths of the mixing chambers l_c, l_m and the diffuser l_d, and the angles of the convergent mixing chamber α_c and diffuser α_d.

As mentioned, it is difficult to design an ejector which successfully entrains the recirculated hydrogen over the entire operating range of a PEM fuel cell system. In case the system is operated at low power, the hydrogen feed enters the ejector at too low a velocity to successfully entrain the recirculated hydrogen. The performance of an ejector is measured by the ejector efficiency R_{ej}. This measure represents the range of system operating points in which the ejector can successfully entrain the recirculated hydrogen.

$$R_{ej} = \frac{P_{max} - P_{min}}{P_{min}} \qquad (2\text{-}1)$$

In equation (2-1), P_{max} is the maximum power at which the PEM fuel cell system can be operated. P_{min} is the minimum power at which the primary flow is able to entrain the secondary flow. In experimental set-ups a range of 65-80% has been achieved. In practice, a range of 90-95% is desirable in PEM fuel cell systems. There has been ongoing research to improve the entrainment performance of ejectors. [12] A short-term solution would be a hybrid PEM fuel cell system incorporating a battery which would be activated at lower power demands. [11]

Ejectors have a long tradition of application in refrigeration systems. The application of ejectors in PEM fuel cell systems is a novelty, however. When applied in PEM fuel cell systems, the secondary flow has different characteristics compared to those encountered in refrigeration systems. First of all, the secondary flow in PEM fuel cell systems consists of multiple components, namely hydrogen, nitrogen, and water. Secondly, water can manifest itself both in the vapor and the liquid phase. Consequently, several CFD models have been proposed specifically for multiphase flows in ejectors in PEM fuel cell systems. [13] The main conclusion was that the degree of entrainment of the secondary flow is lower in case of a two-phase flow compared to the case of a single-phase secondary flow. Furthermore, condensation occurred mostly around the nozzle outlet of the primary flow.

Wang et al. [13] conducted experiments monitoring the condensation of water vapor in the secondary flow upon entrainment in an ejector by the primary flow. When the primary flow was fed at low temperature, condensation upon entrainment increased with an increasing fraction of water vapor in the secondary flow. Little literature about phase change and two-phase flows in ejectors is available as of yet. The behavior of two-phase flows and phase change in ejectors require more thorough analysis.

Water separator in the recirculation loop

A vital component of an anode subsystem with a recirculation loop is the vapor-liquid separator located after the stack. This component is also referred to as a water separator (Figures 2.1,2.3 & 2.4) or water trap. A certain fraction of the water leaving the stack is in the liquid phase. Furthermore, some water vapor will condense in the piping between the anode outlet of the stack and the water separator. It is vital to remove liquid water out of the recirculation loop before it can reach the pump or ejector. Liquid water can hamper the operation of the pump or ejector. Further downstream, liquid water would enter the stack after mixing with newly introduced hydrogen in the mixing chamber. Failing to prevent this would lead to flooding of the stack on the anode side of the cells. Various types of water separators are applied in the recirculation loops of PEM fuel cell systems to remove liquid water from the recirculation loop. Gravity settling, cyclone, baffle vane and wire mesh separators are among the alternatives used. These separators have varying pressure drops and separation efficiencies.

In figure 2.6, a schematic overview of the water separators applied in anode recirculation loops has been provided. The working principle of each water separator shown in figure 2.6 will be briefly clarified. In a gravity settling vapor-gas separator, the difference in density between water in the vapor phase and liquid phase is harnessed to separate the phases as portrayed in figure 2.6a. Liquid water collects at the bottom of the separator, whereas other phases leave through the top. In a corrugated plate water separator, liquid water settles on the surface of the plates when a two-phase flow passes through them. (Figure 2.6b) This type of separator can handle a large flow rate while the pressure drop is low. Small droplets tend to pass through a corrugated plate separator, however. In a cyclone separator, gaseous phases and liquid water are separated by centrifugal force. (Figure 2.6c) The separation efficiency of a cyclone separator is affected by the liquid fraction and the velocity of the inlet flow. The swirl tube (Figure 2.6d) separates liquid water from the flow by inducing a rotational motion through the swirl vane. Gaseous phases more or less maintain the axial direction, whereas liquid water is separated through an outlet in the pipe wall. The filter (Figure 2.6e) presents a physical barrier for liquid water. The separation efficiency and pressure drop are affected by the filter material and construction of the filter element.

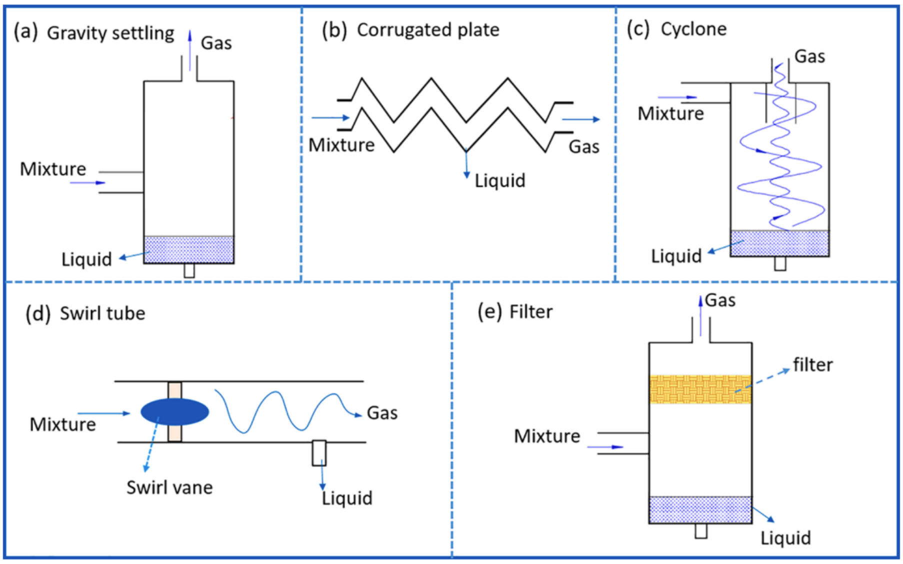

Figure 2.6: Overview of water separators applied in PEM fuel cell systems [12]

The water separators shown in figure 2.6 are compared in table 2.1. They are compared based on their separation efficiency, pressure drop, size, and durability.

Table 2.1: Comparison of vapor-liquid separators applied in PEMFC systems [12]

Type	**Separation efficiency**	**Pressure drop**	**Size**	**Durability**
Gravity settling	★	★ ★ ★	★	★ ★ ★
Corrugated plate separator	★ ★	★ ★	★ ★	★ ★ ★
Cyclone	★ ★	★ ★	★ ★ ★	★ ★ ★
Swirl tube	★ ★	★ ★	★ ★ ★	★ ★
Filter	★ ★ ★	★	★ ★ ★	★

3 Anatomy of a PEM fuel cell stack

This chapter serves to explain the functioning of a PEM fuel cell stack, the core component of a PEMFC system. A PEMFC stack, like PowerCell's P-stack, consists of adjacent individual galvanic cells which are connected in series (Figure 3.1). As the cells are connected in series, the voltages add up while the current through each cell is equal. Every single cell consists of a membrane electrode assembly (MEA) which is wedged between two bipolar plates. The stack is constructed out of a repeating pattern of cells and bipolar plates, with two one-sided bipolar plates at both ends. [8] The individual cells of the P-stack are held in place by steel strapping. The individual galvanic cells of a PEM fuel cell, its subcomponents in the MEA, and the bipolar plates will be elaborated upon in this chapter.

Figure 3.1: PowerCell's P-stack contains hundreds of individual galvanic cells connected in series [14]

Galvanic cells in a PEMFC stack

Each individual galvanic cell in a PEMFC stack is capable of generating a current from a spontaneous redox reaction. The cells consist of a membrane, a positive electrode (cathode), a negative electrode (anode), gas flow channels for the supply of reactants and the disposal of products, and collector plates which allow the flow of electrons released in the electrochemical reaction through an external circuit. The membrane and the electrodes are often collectively referred to as the membrane electrode assembly (MEA).

In the electrochemical reaction which takes place in the galvanic cells, electrons are transferred from a reductant to an oxidant. In a PEMFC, hydrogen is the reductant and oxygen is the oxidant. The reaction takes place at the surface of catalyst sites of physically separated electrodes in the form of two half-reactions. In addition to catalysing the half-cell reactions, the function of electrodes is to conduct electrons towards the current collectors, and to provide a pathway for reactants and products. The reaction is schematically depicted in figure 3.2. [9]

Through the anode gas flow channels, hydrogen is supplied to the galvanic cell. The hydrogen molecules are subsequently stripped from their electrons at the catalyst sites, which are in turn transported to the cathode through an external circuit. This transport of electrons can be harnessed as a source of useful work. The potential difference stemming from the transport of electrons gives rise to an ionic current (H^+) through the membrane from the anode to the cathode aiming to restore the charge balance.

The oxidation of hydrogen which occurs at the anodic catalyst sites of a PEMFC is described by the following chemical equation:

$$H_2 \rightarrow 2H^+ + 2e^- \tag{3-1}$$

The electrons and protons originating from the anodic half-cell reaction, react with oxygen supplied to the cathodic catalyst sites to produce water and heat according to the following chemical equation:

$$O_2 + 4H^+ + 4e^- \rightarrow 2H_2O \tag{3-2}$$

Recombining the half-cell reactions (3-1), (3-2) gives rise to the following overall chemical equation:

$$2H_2 + O_2 \rightarrow 2H_2O \tag{3-3}$$

The overall chemical reaction (3-3) is exothermal. This means waste heat is produced during operation of a fuel cell. The higher heating value of the overall reaction, corresponds to the heat of formation of water at 298.15 K. At said temperature and atmospheric pressure, this is equal to 286 KJ/mol [9]. This corresponds to the heat produced when hydrogen is combusted to form only liquid water. The heat produced in a fuel cell depends on the temperature at which the reaction occurs and whether the product water is in the liquid or the vapor phase.

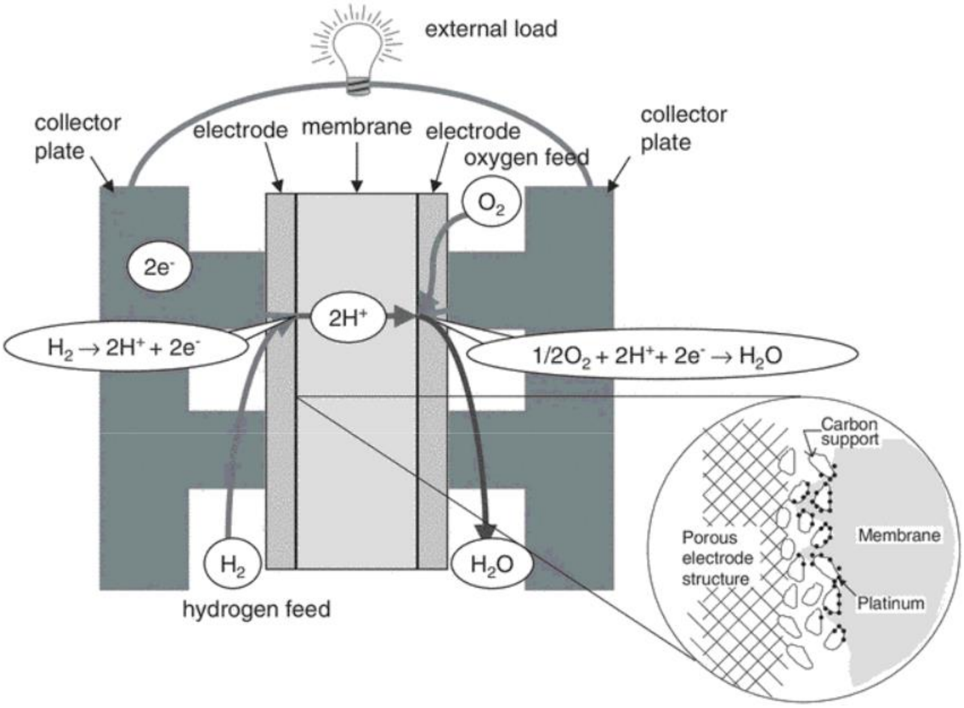

Figure 3.2: Top view of an individual cell in a PEMFC including schematic depiction of the reaction [9]

Membrane electrode assembly

As mentioned before, the electrodes and the membrane of the cells in a PEMFC stack are collectively referred to as the MEA. The membrane and electrodes are inseparable as a result of their manufacturing process. The MEA could be considered the core component of the galvanic cell as it allows the overall electrochemical reaction to take place at physically separated electrodes. As shown in figure 3.2, the membrane is sandwiched between the two electrodes. First, the purpose and the structure of the membrane will be discussed.

Functions and structure of the membrane

The membrane in a PEM fuel cell has three main functions. First of all, the membrane is a conductor of protons and as such, enables passage of protons stemming from the anodic half-reaction to the cathodic catalyst sites. In addition, the membrane is an electric insulator. In this capacity it prevents a short circuit, electrons are forced to travel between the electrodes through an external circuit. Finally, the membrane acts as a barrier to prevent oxygen and hydrogen from mixing. [9]

The membrane consist of a carbon backbone which is hydrophobic. Sulfonic acid groups ($SO_3^-H^+$) are attached to the carbon backbone as side chains (Figure 3.3). The carbon backbone, which often is a Teflon-like material, provides mechanical strength to the membrane. A material which was originally commonly used in membranes is Nafion. This is a brand name for a tetrafluoroethylene-based fluoropolymer-copolymer [15]. The sulfonic acid groups provide locations for proton transfer and are hydrophilic. As a result of the hydrophilic nature of the sulfonic acid groups, the membrane can absorb up to 50% of its weight in water. [9] The hydrated regions of the membrane allow for transport of protons.

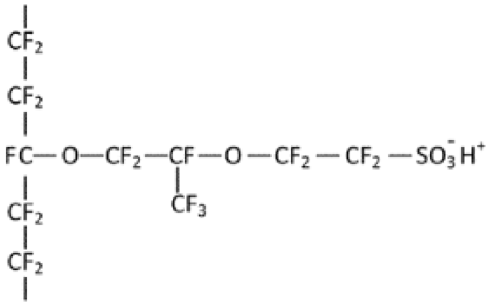

Figure 3.3: Structure of a Nafion polymer [16]

The material structure and the water content of the membrane determine the protonic conductivity of the membrane. A common way of expressing the water content of a membrane, is the number of water molecules absorbed per sulfonic acid group λ. In the liquid phase a Nafion membrane can absorb up to 22 molecules per sulfonic acid group. In the vapour phase this is reduced to 14 molecules per sulfonic acid group [17]. This phenomenon is referred to as Schroeder's paradox.

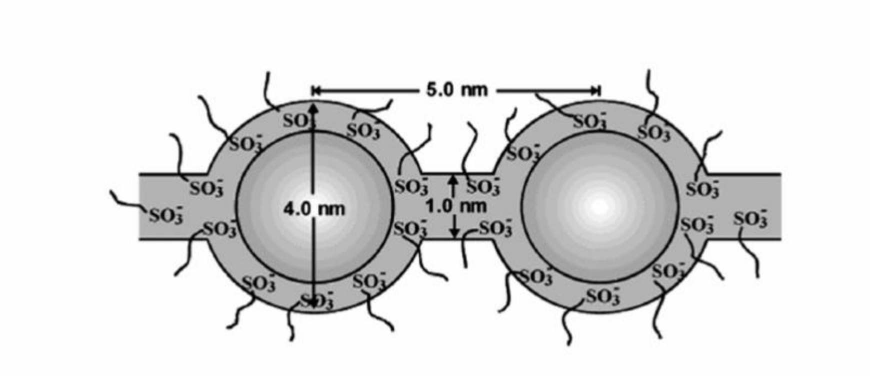

Figure 3.4: The structure of a hydrated Nafion strain [18][19]

Based on experiments conducted at Los Alamos National Laboratory, Zawodzinski [20] defined a relationship between the water content of a membrane and the water activity a. The water activity is given by the following relation:

$$a = \frac{p}{p^*} \tag{3-4}$$

In relation (3-4), p is the partial water vapour pressure at the surface of the membrane on the cathode side, and p^* the partial vapour pressure of pure water at the same temperature.The water activity can be assumed to be equal to the relative humidity on the cathode side face of the membrane if water is considered to be an ideal gas. The water content λ is expressed as:

$$\lambda = 0.043 + 17.18a - 39.85\, a^2 + 36\, a^3 \qquad (3\text{-}5)$$

The process of water absorption by a Nafion membrane was described by Weber and Newman [9]. Four steps can be distinguished in the process:

1. Water is absorbed by a previously dry membrane. The membrane's sulfonic acid groups are solvated in course. In this phase strong bonds between the sulfonic acid groups and the water molecules are formed.
2. When more water is absorbed, the bonds between the water molecules and sulfonic acid groups are loosened. This causes the hydrophobic carbon backbone to reform itself and encapsulate the water molecules as shown in figure 3.4. This phenomenon occurs due to the hydrophobic nature of the fluoro-carbon rich skin of the ionomer (CF_2 and CF_3) and the hydrophilic nature of the sulfonic acid groups.
3. The next step is the formation of an interconnected network of Nafion structures which encapsulate water molecules. A cluster-channel network starts to form.
4. When every sulfonic acid group is connected to two water molecules ($\lambda = 2$), a continuous path of clusters has been formed in the membrane. A greater uptake of water molecules increases the interconnectivity.

The structure of a dry Nafion membrane is depicted in figure 3.5a. A membrane which has absorbed some water but does not form interconnected clusters can be seen in figure 3.5b. Finally, a completely hydrated membrane surrounded by water in the vapour phase and liquid water is depicted in figure 3.5c and figure 3.5d respectively. When a membrane is saturated, its dimensions can increase up to 10% compared to the dry state.

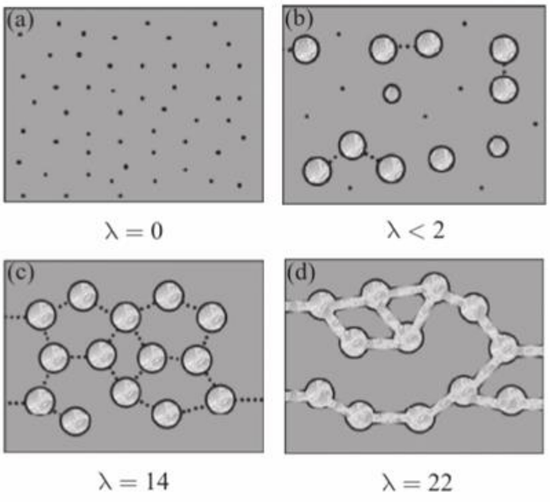

Figure 3.5: (a) a dry membrane, (b) a somewhat hydrated membrane without interconnected Nafion strains, (c) a fully hydrated membrane with water in the vapor phase, (d) membrane fully hydrated with liquid water [21]

The proton conductivity of a Nafion membrane is strongly influenced by its water content. This in turn implies that the ohmic losses over the membrane are strongly influenced water content. Besides the water content and the structure of the membrane, the conductivity is also influenced by the temperature of the cell. Springer defined the following relation for the protonic conductivity of a Nafion 117 membrane as a function of the water content of the membrane, and the cell temperature. [13]

$$\kappa_{\text{proton}} = (0.005139\lambda - 0.00326)\exp\left[1268\left(\frac{1}{303} - \frac{1}{T_{cell}}\right)\right] \quad (3\text{-}6)$$

In relation (3-6), λ is the water content of the membrane and T_{cell} is the cell temperature in Kelvin.

Nafion 117 is a membrane which has a thickness of 175 µm. [13] Since the early 1990s, membranes have dramatically decreased in thickness. State-of-the-art membranes have a thickness of around 15 µm. As a consequence, they require a reinforcement structure in the centre to guarantee structural integrity. The rationale for decreasing the membrane thickness has been a lower Ohmic resistance. These reinforced membranes display higher strength, lower gas permeability, and better dimensional stability than their non-reinforced counterparts. [22]

Structure of the electrodes

Now the subcomponents of the electrodes which are attached to the membrane on both sides will be elaborated on. The electrodes comprise of three layers: the catalyst layer, the microporous layer, and the gas diffusion layer (GDL), respectively. The catalyst layer is the layer adjacent to the membrane. The layers which constitute the electrodes have various functions which will be detailed. One common characteristic of all layers is that the materials are porous in order to provide a pathway for the reactant gases to the reaction sites. These pathways also allow for product water to be removed. If there is an excess of liquid water in the pores, reactant gases are inhibited from reaching reaction sites in the electrodes. This phenomenon is known as flooding of the electrodes.

Catalyst layer

On both sides of the membrane a catalyst layer is applied through a coating process, which comprises of platinum particles supported by a carbon backbone. The catalyst layer is the zone of the electrode where the half-reactions occur. The particles that catalyse the reactions in both the anode and cathode catalyst layers are usually platinum particles. These particles lower the activation energy of the half-reactions, causing them to proceed at a much higher rate. Contact between three phases is required for a half-reaction to occur. [16] At the reaction sites hydrogen or oxygen meet with a solid phase which conducts electrons, and the electrolyte which conducts ions. The catalyst layers' proton conductivity is determined by the water content of the ionomer which extends from the membrane. This region of contact in the catalyst later is called the three-phase boundary. [16] At the surface of platinum particles in the anode catalyst layer, hydrogen is stripped from its electrons. The remaining protons are subsequently transported to the cathode over the membrane. The electrons are transported to the cathode through the external circuit. At the cathode catalyst layer, the protons, electrons, and oxygen molecules are recombined into water molecules. In this half reaction heat is produced due to the formation of water. [9]

The catalyst layer is electrically conductive so that the electrons stripped from the hydrogen molecules can find their way to the current collectors and then the external circuit. Furthermore, it is essential that the catalyst layer is in close contact with the membrane so that protons can travel over the membrane. [9] The specific surface area of the catalyst particles is the parameter which determines the performance of a catalyst layer. By minimising the volume per platinum particle and achieving a higher platinum loading in the catalyst layer, the activation losses will be reduced. [9]

Microporous layer

The microporous layer is located between the catalyst layer and the gas diffusion layer and serves two purposes. First of all, the small pore size of this layer improves the electrical contact of the subsequent gas diffusion layer with the catalyst layer. Most importantly, the removal of water is enhanced by the wicking of liquid water into the diffusion layer as a consequence of the small pores. Furthermore, the resulting water droplets are smaller which decreases the likelihood of water flooding the subsequent gas diffusion layer. [9] Due to the small pore size, Knudsen diffusion is expected be prevalent in the microporous layer as the pore size is in the order of the mean free path length of the gases.

Gas diffusion layer

The GDL constitutes of a porous carbon fibre-based material. It provides a pathway for hydrogen and oxygen molecules from the gas flow channels to the reaction sites in the catalyst layer. In addition, the GDL provides drainage pathways for the water produced in the reaction. Water diffuses through the GDL and is drained by the flow in the gas flow channels. Furthermore, the electrons participating in the half-reactions travel from the catalyst sites at the anode to the cathode catalyst sites through the electrically conductive material of the GDL. Finally, the GDL also serves to provide mechanical stability to the membrane and to conduct heat produced in the electrochemical reaction. GDL materials are rendered hydrophobic by treating them with Polytetrafluoroethylene particles. This prevents the accumulation of water in the pores. [9]

Bipolar plates

Bipolar plates enable individual galvanic cells to function together in a stack. First of all, bipolar plates electrically connect the individual cells of the stack in series, adding the cell voltages. Whereas bipolar plates electrically connect the galvanic cells, they also physically separate them. Hydrogen and oxygen fed to adjacent cells are prevented from mixing by the physical barrier the plates provide. Bipolar plates have integrated gas flow channels through which the MEAs are supplied with reactant gases. On one side of the bipolar plate, hydrogen flows through the gas flow channels. Through the gas flow channels on the opposite side, oxygen is supplied to joining cell. Water produced in the stack is also removed through the gas flow channels. The dominant mechanism of water transport in the gas flow channels is convection, i.e., transport by bulk motion. As the dimensions of the gas flow channels are small and the velocity of the flow is generally low, the flow in the gas flow channels is laminar. However, near the manifolds the flow is turbulent.

Additionally, the bipolar plates structurally support the stack and drain the heat produced in the chemical reaction towards the cooling circuit. A bipolar plate must thus therefore be thermally conductive. [9] As PEM fuel cells are mostly used in transportation and portable applications, lightweight bipolar plates are desirable. Bipolar plates contribute a major share in the weight and volume of a stack with 70-90%. As the environment within the stack is acidic, bipolar plates are subject to a corrosive environment. Bipolar plates can be made of stainless steel with graphite deposited onto it. The stainless steel provides low gas permeability, high electric and thermal conductivities, and structural integrity to the stack. Graphite offers protection against corrosion. Under normal operating conditions the stainless steel does not suffer from corrosion. [8]

4 Performance and degradation of a PEM fuel cell stack

The performance of a PEM fuel cell stack can be measured in its power density and its efficiency. The power density of an individual cell is the product of its cell potential and the current density. The relation between the cell voltage and current density at steady-state operation can be displayed in a polarisation curve as depicted in figure 4.1. A polarisation curve can be established by taking measurements of the cell potential against the current density at a constant temperature and pressure. [16] The potential and current density in an electrochemical cell cannot be controlled independently. Consequently, the polarisation curve provides an operational map of the galvanic cell at a certain temperature and pressure.

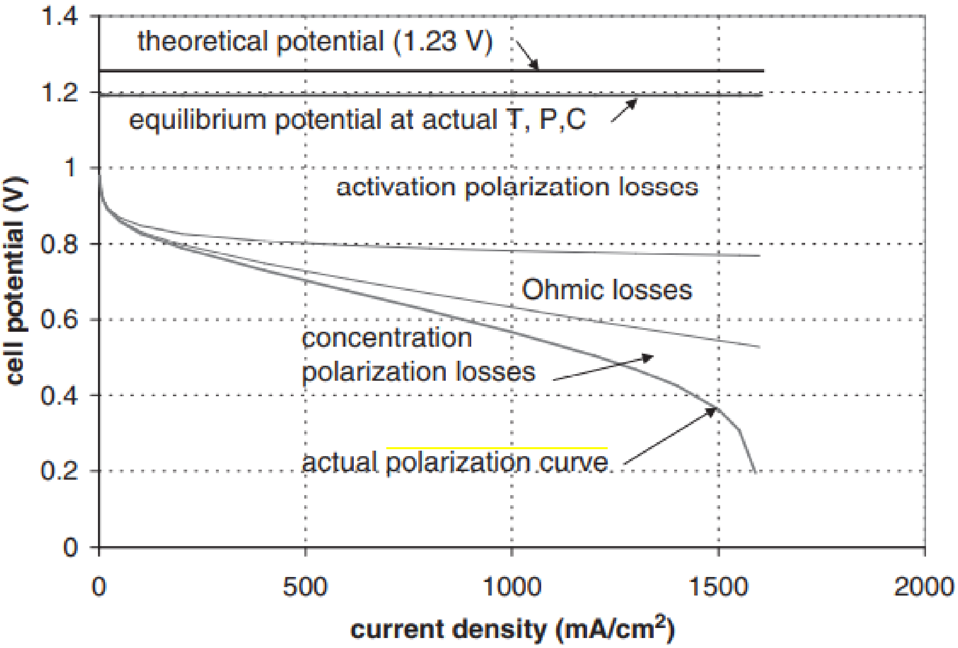

Figure 4.1: Example of a polarization curve for a single galvanic cell [9]

The polarization curve in figure 4.1 is the difference of the reversible equilibrium potential and the potential losses. The potential losses can be divided in open circuit voltage losses, activation polarization losses, the ohmic losses and the mass transfer losses. These phenomena will be elaborated upon in this chapter.

Open-circuit voltage and Gibbs free energy

The maximum potential of a single galvanic cell is the difference in the energy of the electrodes participating in the half-reactions at the anode and cathode in an open circuit. At open circuit conditions no electrons are transported from the anode to the cathode. The half-reactions are in equilibrium and reversible in these circumstances. This means there is no net reaction at the electrodes. This maximum potential is referred to as the open-circuit voltage or the thermodynamic potential. The open circuit voltage of an electrochemical cell is defined as [9]

$$U_{oc} = U_{cathode} - U_{anode} \qquad (4\text{-}1)$$

At the arbitrary standard conditions of a temperature of 298.15 K, a concentration of 1M, and a pressure of 1 bar, the maximum theoretical voltage set by thermodynamics is 1.2291 V as shown in figure 4.1. [16] The standard potential is defined as the difference in potential between a certain reaction and the hydrogen reaction. As a consequence, the standard potential of the hydrogen reaction is defined to be 0 V. The standard potential U_{oc}^0 of the oxygen reaction relative to the hydrogen reaction is 1.229 V. [23]

The open-circuit voltage at operating conditions different than the standard conditions, can be calculated with the Nernst equation. Under typical operating conditions of PEM fuel cells, hydrogen and oxygen can be considered ideal gases. When this assumption is made, the Nernst equation can be written as: [9]

$$U_{oc} = U_{oc}^0 + \frac{RT_{cell}}{2F} \ln\left(\frac{p_{H_2} p_{O_2}^{\frac{1}{2}}}{p_{H_2O}}\right) \qquad (4\text{-}2)$$

In this equation p_{H_2}, p_{H_2O}, and p_{O_2} are the partial pressures of hydrogen, water vapor and oxygen, respectively. R is the ideal gas constant, F is Faraday's constant and T_{cell} is the cell temperature in Kelvin. The maximum electrical work that can in theory be performed by a single cell at constant temperature and pressure can be determined with the change in Gibbs free energy during the electrochemical reaction: [16]

$$W_{el} = -\Delta G_R = nFU_{oc} \qquad (4\text{-}3)$$

In relation (4-3), n is the number of electrons transferred in the reaction. This amounts to two electrons in the electrochemical reaction occurring in a PEM fuel cell. F is Faraday's constant and U_{oc} is the open-circuit voltage. The Gibbs free energy is a thermodynamic potential with temperature and pressure as the natural variables. [24] This means the Gibbs free energy varies with the temperature and pressure. Raising the temperature at which a fuel cell stack operates, lowers the open-circuit voltage. [25] When the temperature is raised to 333.15 K at atmospheric pressure, the open-circuit voltage is reduced to 1.200 V. When the temperature is raised to 353.15 K, the open-circuit voltage decreases to 1.184 V. [9]

The change of the Gibbs free energy of a chemical reaction can also be determined with the following relation: [16]

$$\Delta G_R = \Delta G_f^{products} - \Delta G_f^{reactants} \qquad (4\text{-}4)$$

Where ΔG_f is the Gibbs energy of formation. The sign of the change of the Gibbs free energy in (4-4) determines whether a reaction occurs spontaneously. If $\Delta G_R < 0$, the reaction occurs spontaneously. In this case work can be extracted from a chemical reaction, which is the case in a PEMFC. In case of a positive sign, work has to be put in for the reaction to occur.

Relation (4-3) from equilibrium thermodynamics may only be used at open-circuit conditions. In a fuel cell operating on hydrogen and oxygen at standard conditions the change in Gibbs free energy amounts to -237 kJ/mol of electrons. Due to the electrochemical reaction occurring at two physically separated electrodes, where one of the components reacting is not present, work can be harvested from the electrochemical reaction.

Relation between reaction rate and current

The consumption rate of hydrogen and oxygen, and the production rate of water at the electrodes of a galvanic cell are related to the current through Faraday's law:

$$\dot{N}_i = \frac{I}{nF} \tag{4-5}$$

In equation (4-5), $\dot{N}_i$ is the number of moles consumed or produced per second of species i, I is the current through the external circuit and as a consequence of potential losses, n is the number of electrons that are transferred for species i, and F is Faraday's constant.

The hydrogen and oxygen consumption rate, and the water production rate [mol s^{-1}] resulting from Faraday's law are [9]

$$\begin{cases} \dot{N}_{H_2} = \frac{I}{2F} \\ \dot{N}_{O_2} = \frac{I}{4F} \\ \dot{N}_{H_2O} = \frac{I}{2F} \end{cases} \tag{4-6}$$

By multiplying the equations in (4-6) with the molar mass of hydrogen M_{H_2}, oxygen M_{O_2}, and water M_{H_2O} respectively, mass flow rates [g/s] at the electrodes can be found.

$$\begin{cases} \dot{m}_{H_2} = \frac{I}{2F} M_{H_2} \\ \dot{m}_{O_2} = \frac{I}{4F} M_{O_2} \\ \dot{m}_{H_2O} = \frac{I}{2F} M_{H_2O} \end{cases} \tag{4-7}$$

The equations in (4-7) are valid for an individual cell. By multiplying (4-7) with the number of cells in the stack, the cumulative mass flow rates can be found.

Potential loss mechanisms

Ideally, the polarisation curve of a galvanic cell would be a horizontal line as shown in figure 4.1. In reality, various potential losses come into play when a current is drawn from a cell. These loss mechanisms reduce the cell voltage and consequently the efficiency of the cell. The potential losses increase with increasing current density.

The first potential loss is the open-circuit voltage loss. The open-circuit voltage is lower than the theoretical reversible open-circuit potential predicted with the Nernst equation. This is the result of a small amount of hydrogen, oxygen and electrons crossing over through the membrane. These reactants do not partake in the half-reactions. Additionally, the kinetics of the oxygen reduction reaction in an acidic environment are so slow at low temperatures that contaminants and impurities can compete in side reactions. [16]

The cell voltage U_{cell} of a galvanic cell can be determined by deducting the potential losses stemming from various mechanisms from the real open-circuit voltage $U_{OC,r}$:

$$U_{cell} = U_{OC,r} + \eta_c - \eta_a - \Delta V_e - \Delta\phi - \Delta V_{mt} \tag{4-8}$$

The potential loss mechanisms in relation (4-8) are the activation losses ($\eta_c - \eta_a$) which stem from the half-reactions, ohmic losses in the electrolyte ($\Delta\phi$), losses from the transport of electrons in the external circuit (ΔV_e), and finally the potential loss as a consequence of mass transfer (concentration polarization losses) in the porous electrodes ΔV_{mt}. The potential loss stemming from the transport of electrons through the electrodes of the cell is negligible. The actual electrical work that can be performed by a single galvanic cell can be found by replacing U_{oc} with U_{cell} in relation (4-3).

The voltage efficiency of a PEMFC is defined as:

$$\varphi = \frac{U_{cell}}{U_{oc}} \tag{4-9}$$

The maximum theoretical efficiency of a PEMFC can be found by dividing the Gibbs free energy by the heat of formation of water. This results in a maximum efficiency of approximately 83%. When taking relation (4-8) and (4-9) into account, it should be noted that the efficiency of a PEMFC can be increased by lowering the potential losses. As displayed in figure 4.2, the dominant source of potential losses in an operating PEMFC stack is always the activation of the half-reactions. The activation losses are predominantly a consequence of the slow oxygen reduction reaction. The gradient of the potential loss curves vary with the current density at which the fuel cell is operated as portrayed in figure 4.2. [9]

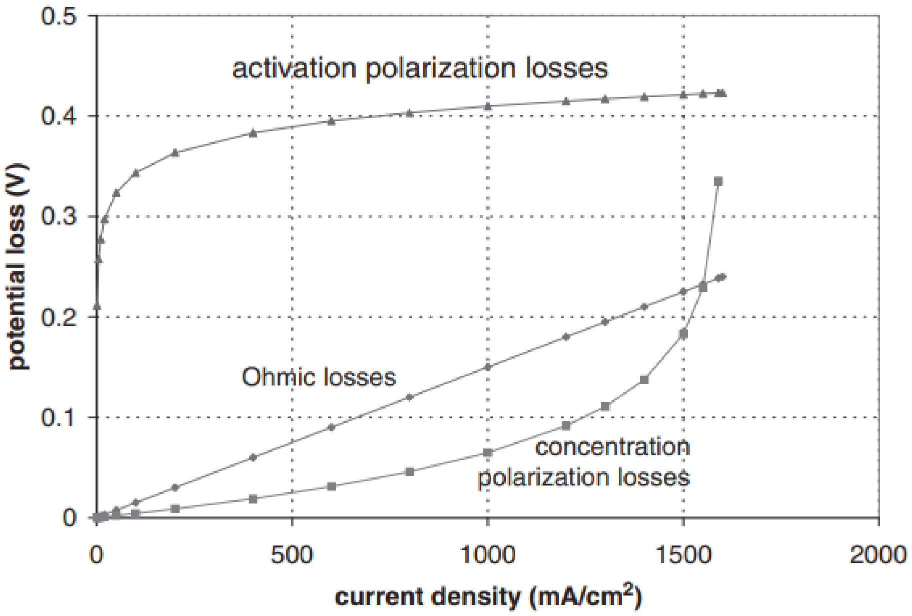

Figure 4.2: The evolution of potential loss mechanisms over a range of current densities [9]

The curves depicted in figure 4.2 portray how the gradient of the potential losses evolve over a range of current densities from 0 to 2000 mA/cm^2. The activation overpotentials increase most rapidly at low current densities, after which they plateau. Beyond a current density of 500 mA/cm^2 the change in the activation losses is relatively limited compared to the growth in Ohmic losses. It can be seen that the Ohmic losses as a result of charge transport across the membrane increase linearly with the current density. The Ohmic losses are the dominant source of potential losses between 500-1200 mA/cm^2. Above a current density of approximately 1200 mA/cm^2, the mass transfer losses (concentration polarisation losses) become the dominant source of potential losses.

Activation potential losses

The activation potential losses are a consequence of the energy barriers that have to be overcome for the half-cell reactions at the electrodes to progress at a discernible rate. This energy barrier is referred to as the activation energy E_a. The activation energy is the energy threshold that has to be surpassed in order to bring molecules in a state where they can participate in a chemical reaction [41A]. The platinum particles in the catalyst layer lower the activation energy.

At low current densities the cell voltage U_{cell} decreases rapidly (Figure 4.1). This is a consequence of the rapid surge in the activation potential losses at low current densities. In relation (4-8) η_c and η_a are the activation overpotentials of the cathode and anode respectively, where $\eta_a > 0$ and $\eta_c < 0$ by convention. Especially the cathode overpotential contributes to the voltage losses as the activation energy for the oxygen reduction reaction to occur, is significantly higher than the activation energy for the hydrogen oxidation reaction. The kinetics of the oxygen reduction reaction are much slower than those of the hydrogen oxidation reaction. As a consequence, the anode activation potential loss can be neglected. [16] The activation energy influences the reaction rate constant k as shown in the Arrhenius equation: [52]

$$k = Ae^{\frac{E_a}{RT}} \tag{4-10}$$

In the Arrhenius equation, A is a constant dependent on the chemical reaction. From (4-10) it can be deduced that the reaction rate can be increased by raising the temperature and lowering the activation energy through improved catalyst layers. This will also lead to lower activation potential losses.

Ohmic potential loss $\Delta\phi$

The potential loss as a consequence of proton transfer across the membrane is given by: [9]

$$\Delta\phi = \frac{jL}{\kappa_{\text{proton}}} \tag{4-11}$$

The Ohmic potential loss increases linearly with the current density j, as depicted in figure 4.2. The Ohmic potential loss is also proportional to the membrane thickness L, and inversely proportional to the membrane's proton conductivity κ_{proton}.

Mass transfer potential loss ΔV_{mt}

When reactants are consumed at a high rate at the surface of the platinum particles, a reactant concentration gradient is established between the bulk and the interface. When the PEMFC is operated at a high current density, a high rate of hydrogen and oxygen is consumed. As a result, the concentration of these reactants is low at the surface of the electrodes compared to the bulk concentration. [9]

At a certain current density, as much hydrogen is consumed as can be supplied to the catalyst layer by diffusion. It is not possible to increase the current density beyond this point. This current density is referred to as the limiting current density. In reality, there is a non-uniform distribution of reactants at the electrodes, which means there is no uniformly distributed current density at the electrodes as well. Some parts of the electrode might operate at the limiting current density, whereas others operate at a lower current density. This implies that the steep decline in the cell voltage as depicted in figure 4.1, cannot be witnessed in the polarization curve of real PEM fuel cells. Mass transfer potential losses can also stem from blocked pathways to the catalyst sites due to a flooded electrode or a build-up of inert species. [9]

Liquid water in the electrodes

When the pressure is above the saturation pressure, water condenses in the gas diffusion layers, microporous layers, catalyst layers and gas flow channels. [26] The saturation pressure of water depends on temperature according to the following relation [17]

$$\log_{10} P_{\text{sat}} = -2.1794 + 0.02953T - 9.1837\,.\,10^{-5}T^2 + 1.4454\,.\,10^{-7}T^3 \tag{4-12}$$

When water condenses in the porous layers of the electrodes, it mostly occurs at the surface of already existing microdroplets. As a consequence, the microdroplets grow in size. This growth is illustrated in figure 4.3. In the final stage, the microdroplets grow to such an extent that they completely obstruct pathways in the porous electrodes.

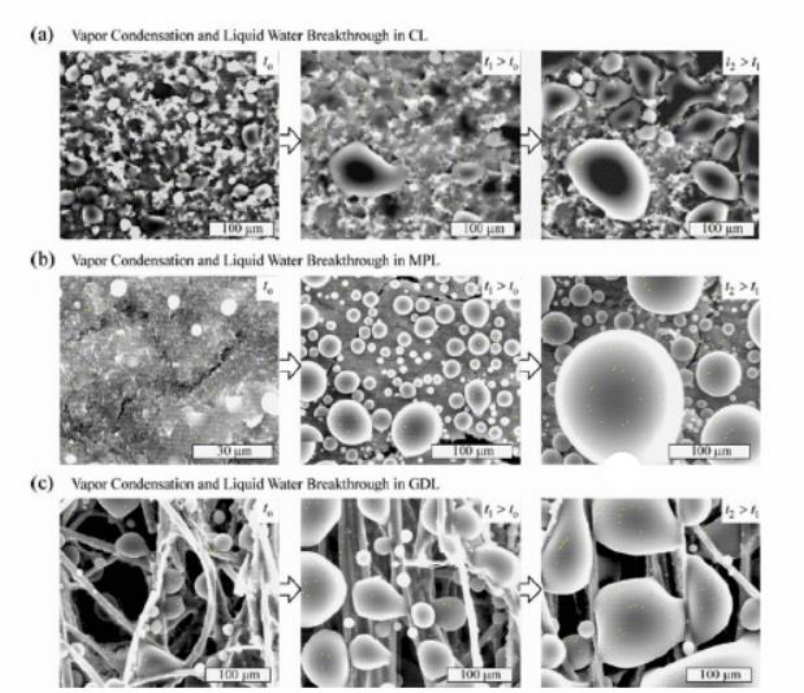

Figure 4.3: Microscopic view of the growth of water droplets in the (a) catalyst layer, (b) the microporous layer, (c) and the gas diffusion layer [26]

In figure 4.4, the transport of water from the cathode catalyst layer to the gas flow channel is depicted. Droplets of water are drained from the GDL in small branches which culminate in a large stream. This structure of droplets gravitating towards a larger stream resembles a tree. Liquid water in the GDL is transported by capillary action, which can be considered a diffusive term. The viscous effects can be neglected in the transport of liquid water through the GDL. When water droplets reach the interface of the GDL and the gas flow channel, they are either carried away by the gas flow, evaporate or become attached to the walls of the gas flow channels. Water in the gas flow channels is transported as droplets, films attached to the channel walls, or as vapor. Liquid water droplets at the interface of the gas diffusion layer and the gas flow channel give rise to a transport resistance of gaseous reactants into the GDL.

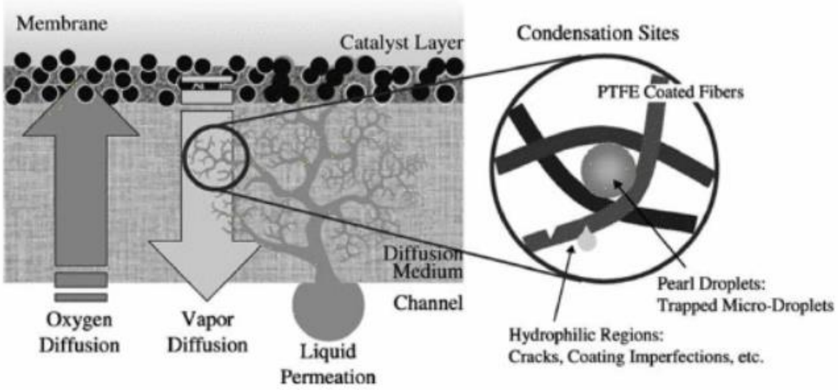

Figure 4.4: Branching water transport in a cathode gas diffusion layer [26]

Degradation mechanisms related to water management

Multiple degradation mechanisms of a PEMFC stack can be mitigated by adequate water management. In dry operation, the membranes will degrade faster due to the formation of cracks and pinholes. Maintaining adequate humidification of the inlet flows of the reactants does therefore not only guarantee short term stability but also longevity of the stack. Furthermore, freezing of water in the catalyst layer leads to degradation of the reaction surface. Additionally, flooding of the electrodes leads to corrosion of their carbon backbone. [26]

Carbon corrosion is a consequence of oxygen or hydrogen starvation at the catalyst sites. The amount of water produced in a cell increases with the current density. Therefore, flooding is a greater problem at higher current densities. Flooding can also be alleviated by raising the stoichiometry at which the reactants are fed to the stack. This is the ratio between the amount of a reactant supplied to the stack and the amount consumed. At higher stoichiometries the reactant flows are better able to drain the water from the interface of the GDL and the gas flow channel.

Carbon corrosion occurs when the carbon backbone of the catalyst layer and the gas diffusion layer participates in an electrochemical reaction with water. There are two reactions which contribute to carbon corrosion. [27] The products of the first reaction are carbon dioxide, protons and electrons:

$$C+2H_2O \rightarrow CO_2+4H^++4e^- \tag{4-13}$$

The standard reduction potential of this reaction is 0.207 V, meaning that it occurs when a cell operates above this voltage. In the second reaction, water and carbon react in a different ratio producing carbon monoxide, protons, and electrons:

$$C+H_2O \rightarrow CO+2H^++2e^- \tag{4-14}$$

The standard reduction potential of the latter reaction is 0.518 V. The rate of carbon corrosion increases by approximately one order of magnitude for every 0.1 V increase in the cell potential above 1.0 V. The rate of carbon corrosion can be measured by measuring the CO_2-concentration. Carbon corrosion reduces the thickness and the mechanical strength of the gas diffusion layer. Additionally, the electrical resistance of the gas diffusion layer is increased. Finally, the mass transport resistance is increased in a corroded gas diffusion layer and catalyst layer. [28]

A higher platinum loading in the catalyst layer increases the rate of carbon corrosion. The greater the platinum loading, the greater the interfacial area between the carbon backbone and the platinum particles. As a consequence, the amount of carbon exposed to the reaction zone is higher as well. When the carbon backbone corrodes, the supported platinum particles disengage. Furthermore, carbon corrosion reduces the hydrophobicity of pores in the catalyst layer. This complicates the passage of liquid water from the GDL towards the gas flow channel. Therefore, flooding is a self-reinforcing phenomenon. In case of an unevenly flooded stack, the affected cells degrade faster as the carbon backbone disappears at a higher rate.

In the zone affected by flooding, water is also electrolysed. Oxygen, protons, and electrons are produced according to the following reaction:

$$2H_2O \rightarrow O_2+4H^++4e^- \tag{4-15}$$

In addition to the oxygen produced in electrolysis, a minute amount of oxygen crosses over from the cathode to the anode. Hydrogen and oxygen form water which creates an interface with the hydrogen outside of the flooded zone. This causes the flooded zone to grow. These reactions lead to a reverse current which is notable as a spike in the cell voltage as shown in figure 4.5.

A measure against flooding on the anode side of the cells, is feeding the oxygen and hydrogen in counter-flow mode. In this manner, the hydrogen feed can be hydrated with water crossing over from the cathode to the anode through the membranes. Furthermore, reducing the inlet pressure of the anode and raising the feed temperature also aides in diminishing flooding. The stoichiometry of hydrogen in the anode determines how much water can be taken away from the PEMFC stack. Therefore, it is also an important parameter in controlling flooding. The aforementioned parameters play a vital role in the water management of the anode loop. When these are properly set, the anode loop is well-humidified while avoiding flooding of the electrodes.

Detection and of electrode flooding

According to O’Rourke et at., [29] flooding of the anodic electrodes occurs at lower current densities. Here the hydrogen flow rate is not high enough to drain all liquid water from the gas flow channels. The rate of water removal from the anode flow field depends on the geometry of the gas flow channels, the surface properties of the bipolar plate, and the hydrogen flow rate. The most severe flooding occurred in the cells closest to the end plates of the stack. The temperature of the cells close to the end plates is somewhat lower than the temperature of the cells closer to the core. Accordingly, the saturation pressure of water in the outer cells is somewhat lower in the outer cells of a stack. Therefore, condensation of water occurs first in the anodes of the outer cells.

The experimental set-up used by O’Rourke et at., consisted of an eight-cell stack in a test station. O’Rourke et al. proposed a method to detect anode flooding in an operational setting. Through introducing a current spike in the fuel cell, individual cell voltages in a stack were measured and compared to the median voltage. A deviation from the median voltage indicates flooding in the respective cell. If there is a significant deviation from the median voltage, hydrogen should be blasted to clear the anode flow channel and gas diffusion layer from an excess of liquid water. This means the stoichiometry of the hydrogen feed was temporarily increased.

In order to determine the cell voltages, the impedance was measured while the operating conditions were kept constant. A small AC load was superimposed on the DC load of the stack that varied in frequency between 0 and 15 kHz. This method is called a frequency sweep, during which the time-dependent behavior of the individual cell voltages can be determined. When a decline in a cell voltage as shown in figure 4.5 is witnessed greater than some predetermined deviation of the median voltage, this is an indication of flooding in the corresponding cell.

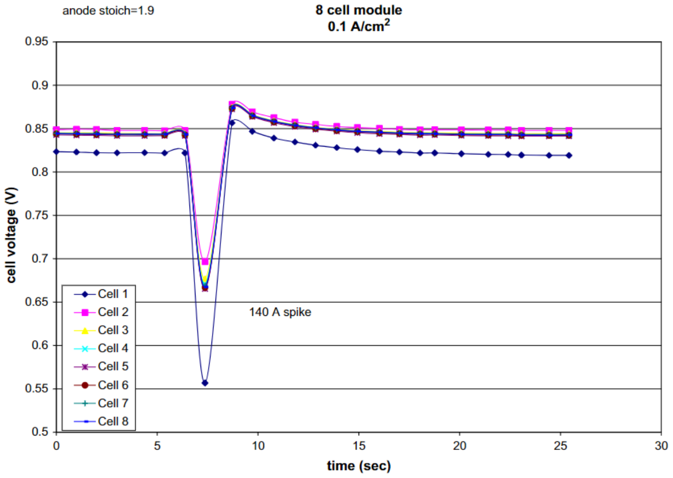

Figure 4.5: Spike in cell voltage in cells affected by anode flooding [29]

Summary

In order to maintain stable instantaneous operation, it is vital to maintain a high membrane water content. This guarantees a high proton conductivity which allows protons to be transported over the membrane without a high Ohmic potential loss. Furthermore, a higher operating temperature positively influences the proton conductivity. Activation potential losses are also lower at higher temperatures. Moreover, the presence of liquid water in the stack should be minimized in order to reduce mass transfer losses.

The same recommendations hold regarding the water management of the anode loop in order to extend the lifetime of the stack. First of all, a sufficiently high relative humidity of the inlet hydrogen should be maintained. When the stack is operated under insufficient humidification the membranes will dry out which leads to the formation of cracks and pinholes. Secondly, liquid water should be prevented from entering the stack and condensation in the stack should be minimized. The presence of liquid water gives rise to flooding of the electrodes and subsequently carbon corrosion of the MEA.

5 Membrane water crossover in a PEMFC stack

The relation between the current at which a PEM fuel cell stack is operated and the production rate of water in the cathode catalyst layer has been established through Faraday's law. The water in the anode loop of PowerCell's systems originates from the cathode side of the membranes. The membrane serves as a medium for water transport from the cathode to the anode. In this chapter the mechanisms of water transport through the membrane are described.

As mentioned in the introduction, the first step in this work is to predict the amount of water crossing over to the anode side of the membranes. The available literature on PEM water crossover models will be reviewed and in a later section the water crossover predicted by these models will be compared to measurement values.

Quasi-2D mass transport models

Mass transport in a PEM fuel cell stack occurs along the gas flow channels and through the MEA. Mass transport in the aforementioned sections can be decoupled in two 1D problems. This is referred to as a quasi-2D modelling by Kulikovsky. [19] This is a common approach in the modelling of mass transfer in PEM fuel cell stacks. Quasi-2D modelling is illustrated in figure 5.1 with a schematic depiction as shown in lecture slides by J.W. Haverkort. The direction perpendicular to the MEA is taken as the x-coordinate, whereas the direction parallel to the gas flow channels is taken as the z-coordinate.

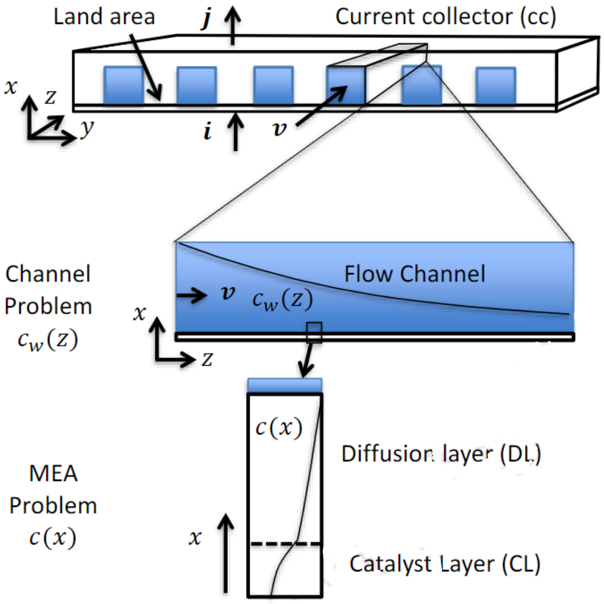

Figure 5.1: (a) Top view of the bipolar plate (b) Side view of a section of a gas glow channel (c) Section of a MEA[1]

The use of quasi-2D models can be justified by comparing the diffusive fluxes and advective fluxes along the x- and z-coordinates in a scaling analysis.

---

[1] Figure taken from reader accompanying the fifth lecture of the course Electrochemical energy storage 2 by J.W. Haverkort which is not publicly available

First of all, the concentration gradient of water is much greater through the MEA than along the gas flow channels. This is due to the much smaller length scale of the diffusion layer and catalyst layer compared to that of the gas flow channels. The length scale of a gas flow channel parallel to the flow direction is $L_{GFC} \sim 0.1 - 1$ m, whereas the length scale of the MEA is $L_{MEA} \sim 100\,\mu\text{m}$. The quotient of the diffusive fluxes along the gas flow channel and through the MEA can be defined as

$$\frac{\dot{N}_{dif,GFC}}{\dot{N}_{dif,MEA}} \sim \frac{L_{GFC}}{L_{MEA}} \ll 1 \qquad (5\text{-}1)$$

The diffusion of water along the direction of the gas flow channel is negligible compared to the diffusion through the MEA as shown in (5-1). The same line of reasoning can be followed for water transport due to advection. The velocity of the flow along the gas flow channel is far greater than the velocity through the MEA. Therefore, the water transport through the MEA can be considered a 1D problem dominated by diffusion, whereas the water transport through the gas flow channel is a 1D problem dominated by advection. The two problems are coupled by water transport across the interface of the gas diffusion layer and the MEA.

Water transport mechanisms across the membrane

According to Barbir, [9] three modes of water transport through the membrane can be distinguished. These are the mechanisms of electro-osmotic drag, back-diffusion, and hydraulic permeation. These mechanisms are represented in the conservation equation of water in a membrane [26]

$$\varepsilon_m \frac{\partial C_w^m}{\partial t} = \nabla \cdot \left(D_w^{m,\text{eff}} \nabla C_w^m + \vec{G}_{w,\text{perm}} \right) - \frac{1}{F} \nabla \cdot \left(n_d \vec{i}_e \right) \qquad (5\text{-}2)$$

In this conservation equation the first term on the left describes the water holding capacity. The constant ε_m is the ionomer volume fraction in the membrane and C_w^m is the equivalent water concentration in the membrane defined as:

$$C_w^m = \frac{\rho_m \lambda}{\text{EW}} \qquad (5\text{-}3)$$

In relation (5-3), ρ_m equals the density of the membrane, λ the water content of the membrane and EW the equivalent weight of the membrane, which is defined as the weight of Nafion per sulfonic acid group. The three terms on the right side of the conservation equation describe the back-diffusion, hydraulic permeation, and electro-osmotic drag mechanisms respectively.

Membrane water crossover due to back-diffusion

The first water transport mechanism across the membrane to be introduced, is back-diffusion. This is a mechanism of transport induced by a water concentration gradient from the cathode to the anode side of the membrane. At the cathode, the water concentration is comparatively high due to the production of water in the oxygen reduction reaction. The water flows from the cathode to the anode as a result of random motion of water molecules on average following the concentration gradient. As the diffusivity of water in the membrane depends on the water content of the membrane, back-diffusion is a nonlinear transport mechanism. The rate of water transport by diffusion (mol s^{-1} cm^{-2}) over the membrane is given by: [9]

$$\dot{N}_{\text{H}_2\text{O,diffusion}} = D_w^m(\lambda) \frac{\Delta c}{\Delta x} \qquad (5\text{-}4)$$

In order to find the diffusive molar flux of water across the membrane, the diffusion coefficient is to be multiplied with the water concentration gradient across the membrane as specified in (5-4). Multiple methods have been used to experimentally determine the diffusion coefficient of Nafion membranes. [9]

When a membrane does not entirely consist of an ionomer such as Nafion, the diffusion coefficient D_w^m has to be corrected by multiplying it with the volume fraction of the ionomer ε_m in the membrane. In this way reinforced membranes such as those used by PowerCell can be represented with (5-5) as well. This gives the following effective diffusion coefficient [26]

$$D_w^{m,\text{eff}} = \varepsilon_m D_w^m \tag{5-5}$$

It should be noted that reinforced membranes have a lower effective diffusion coefficient. Reinforced membranes still have a relatively high diffusive flux of water due to their thinness, which gives rise to a greater concentration gradient.

Membrane water crossover due to electro-osmotic drag

The second mechanism introduced by Barbir, is water transport by electro-osmotic drag. This transport mechanism is coupled with proton transport across the membrane. It occurs in the opposite direction of back-diffusion. Water molecules are dragged along with the protons crossing over from the anode side to the cathode side of the membrane. The driving force of this transport mechanism is the potential across the membrane. The water flux $\dot{N}_{\mathrm{H_2O,drag}}$ [mol s^{-1} cm^{-2}] as a result of electro-osmotic drag is proportional to the current density. The constant $\xi(\lambda)$ in this proportional relation is referred to as the electro-osmotic drag coefficient. [9]

$$\dot{N}_{\mathrm{H_2O,drag}} = \xi(\lambda)\frac{I}{F} \tag{5-6}$$

The electro-osmotic drag coefficient $\xi(\lambda)$ is defined as the number of water molecules per proton. It is a function of the water content of the membrane. Furthermore, I is the protonic current over the membrane. The value of $\xi(\lambda)$ depends on the measurement method used, the data fit, and the membrane used.

There are two expressions for $\xi(\lambda)$ which are especially popular. [26] First of all there is the electro-osmotic drag coefficient proposed by Springer et al. [17]

$$\xi(\lambda) = \frac{2.5\lambda}{22} \tag{5-7}$$

Another electro-osmotic drag coefficient was proposed by Zawodzinski: [30]

$$\xi(\lambda) = \begin{cases} 1.0 \text{ for } \lambda \leq 14 \\ \frac{1.5}{8}(\lambda - 14) + 1.0 \text{ otherwise} \end{cases} \tag{5-8}$$

Both Springer et al. and Zawodzinski proposed coefficients based on experiments on a Nafion 117 membrane.

Membrane water crossover due to hydraulic permeation

The final water transport mechanism across the membrane mentioned by Barbir is hydraulic permeation. It manifests itself as a consequence of a liquid water pressure difference between both sides of the membrane. The transport of liquid water follows the decreasing pressure gradient. The flux as a consequence of hydraulic permeation is negligible compared to the fluxes caused by electro-osmotic drag and back-diffusion. The liquid water flux due to hydraulic permeation can be described by the following relation:

$$\vec{G}_{w,\mathrm{perm}} = -\frac{K_m}{M_w v^l} \nabla p^l \tag{5-9}$$

In this relation ∇p^l is the liquid water pressure gradient over the membrane, K_m the intrinsic permeability of the membrane, M_w the molecular weight of water, and v^l the diffusive velocity of liquid water. Relation (5-9) can be simplified to:

$$\dot{N}_{\mathrm{H_2O,Perm}} = k_{\mathrm{Perm}}(\lambda) \frac{\Delta p}{\Delta x} \tag{5-10}$$

In relation (5-10), $k_{\mathrm{Perm}}(\lambda)$ is the hydraulic permeability coefficient of the membrane at a certain water content λ, whereas $\frac{\Delta p}{\Delta x}$ is the pressure gradient over the membrane.

Net water transport coefficient α

As noted, electro-osmotic drag and back-diffusion are counteracting mechanisms of water transport. The net water transport coefficient α serves to indicate the dominant mechanism between them. It is a dimensionless number equal to the water molecules per proton. When $\alpha > 0$, there is a net transport of water from the anode to the cathode. Conversely, if $\alpha < 0$, there is a net transport of water from the cathode to the anode. Due to the diffusion component, net water transport across the membrane is a nonlinear phenomenon as well. A general definition of the net water transport coefficient is given by Wang & Chen [17]

$$\alpha = \xi(\lambda) - \frac{FG}{I} \tag{5-11}$$

In relation (5-11), G is the cumulative water flux as a consequence of back-diffusion and hydraulic permeation from the cathode to the anode.

Janssen and Overvelde [31] found that the net water transport coefficient α in Nafion 105 (127 µm) and Nafion 112 (51 µm) membranes, [32] is greatly affected by the anode gas flow humidification. The pressure differential across the membrane did not have a noticeable effect on α, however. This indicates that hydraulic permeation in Nafion™ 105 and Nafion™ 112 is negligible. This assumption is also used in many models proposed for water-crossover through the membrane. The anode and cathode stoichiometry, and the inlet relative humidity of the reactants had a large effect on the net water transport coefficient. In Janssen and Overvelde's experiments the anode outlet gas flow was always saturated unless the cathode inlet flow was dry.

Effect of crossover on membrane humidification

It has been observed experimentally by Büchi and Scherer, [33] that the anode side of the membranes may dry out in fuel cells with a thicker membrane. The thicker membranes, such as the 400 µm and 240 µm specimens, were constructed of multiple layers of Nafion sheets. Back-diffusion cannot sufficiently humidify the anode side of the membrane in such cases. It was experimentally shown that the Nafion layer on the anode side dried out at high current densities as a result of the increased electro-osmotic drag. Consequently, the membrane resistance increases with increasing current densities (Figure 5.2). For thinner membranes (thickness below 120 µm), the membrane resistance is independent of the current density. In these cases, a higher water production and back-diffusion were able to offset the effects of a higher water flux due to electro-osmotic drag.

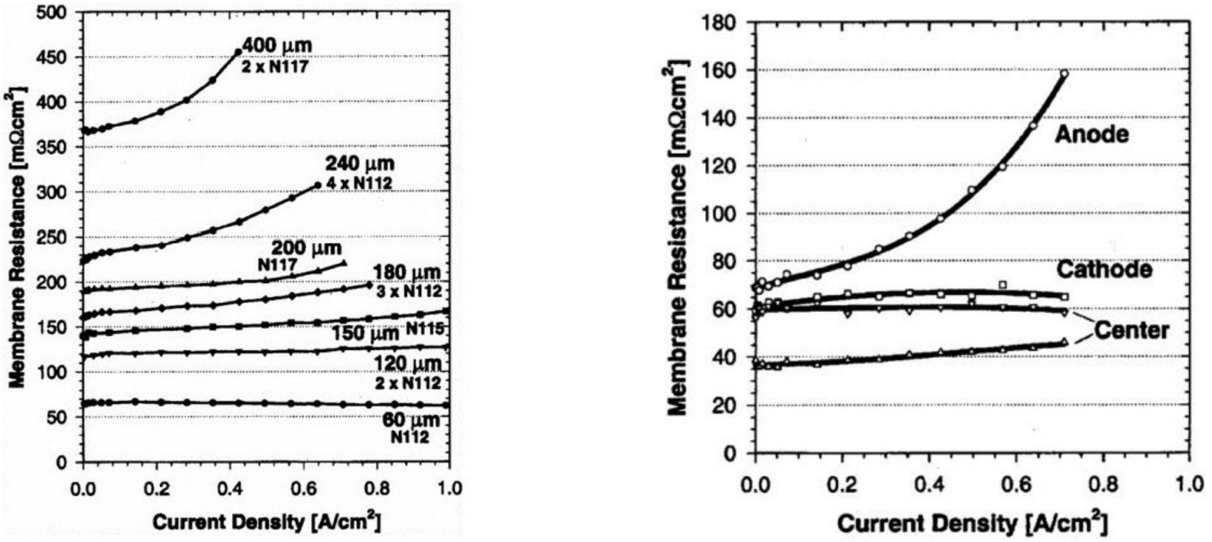

Figure 5.2: (a) Dependence of the membrane resistance on the current density, (b) Contribution of layers to the membrane resistance for the 240 µm membrane [27]

State-of-the-art reinforced membranes have a thickness between 15 and 30 µm. In a study executed by Ye & Wang, [34] it was demonstrated that for these membranes the opposite effect can be witnessed when raising the current density as displayed in figure 5.3.

For Gore-select membranes with a thickness of 18 µm, it was found that the Ohmic resistance over the membrane was lower under current load than at open circuit at a set relative humidity. This contrast became starker at lower levels of relative humidity of the gas flows surrounding the membrane. The humidification of these membranes improved with increasing current density.

Therefore, it can be concluded that operating a fuel cell at high current densities does not dehydrate the anode side of the membrane when using thin membranes. At higher current densities the water production gives rise to an increased concentration gradient of water across the membrane. This phenomenon dominates over the increased electro-osmotic drag. The higher concentration gradient over the membrane also stems from its thinness.

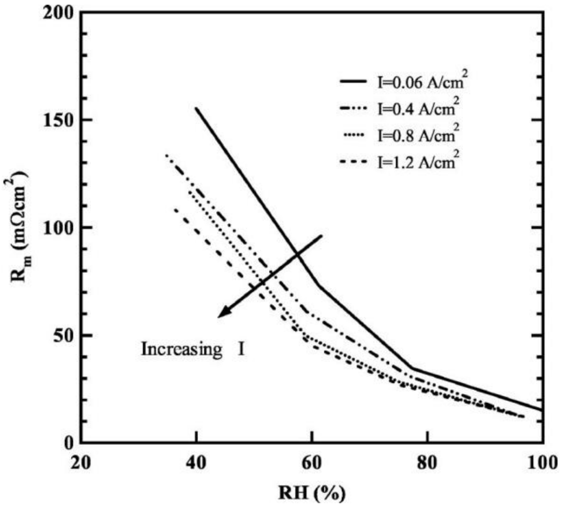

Figure 5.3: Measured Ohmic resistance of Gore-Select membranes (18 microns) under current load versus relative humidity [34]

Experimental water crossover models

Since the early 1990s, sustained efforts have been made to experimentally quantify the fluxes of water crossover in membranes in PEMFCs. A selection of models based on these studies will be elaborated upon now. In a further section of this thesis, the values of water crossover predicted by these models will be compared to measurement data made available by PowerCell. To this end, the operational parameters of the measurement points will be inserted into the models found in literature. Ideally, these models will reflect the recorded values in the test station.

Springer model

In 1991, a group of researchers at the Los Alamos National Laboratory published a seminal article on water transport across PEM fuel cell membranes. In their article Springer et al. formulated an isothermal, one-dimensional, and stationary model [17] for water transport across a proton exchange membrane. The model additionally provides a relation between the membrane water content and its protonic conductivity as mentioned in (3-6). Springer et al. did not account for depletion of reactants along the channel and the production of water along the length of the cathode catalyst layer. Furthermore, latent heat as a result from evaporation and condensation was not taken into account in this model.

In the Springer model, five regions of the galvanic cell are represented: the membrane, two gas flow channels, and two electrodes. The electrodes are not split up in the gas diffusion layer, microporous layers, and catalysts layer but treated as uniform components. Transport of water through the electrodes is assumed to be driven by Fickian diffusion, whereas in the membrane water transport also occurs due to electro-osmotic drag.

Springer et al. draw upon experimentally determined transport parameters by their research group. These transport parameters include the water-diffusion coefficients in Nafion, electro-osmotic drag coefficients, water sorption isotherms, and membrane conductivity as a function of membrane water content. An extensive set of experiments was carried out at various water contents in order to determine the spatial variation of parameters in the membrane in the presence of a water content gradient at any current density. The Springer model only qualitatively touches upon the transport of water droplets in the electrode.

It is assumed that the gas mixtures in the electrodes containing water vapor behave as ideal gases. Only a concentration gradient across the gas diffusion layer is considered in the Springer model. A pressure gradient is not considered, meaning hydraulic permeation of liquid water is not taken into account.

Water transport in the anodic electrode

In the gas diffusion layer on the anode side there is binary diffusion of hydrogen and water vapour. The concentration gradient of water vapour in the gas diffusion layer on the anode side is defined as

$$\frac{dy_{\mathrm{wA}}}{dx} = \frac{RT_{cell}\dot{N}_p}{p_{\mathrm{A}}D_{\mathrm{wH}}}\left[y_{\mathrm{wA}}(1+\alpha)-\alpha\right] \tag{5-12}$$

In relation (5-12), y_{wA} is the water vapour mole fraction, p_{A} the pressure the anode is operated at, α is the net water transport coefficient, D_{wH} is the diffusion coefficient, and $\dot{N}_p$ is the molar flux of water production at the cathode. The higher the operating pressure of the anode, the smaller the water concentration gradient across the anode gas diffusion layer. The water vapour mole fraction at the interface of the membrane and the anodic electrode can be found by integrating (5-12). This gives the following relationship:

$$y_{\mathrm{w,interface\ electrode/membrane}} = \left(y_{\mathrm{w,\ interface\ GDL/GFC}} - \frac{\alpha}{1+\alpha}\right) \exp\left(\frac{RT_{cell} I t_{\mathrm{A}}}{P_{\mathrm{A}} D_{\mathrm{wH}}}\right) + \frac{\alpha}{1+\alpha} \qquad \text{(5-13)}$$

In relation (5-13), t_{A} is the thickness of the anodic electrode. At the interfaces of the electrodes and the membrane, equilibrium in water activity is assumed which determines the local amount of water on the membrane surface.

Diffusive water transport in the membrane

Zawodzinski, [30] a co-author of the Springer model measured the intradiffusion coefficient D' of water in a Nafion 117 membrane using the nuclear magnetic resonance technique. The molar flux of water through the membrane as a consequence of diffusion is denoted in the following manner by Springer et al.

$$\dot{N}_{\mathrm{w,diff}} = -\frac{D' c_{\mathrm{w}}}{RT_{cell}} \nabla\mu = -\frac{D' c_{\mathrm{w}}}{RT_{cell}} \nabla(\mathrm{RTln}a) = -\frac{\rho_{\mathrm{dry}}}{M_{\mathrm{m}}} D_{\lambda} \frac{d\lambda}{dx} \qquad \text{(5-14)}$$

In relation (5-14), c_{w} is the water concentration, D_{λ} is the diffusion coefficient of water in Nafion corrected for membrane swelling, ρ_{dry} is the density of a dry membrane, M_{m} is the equivalent weight of the membrane, and a is the water vapor activity which is defined at the interface between the membrane and the electrode. The activity of water vapor is determined by the following relation:

$$a = \frac{x_{\mathrm{w}} p}{p_{\mathrm{sat}}} \qquad \text{(5-15)}$$

In relation (5-15), x_{w} is the mole fraction of water and p is the pressure. The saturation pressure of water is taken from (3-12). According to Barbir, the water activity can be taken equal to the relative humidity in case the gases fed to the galvanic cell are assumed to behave as ideal gas mixtures.

The water uptake of the membrane can be calculated with the experimental relation determined by Zawodzinski [30] as a function of the water activity.

$$\lambda_{(30)} = 0.043 + 17.81a - 39.85a^2 + 36.0a^3 \quad \text{for } 0 < a \leq 1 \qquad \text{(5-16)}$$

In equilibrium, the maximum water content at the interface was 14 water molecules per sulfid acid group at a temperature of 30 °C. At the time Springer et al. wrote their article, there was no data available for the water uptake of the membrane in equilibrium with water vapor at the surface at 80 °C. For that reason. Therefore, the assumption was made that relation (5-16) could also be used at 80 °C.

Nafion has different capacities for holding water in the saturated vapor and liquid phase. This phenomenon is referred to as Schroeder’s paradox. Nafion has a greater capacity to absorb water in the liquid phase than in the vapor phase. Springer et al. compensated for this by letting the membrane water content increase up to 16.8 when the mole fraction of water exceeds the saturation value.

$$1 \leq \frac{x_{\mathrm{w}} p}{p_{\mathrm{sat}}} \leq 3, \lambda = 14 + 1.4\left(\frac{x_{\mathrm{w}} p}{p_{\mathrm{sat}}} - 1\right) \qquad \text{(5-17)}$$

In relation (5-14), the water flux resulting from diffusion is related to the gradient of the chemical potential. The coordinate x' goes through the membrane and takes into account the swelling of the membrane when it absorbs water. As tracking the swelling of the membrane is a complicated procedure, Springer et al. chose to replace the coordinate x' with a coordinate x which is orthogonal to a dry membrane. In order to be able to use this coordinate the diffusion coefficient D' has to be corrected for the swelling.

The diffusive water flux can be rewritten with this coordinate with the dry membrane as a reference as shown in equation (5-14). When a dry membrane is taken as a reference, D_λ is the diffusion coefficient. Relationship (5-16) for the membrane water content can be differentiated to the to find $\frac{da}{d\lambda}$ and substituted into (5-18) to find an expression for D_λ. This expression is derived for the membrane water content at 30 ºC.

$$D_{\lambda,30\mathrm{C}} = \left(\frac{1}{(1+s\lambda)^2}\frac{\lambda}{a(17.81-79.7a+108a^2)}\right)D' \tag{5-19}$$

The value for s was determined to be 0.0126 by considering the thickness of a dry and fully hydrated Nafion 117 membrane. For a certain value of λ, the equation for the water content at 30 ºC is solved implicitly in order to find the water vapour activity a. In figure 5.4, the intradiffusion coefficient and the corrected diffusion coefficient are depicted for varying water contents. It should be noted that the corrected diffusion coefficient can be modelled by a cubic polynomial if $\lambda > 4$. Springer et al. correct this polynomial with an activation energy term in order to use it at different temperatures.

$$D_{\lambda>4} = 10^{-6}\times\exp\left[2416\left(\frac{1}{303}-\frac{1}{273+T_{\mathrm{cell}}}\right)\right](2.563-0.33\lambda+0.0264\lambda^2-0.000671\lambda^3) \tag{5-20}$$

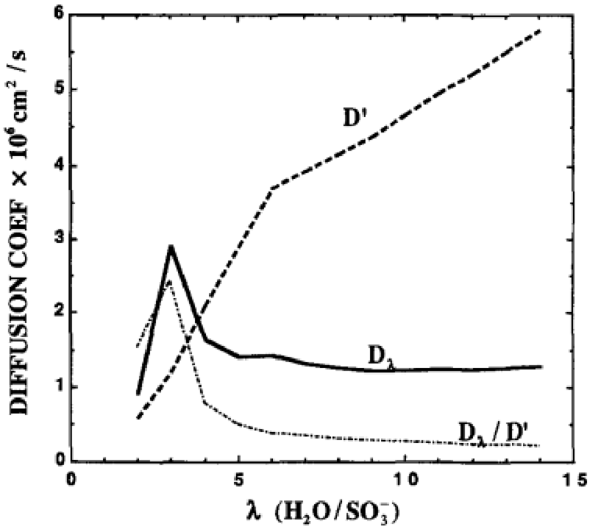

Figure 5.4: The measured intradiffusion coefficient D' by Zawodzinski and D_λ, the diffusion coefficient corrected for membrane swelling at 30 ºC [17]

Springer et al. conducted experiments in which the number of water molecules dragged per H^+-ion as a consequence of an electric field over a Nafion 117 membrane was measured. The following linear relation between the membrane water content λ and the amount of water molecules per H^+-ion was established:

$$\xi(\lambda) = \frac{2.5\lambda_{(30)}}{22} \tag{5-21}$$

The parameter $\xi(\lambda)$ defined in (5-21) is referred to as the electro-osmotic drag coefficient. By multiplying this coefficient with the current, the water flux [mol/(m^{2}s)] through the membrane as a consequence of electro-osmotic drag can be found:

$$\dot{N}_{W,\mathrm{drag}} = 2I\xi(\lambda) \tag{5-22}$$

The net water flux through the membrane in Springer's model is defined by the difference in electro-osmotic drag and back-diffusion.

$$\dot{N}_W = \dot{N}_{W,\mathrm{drag}} - \dot{N}_{W,\mathrm{dif}} = \alpha I = \frac{n_{\mathrm{drag}} I\lambda}{11} - \frac{\rho_{\mathrm{dry}}}{M_{\mathrm{m}}} D_\lambda \frac{d\lambda}{dx} \tag{5-23}$$

The gradient of the water content λ through the membrane is consequently defined as

$$\frac{d\lambda}{dx} = \left[\frac{\lambda\xi(\lambda)}{11} - \alpha\right] \frac{IM_{\mathrm{m}}}{\rho_{\mathrm{dry}} D_\lambda(\lambda)} \tag{5-24}$$

When this relation is integrated from the interface of the membrane and the anodic electrode, the water distribution throughout the membrane can be found. The water concentration at the respective interface should be used as a boundary condition.

Vetter model

Vetter et al. [35] constructed a model based on the foundational work laid by Springer et al. Vetter's diffusion coefficient for water in the membrane is prescribed by a polynomial fitted to experimental data gathered by Mittelsteadt and Staser. [36]

$$D_\lambda = \epsilon_{\mathrm{i}}^{1.5} \frac{3.842\lambda^3 - 32.03\lambda^2 + 67.74\lambda}{\lambda^3 - 2.115\lambda^2 - 33.013\lambda + 103.37} 10^{-6} \frac{\mathrm{cm}^2}{\mathrm{s}} \times \exp\left[\frac{20\ \mathrm{kJ/mol}}{R}\left(\frac{1}{T_{\mathrm{ref}}} - \frac{1}{T_{cell}}\right)\right] \tag{5-25}$$

The term ϵ_{i} is the volume fraction of ionomer in the membrane. For the electro-osmotic drag coefficient Vetter, used $\xi\ (\lambda)$ as determined by Springer in (5-21). Furthermore, the relation for the water content λ determined by Zawodzinski at 30 ºC in Nafion® 117 was used to insert in the relation for the diffusion coefficient of water in the membrane given in (5-25).

In the model proposed by Vetter et al., water crossover due to hydraulic permeation is neglected. Furthermore, Schroeder's paradox is not taken into account. This means the model does not account for the influence of liquid water on the membrane properties. In addition, water droplet formation at the interface of the gas diffusion layer and gas flow channel is not considered.

Nguyen & White model

The water crossover model presented by Nguyen and White in 1993 is a steady-state 2D-model. The fuel cell is modelled as a membrane with integrated electrodes, with two flow channels on both sides. Like the models proposed by Springer et al. and Vetter et al., the model proposed by Nguyen and White [37] only incorporates water transport by electro-osmotic drag and back-diffusion. Water crossover as a consequence of hydraulic permeation is neglected.

Nguyen and White make a number of assumptions in the model. First of all, the temperature in the components of the galvanic cells such as the bipolar plates, electrodes, and membrane is assumed to be constant due to their high thermal conductivity. This means the model is isothermal. The flow within the gas flow channels is considered a plug flow and the pressure drop along the gas flow channels is neglected. Water leaves and enters the gas flow channels from the electrodes and membrane only in the vapor phase. Gas diffusion in the electrodes is neglected as Nguyen and White assume their thickness to be very small. The gas mixture in the flow channels is assumed to be an ideal gas mixture. The volume of liquid water present in the MEA is assumed to be negligible and exists in the form of tiny droplets.

In their experiments Nguyen and White observed that at current densities over 1 A/cm^2, the water crossover flux from the cathode to the anode is insufficient to keep the membrane hydrated on the anode side. They proposed to humidify the anode stream as a solution. Moreover, as the activity of water on the anodic face of the membrane is lower, Nguyen and White use it to calculate the electro-osmotic coefficient and the diffusion coefficient more conservatively.

The molar flux of water vapour [mol/(cm^{2}s)] in and out the membrane from the anode and cathode is defined as:

$$\dot{N}^{\mathrm{V}}_{\mathrm{w,y,a}}(x) = \frac{\alpha I(x)}{F}, \qquad \dot{N}^{\mathrm{V}}_{\mathrm{w,y,c}}(x) = \frac{(1+2\alpha)I(x)}{2F} \tag{5-26}$$

The local current density $I(x)$ varies along the gas flow channels as the membrane water content and the electrode potential change along the channel. The concentration gradient across the membrane was linearized, which leads to the following expression for the NWTC:

$$\alpha = \xi(\lambda) - \frac{F}{I(x)} D_W \frac{(c_{w,c} - c_{w,a})}{t_m} \tag{5-27}$$

In relation (5-27) Nguyen and White use the activity of water on the anode side a_a to calculate the electro-osmotic drag coefficient $\xi(\lambda)$. Another approach would have been to use the average water activity between the cathode and anode, but the anode activity is a more conservative approach. Therefore, the model proposed by Nguyen and White should predict lower water crossover rates than the other models.

Nguyen and White proposed a diffusion coefficient for water in Nafion membranes and an electro-osmotic drag coefficient. The electro-osmotic drag coefficient as a function of the anodic water activity is specified as:

$$\begin{cases} \xi(\lambda) = 0.0049 + 2.02a_a - 4.53a_a^2 + 4.09a_a^3 \text{ for } a_a \leq 1 \\ \xi(\lambda) = 1.59 + 0.159(a_a - 1) \text{ for } a_a > 1 \end{cases} \tag{5-28}$$

The diffusion coefficient of water in the Nafion membrane was determined as:

$$\begin{cases} D_w = (0.0049 + 2.02a_a - 4.53a_a^2 + 4.09a_a^3) D^0 \exp\left[2416\left(\frac{1}{303} - \frac{1}{273+T_{\mathrm{cell}}}\right)\right] \text{ for } a_a \leq 1 \\ D_w = (1.59 + 0.159(a_a - 1)) D^0 \exp\left[2416\left(\frac{1}{303} - \frac{1}{273+T_{\mathrm{cell}}}\right)\right] \text{ for } a_a > 1 \end{cases} \tag{5-29}$$

In equation (5-29), D^0 is a constant equal to 5.5×10^{-7} cm^2/s. In figure 5.5, Nguyen and White's diffusion coefficient is compared to Zawodzinski's and to a diffusion coefficient by Fuller et al. [38] It should be noted that Nguyen and White's model provides a more conservative estimate for the diffusion coefficient.

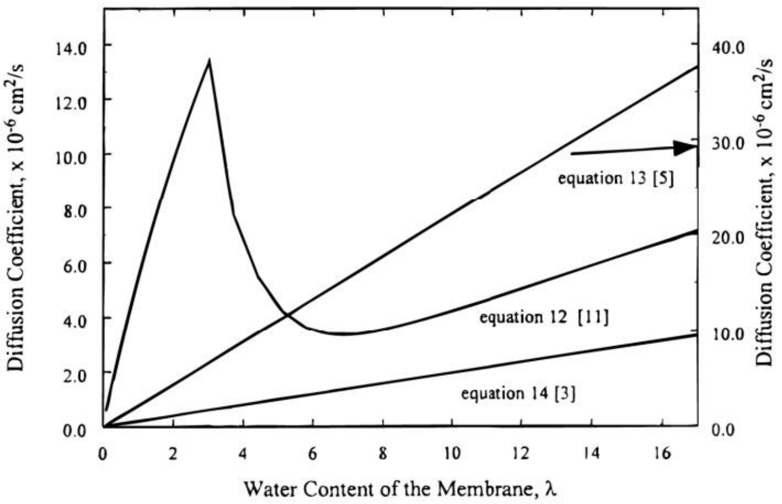

Figure 5.5: The diffusion coefficient of water in the membrane against λ according to Zawodzinski (eq. 12), Fuller (eq. 13), and Nguyen and White (eq. 14) [39]

Motupally diffusion coefficient

Another attempt to quantify the diffusive water flux over a Nafion membrane (105/115 series, 127 µm) was made in a study published by Motupally et al. in 2000. [39] Motupally et al. only proposed a different diffusion coefficient for the membrane, the other crossover mechanisms were not taken into consideration in their paper. The diffusion coefficient was determined in a fuel cell set-up where on one side of the membrane water at 80 ºC was fed while nitrogen was fed to the channels on the other side of the membrane. In Motupally's experiments to determine the water flux, the flow rate of nitrogen was varied to control the water activity on the surface of the membrane.
The diffusion coefficient proposed by Motupally et al. as a function of the membrane water content and cell temperature is:

$$\begin{cases} D_{\mathrm{w}} = 3.10 \times 10^{-3}\lambda\left(-1+e^{0.28\lambda}\right)\exp\left[\frac{-2436}{T_{cell}}\right] \text{for } 0 < \lambda \leq 3 \\ D_{\mathrm{w}} = 4.17 \times 10^{-4}\left(1+161e^{-\lambda}\right)\exp\left[\frac{-2436}{T_{cell}}\right] \text{ for } 3 < \lambda \leq 17 \end{cases} \tag{5-30}$$

Motupally et al. used an isotherm determined by Hinatsu et al. [40] for the water content of Nafion at 80 ºC.

$$\lambda = 0.3 + 10.8a_w - 16.0a_w^2 + 14.1a_w^3 \tag{5-31}$$

In their research Motupally et al. compared the water flux calculations resulting from those diffusion coefficients with water flux measurements through Nafion© 105/115. It was determined experimentally that the diffusion coefficient determined by Zawodzinski et al. with nuclear magnetic resonance technique integrated in Springer et al.'s model most accurately predicted the water flux. Over a range of pressures and flow rates, the measured flux never differed more than 5% from the water flux calculated with Zawodzinski's diffusion coefficient.

Motupally et al. disregarded a number of assumptions made by Springer et al. First of all, the concentration of water is water is considered uniform across the electrode and gas flow channel in the z-coordinate as the Nafion membrane is the dominant resistance to water transport. Furthermore, Motupally et al. neglect the swelling of the membrane when water is absorbed. The thickness of a dry membrane is taken equal to the thickness of a hydrated membrane. This assumption was made as the membrane in their test set-up was sandwiched between two bipolar plates under high pressure.

Kulikovsky water crossover model

The water crossover model proposed by Kulikovsky [42] is a relatively recent contribution to the literature dating from 2019. A main difference between this model and the models discussed earlier is that it also considers Knudsen diffusion of water in the catalyst layer. In the catalyst layer, the pore diameter is around $3 \cdot 10^{-2}$ µm. The mean free path of reactants in the catalyst layer is of a similar order. This means besides Knudsen diffusion significantly contributes to the transport of mass besides Fickian diffusion. The Knudsen diffusion coefficient for water in a catalyst layer is given by the following relation:

$$D_w^K = \zeta r_{cl} \sqrt{\frac{8RT}{\pi M_w}} \tag{5-32}$$

In the definition for the Knudsen diffusion coefficient (5-32), r_{cl} is the mean pore radius of the catalyst layer, M_w the molecular weight of water, and ζ the correction factor for the average thermal velocity of the molecules.

The diffusive transport of water through the membrane in the Kulikovksy model is governed by a diffusion coefficient determined by van Bussel et al.: [43]

$$D_w = 4.1 \cdot 10^{-6} \left(\frac{\lambda}{25}\right) \left[1 + \tanh\left(\frac{\lambda - 2.5}{1.4}\right)\right] \ \mathrm{cm^2 s^{-1}} \tag{5-33}$$

It should be noted that the diffusion coefficient tends to zero as the water content λ approaches zero. The osmotic drag coefficient in this model is also taken from measurements carried out by van Bussel et al.:

$$n_d = \begin{cases} 1, & \lambda < 9 \\ 0.117\lambda - 0.0544, & \lambda \geq 9 \end{cases} \tag{5-34}$$

Kulikovsky assumes the anode and the cathode are operated at the same pressure, meaning hydraulic permeation is neglected. The overall water transport over the membrane is described by the following equation:

$$N_w = -D_w(\lambda)\Delta c_w + \frac{n_d(\lambda) j_p}{F} \tag{5-35}$$

Water crossover in reinforced membranes

The water crossover models presented in this chapter so far were all created with assumptions based on Nafion membranes. These membranes consist purely of the ionomer used for the transport of protons. Nowadays, membranes applied in PEM fuel cell stacks are much thinner than the Nafion membranes used in the studies discussed and contain a reinforcement structure. In 1995, W.L. Gore & Associates introduced Gore-select® membranes. These membranes consist of a porous PTFE sheet containing an ionomer. This sheet serves as a reinforcement structure and therefore these membranes contain less perfluorinated ionomer than Nafion membranes. [44]

Ye and Wang [34] were the first to report on the water transport properties of Gore-select® membranes in 2007. They measured the electro-osmotic drag coefficient and the diffusion coefficient of water in 18 µm and 25 µm thick membranes and proposed in-situ measurement techniques for these properties. [34]

Most techniques used by researchers to measure the diffusion coefficient of water in membranes and the electro-osmotic drag coefficients are based on ex-situ experiments. Few models are based on measurements in operating fuel cells as these are hard to conduct. [34] In-situ experiments allow for investigation of the membrane properties under current load and the environmental conditions of an operating fuel cell. The water flux in the gas flows at the inlet and the outlet on both sides of the fuel cell was measured by trapping water in gas-drying columns.

The method for measuring the electro-osmotic drag coefficient proposed by Ye and Wang relies on a multilayer membrane. This 200 μm thick membrane is constructed of multiple individual Gore-Select membranes through hot-pressing. Diffusion from the cathode to the anode can be neglected at such thicknesses. Therefore, the electro-osmotic drag mechanism can be evaluated without interference from diffusion. Two hydrogen flows of approximately equal relative humidity were fed to the fuel cell.

In figure 23, the flux of water J_{EOD} [mol/cm^{2}s] multiplied with the x, which appears to be a time scale judging from dimensional analysis, and Faraday's constant is plotted against the current density I [A/m^2]. The slope of the line is the electro-osmotic drag coefficient $\xi(\lambda)$ which was found to be equal to 1.07. It should be noted that in figure 5.6 that electro-osmotic drag is a transport mechanism which is independent of the relative humidity of the hydrogen flows, which was varied between 45% and 95%.

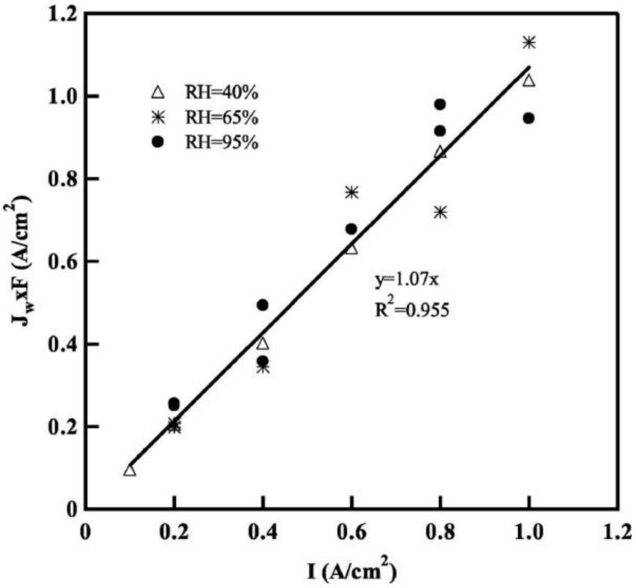

Figure 5.6: Electro-osmotic drag coefficient in Gore-Select multilayer membranes (200 μm) [34]

Ye and Wang conducted measurements on a Nafion membrane as well and found the electro-osmotic drag coefficient to be 1.10 in this case. They concluded that the electro-osmotic drag transport mechanism is not greatly affected by the reinforcement structure in Gore-Select membranes. In figure 5.6, the electro-osmotic drag coefficients found in various studies for Nafion are compared to the measurements for Nafion membranes by Ye and Wang.

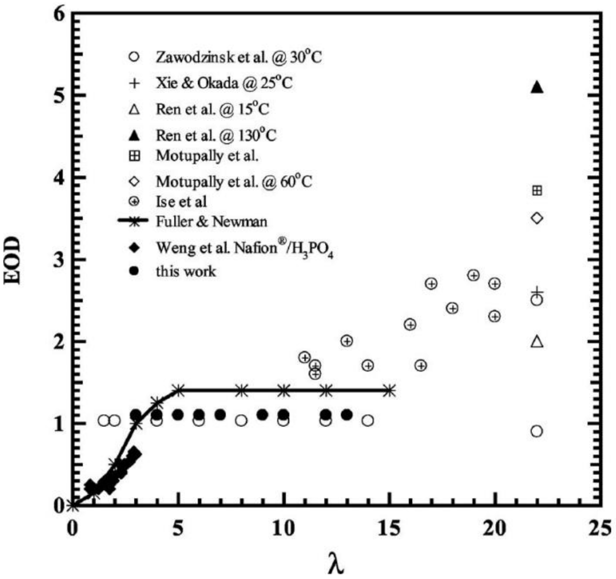

Figure 5.7: Electro-osmotic drag coefficients in various studies [34]

Figure 5.7 illustrates that the value for the electro-osmotic drag coefficient found by Ye and Wang for Nafion membranes is in the same order of magnitude as values found in different studies in the water content range of 4 to 15 water molecules per sulfonic acid group.

The water concentration on the interface of the membrane and the cathode catalyst layer was measured with the high frequency resonance technique. The following fit for the membrane proton conductivity as a function of the water activity was determined using these measurements:

$$\kappa = 0.12\alpha^{2.80} \tag{5-36}$$

Relationship (5-36) is visualized in figure 5.8.

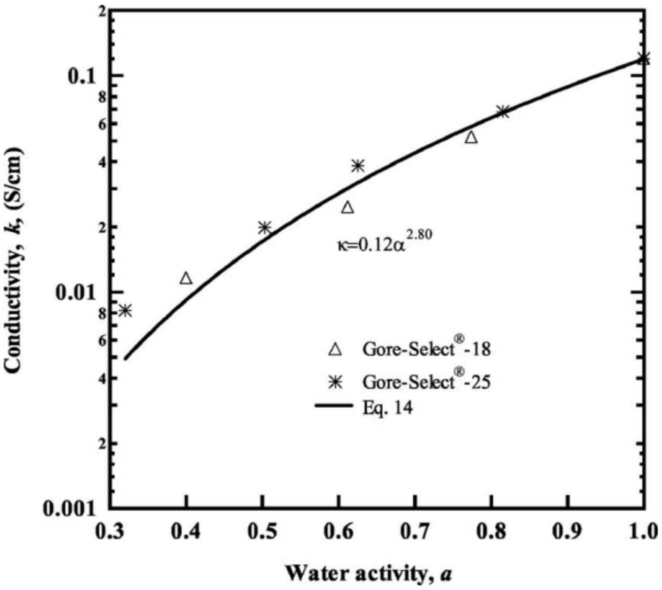

Figure 5.8: Proton conductivity as a function of water activity in Gore-Select membranes [34]

Furthermore, Ye and Wang evaluated the diffusion coefficient of water in Gore-Select membranes of a thickness of 18 and 25 µm. As the diffusion coefficient determined by Zawodzinski is commonly referred to in literature it was chosen as a starting point. Furthermore, there is a great chemical similarity in the ionomer in Gore-Select membranes and Nafion membranes. Zawodzinski's expression for the diffusion coefficient of water in Nafion membranes was multiplied with a correction factor k.

$$D_{\lambda>4} = k \times 10^{-6} \exp\left[2416\left(\frac{1}{303} - \frac{1}{273+80}\right)\right] \times (2.563 - 0.33\lambda + 0.0264\lambda^2 - 0.000671\lambda^3) \qquad (5\text{-}37)$$

The correction factor k presented in equation (5-37) was found to fall in a range of 0.3 to 0.7 (Figure 5.9) in most cases. It appears there is a slight downward trend in the scaling factor with increasing membrane water content. This could perhaps be explained by the fact that at lower water contents the main barrier to diffusive water transport is the reduced interconnectivity between the ionomer strains (Figure 3.5) instead of the reinforcement structure. This trend is more pronounced for Gore-Select membranes of 25 µm thickness.

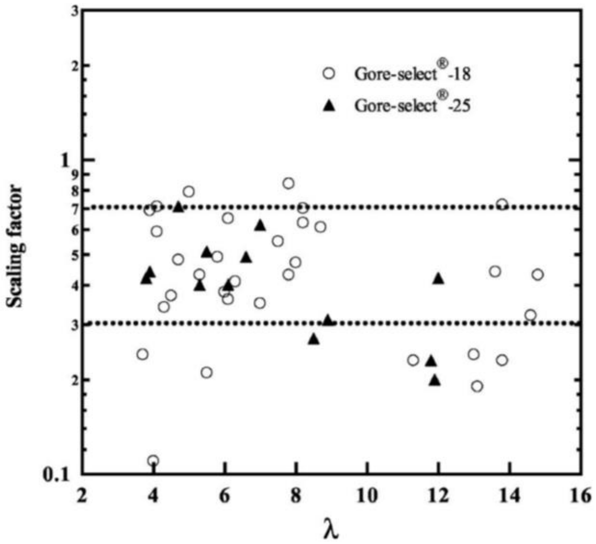

Figure 5.9: Diffusion coefficient scaling factor vs. membrane water content [34]

Figure 5.10 compares some of the diffusion coefficients reported in Nafion with Ye and Wang's corrected diffusion coefficient for Gore-select membranes against the membrane water content. When evaluating figures 5.9 and 5.10, it should be noted that the diffusion coefficient of water in the reinforced Gore-Select membrane is significantly lower than in non-reinforced Nafion membranes.

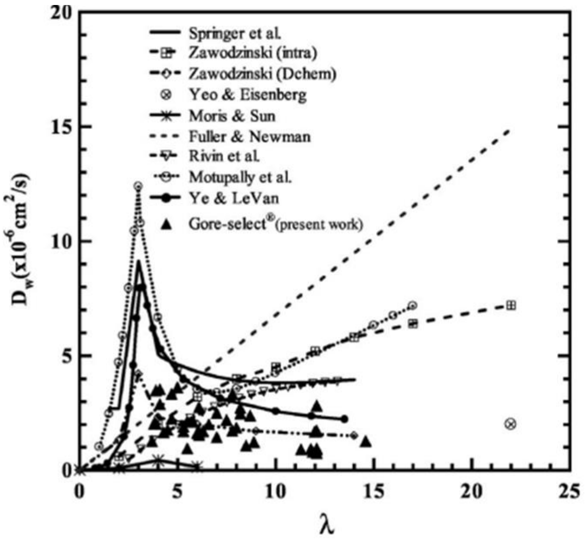

Figure 5.10: Water diffusion coefficients in Gore-Select and Nafion membranes [34]

The main conclusions of this study are that the electro-osmotic drag coefficients in Nafion and Gore-select membranes were not affected by the reinforcement structure and relative humidity of the gas flows. Crossover by diffusion is significantly impeded, however.

Water crossover through thermo-osmosis

As of yet, the galvanic cell was assumed to be isothermal in every water crossover model. A transport mechanism disregarded in the earlier discussed models is thermo-osmosis. The driving force of this mechanism is a temperature gradient from one side of the membrane to the other. For hydrophobic membranes such as Nafion and Gore-Select, water typically flows from the cold to the hot side of the membrane. Due to the heat produced in the cathodic reaction, this side of the membrane is usually at a higher temperature. This means that water flows from the anodic side of the membrane to the cathodic side. The water flux over the membrane as a consequence of this thermos-osmosis is proportional to the temperature gradient and increases with the average membrane temperature: [45]

$$J_T = -D_T \nabla T \tag{5-38}$$

In equation (5-38), D_T is the thermo-osmotic diffusivity and ∇T the temperature gradient across the membrane. The following empirical relation (5-39) for the thermos-osmotic diffusivity was determined for Gore-Select membranes (18 μm) by Kim and Mench: [46]

$$D_T = -[1.66 \pm 0.15] \times 10^{-5} e^{-\left(\frac{2297 \pm 36}{T_{\text{membrane}}}\right)} \tag{5-39}$$

It should be noted that at higher membrane temperatures, D_T increases in magnitude. Therefore, thermo-osmosis becomes an increasingly important transport mechanism at higher currents. The temperature at the interface of the membrane and the cathode catalyst layer where the oxygen reduction reaction takes place, can be at a 1 ºC higher temperature than the bulk of the membrane when a fuel cell is operated at 1 A/cm^2.

In figure 5.11, the water flux as a consequence of thermo-osmosis is compared for three membranes. The membranes used in the experiments were a Gore-Select membrane (18 μm), a Nafion 112 membrane (50 μm), and a reinforced Flemion membrane (50 μm). It should be noted that the water flux in the Gore-Select membrane was significantly higher than in the other membranes. This can be attributed to the greater temperature gradient due to the smaller thickness of the Gore-Select membrane.

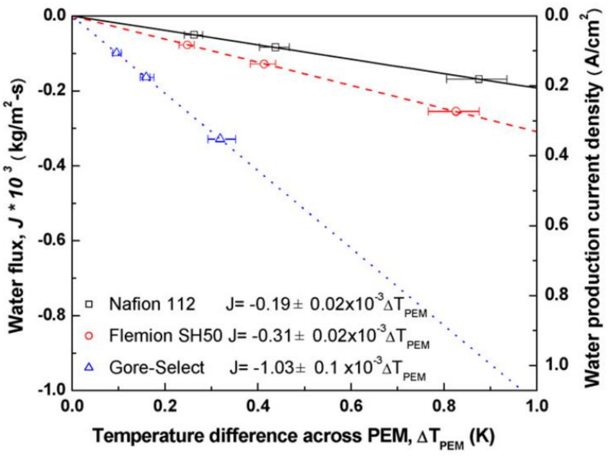

Figure 5.11: Thermo-osmotic flux across the membrane in Nafion® 112 (50 μm), Gore-Select® (18 μm), and Flemion SH50 (50 μm) [46]

When the thickness of the membrane is taken into account, the temperature gradient would be approximately 2.8 times as large in the Gore-Select compared to the Nafion and Flemion membranes for the same temperature difference across the membrane. Comparing the Flemion membrane to the Nafion membrane, it should be noted that the thermos-osmotic water flux is approximately 1.5 times larger. (Figure 5.11) For the Gore-Select membrane it's even twice as big after a correction for the membrane thickness. It appears that the thermos-osmotic transport mechanism plays a much greater role in reinforced membranes than in those consisting solely of the ionomer. Furthermore, Kim and Mench observed a greater flux in membranes with a lower equivalent weight.

It should be noted that there is no consensus on the net flow direction. In other studies, a flow from the hot to the cold side of the membrane was observed. Kim and Mench hypothesize that this is due to the different hydrophobicity of the gas diffusion layers and catalyst layers attached to the membranes used in the studies.

In reality, it is challenging to quantify the water crossover due to thermos-osmosis as it is no sinecure to get a picture of the in-plane temperature distribution of the membranes in an operating fuel cell. Kim and Mench assumed a uniform temperature over the surfaces of the membranes. The water flux at a temperature difference from the cold to the hot side of the membrane for a temperature difference of 0.3 for a Gore-Select membrane is comparable to the water production at 0.4 A/cm^2.

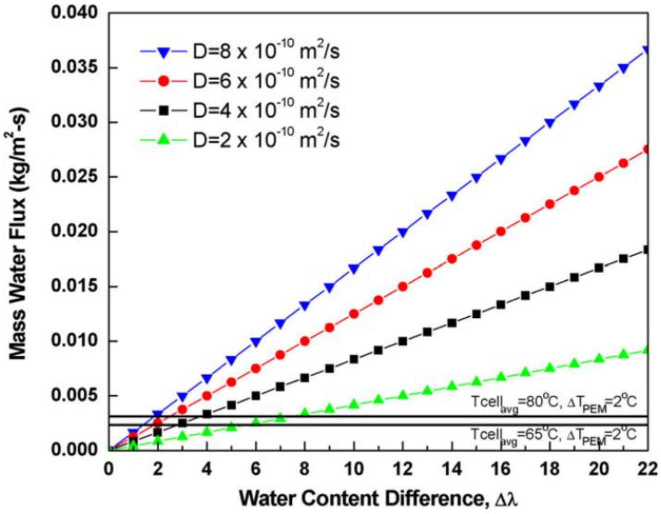

Figure 5.12: Thermo-osmotic flux compared to diffusion flux in a Gore-Select® membrane (18 µm) [46]

In figure 5.12, the water flux by thermo-osmosis in the membrane is compared to the diffusive flux of water over a Gore-Select membrane of 18 µm. The diffusive flux is visualized for four different magnitudes of the diffusion coefficient, whereas the thermo-osmotic flux is given at 65 ºC and 80 ºC with a temperature difference of 2 ºC over the membrane.

Additionally, Kim and Mench [45] also suggested including a term for the transport by phase change in the gas diffusion layer. This follows the saturation pressure gradient from a hot to a cold region. The water flux in the gas diffusion layer as a consequence of phase change is given by:

$$J_{\mathrm{c}} = -\rho_{\mathrm{w}} k_{\mathrm{rw}} \frac{k_{\mathrm{w}}}{\mu_{\mathrm{w}}} \nabla p_{\mathrm{w}} \qquad (5\text{-}40)$$

In equation (5-40), ρ_{w} is the density of liquid water, k_{rw} is the relative water permeability, k_{w} is the water permeability, μ_{w} is the water viscosity, and p_{w} is the saturation pressure. The higher the temperature in the cell, the more important the phase-change induced water transport becomes. Furthermore, it is also strongly affected by the effective diffusivity in the gas diffusion layer. The effective diffusivity is the diffusion coefficient divided by the tortuosity of the gas diffusion layer. This in turn varies with the clamping force the cells are held together with.

Effect of inlet gas humidification on membrane water crossover

The humidification of the oxygen and hydrogen fed to the stack influences the water crossover rate from the cathode to the anode. According to Huang, Hwang, and Lai, [47] the anode humidity is the determining factor for the performance of a PEM fuel cell. The approach to water management suggested is to control the temperature of the gas streams into the fuel cell in order to control the relative humidity. In order to displace water from the relatively humid side of the membrane to the dryer side, the gas on the humid side should be heated up. In this manner flooding and drying out can be prevented.

Kim [48] conducted a study on the effect of the relative humidity of the gases fed to a 6 kW PEM fuel cell stack on the current density distribution along the interface of the catalyst layer and the gas diffusion layer and liquid water saturation. A series of measurements were taken at a cell voltage of 0.5 and 0.7 V a cathode relative humidity of 100%. When the cathode was saturated, a higher relative humidity of the hydrogen feed resulted in a greater presence of liquid water saturation at the interface of the cathodic gas diffusion layer and the catalyst layer. When hydrogen was fed at lower relative humidities, there was less liquid water at the interface of the cathode catalyst layer and gas diffusion layer. This indicates that a higher relative humidity of the hydrogen feed to the stack leads to a lower water crossover due to suppressed back-diffusion.

At an operating voltage of 0.5 V, a higher anode relative humidity resulted in a noticeably lower penetration of hydrogen to the catalyst layer. At an operating voltage of 0.7 V, the local current densities at the interface were unaffected by the relative humidity of the hydrogen feed. At the cell voltage of 0.5 V, a maximum in the current density distribution at the interface could be seen at a relative humidity of the hydrogen flow of 60%. (Figure 5.13) At a relative humidity higher than 60%, the hydrogen molecules experience more resistance in reaching the catalyst layer. This means higher mass transfer potential losses and a greater risk of flooding. Due to the crossover from the cathode to the anode, the humidity of the hydrogen flow increases along the length of the gas flow channel.

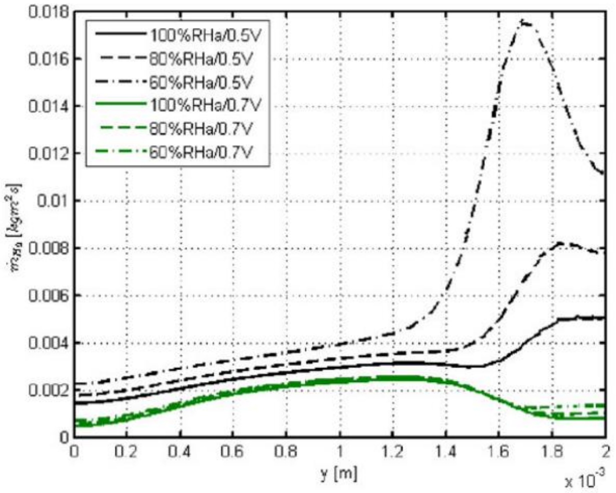

Figure 5.13: Effect of the H2 RH on the H2 mass flow rate along the GDL-CL interface at the operating voltages of 0.5 and 0.7 V. [48]

Effect of anode and cathode stoichiometry on membrane water crossover

Kim [48] also investigated the influence of the anode and cathode stoichiometry on the performance of the fuel cell stack. The stoichiometry is defined as the ratio of the reactant supply and the reactant consumption. Flow rates above the critical stoichiometric flow rate are able to drain water and evaporate it from the gas flow channels. The critical stoichiometry is defined as:

$$\zeta = 0.29\left(\frac{p}{p_{\mathrm{sat}}(T)} - 1\right) + 0.44 \quad (5\text{-}41)$$

Below the critical stoichiometry presented in (5-41), there will be a build-up of liquid water. Increasing the anode stoichiometry also relieves the cathode side from liquid water. A higher anode stoichiometry lowers the water concentration at the interface of the anode catalyst layer and the membrane, stimulating back-diffusion from the cathode to the anode. Raising the cathode stoichiometry has the opposite effect on the water crossover rate as it lowers the water concentration on the interface between the cathode catalyst layer and the membrane.

II

Methodology:

Modelling the PowerCell stack and anode subsystem

6 Methodology stack modelling

The starting point for a comprehensive anode subsystem model is capturing the characteristics of PowerCell's fuel cell stack. As discussed in chapter 5, the fuel cell stack serves as a gateway for water into the anode subsystem. Accurately modelling the water crossover is therefore of great importance. Additionally, including the interaction between processes at a system level and processes within the stack would provide invaluable insight in the coupling of degradation mechanisms and the system operating parameters. This would allow for investigation into the influence of the system operating parameters on the instantaneous power density and on degradation mechanisms in the long term.

Gamma Technologies is a software company which markets a Multiphysics simulation platform called GT-Suite which includes a PEM fuel cell stack model. This PEM fuel cell stack model can be fitted to experimental data to mimic the behavior of the stack of the end-user. Furthermore, the geometrical properties of the end-user's stack can be included. The model provides an overview of processes within the stack under certain boundary conditions derived from the system operating parameters. In this manner, the effect of the system operating parameters on, for example the water content of the membranes or the activation potential losses can be monitored. With these considerations in mind, GT-Suite and its PEM fuel cell stack model were used in an attempt to simulate PowerCell's stack.

Fitting of the PEM fuel cell stack model to experimental data

A dataset (T0042) to fit the PEM fuel cell model on, was provided by PowerCell's industrial partner Bosch. This dataset contains the results of 661 experiments on a 20-cell stack in steady-state operation in a test station conducted by Bosch. The bipolar plates and the MEAs of this 20-cell stack are identical to those applied in PowerCell's full-size stack. In these experiments the operating parameters of the stack were varied while measuring among others the cell voltage against the current density, the mass flow rates of the reactants, and the water crossover rate from the cathode to the anode. The operating parameters which were varied and recorded were for instance: the inlet relative humidity of the reactants, the temperature of the inlet flows, and the operating pressures of the anode and cathode.

A random sample of 25 datapoints was taken from T0042 and inserted in the case set-up in GT-Suite. The case set-up holds the information from the datapoints regarding the measured voltage at a certain current density, the measured water crossover rate, and the operating parameters at which the experiment was conducted. Using these datapoints three parameters of the PEM fuel cell model were subsequently fitted targeting the measured voltages inserted in the case set-up. These parameters were the first Springer coefficient b_{11}, the tortuosity, and the catalyst specific surface area.

The first Springer coefficient b_{11} is a parameter which influences the proton conductivity of the membranes according to the following relation:

$$\sigma_m = (b_{11}\lambda - b_{12})\exp\left(b_2\left(\frac{1}{303} - \frac{1}{T_{cell}}\right)\right) \tag{6-1}$$

The tortuosity is the ratio between the path length reactants have to traverse in a porous electrode and the distance between the end points of the path. It is therefore always greater than 1. Finally, the catalyst specific surface area is the area of the catalyst particles per volume unit. These three parameters were recommended by Gamma Technologies as they affect three different potential loss mechanisms and come with some uncertainty. The first Springer coefficient b_{11} affects the Ohmic potential losses, the tortuosity affects the mass transfer potential losses, and the catalyst specific surface area affects the activation potential losses.

In this manner, the stack model was trained to predict the voltage at a certain current density and operating conditions. After running the optimizer tool, the optimal values for b_{11}, the tortuosity and the catalyst specific surface area were inserted into the PEM fuel cell stack model. Subsequently, a simulation was run to investigate the prediction by the stack model for the water crossover rates based on the 25 experiments inserted in the case set-up. The same stack model was used to evaluate 11 experiments carried out in a test station at PowerCell's facilities. The resulting predictions for the water crossover rates in these experiments were compared to the measured values.

Unfortunately, an estimated measurement error on the water crossover measurements was not provided by Bosch. PowerCell did provide an error on their water crossover measurements. The approach taken by PowerCell to determine the crossover rate was to measure the difference in the water mass flow rate at the inlet and outlet of both the anode and cathode channels of the stack and take the average value. The absolute error was taken as the difference in the two crossover rates based on the differences of the inlet and outlet mass flow rates of the anode and cathode. Two experiments conducted by Bosch were repeated in PowerCell's test station as listed in table 6.1 under the same conditions. The crossover rate at 300 A determined by Bosch was 30.3% greater than the value determined by PowerCell. At 440 A, the value found by Bosch was 12.9% smaller than the value found by PowerCell. As there are only two datapoints to compare between both datasets it is not possible to extrapolate any conclusions regarding the accuracy of crossover rate measurements in the dataset provided by Bosch. Furthermore, the sample size of PowerCell's dataset would be too small for this purpose.

Table 6.1: Comparison of Bosch's and PowerCell's water crossover measurements per cell

Test point	Crossover [g/s]	Error [g/s]	Crossover per cell [g/s]
PowerCell 300 A	0.640	0.05 (7.81%)	0.0090
Bosch 300 A	0.834	NA	0.0120
PowerCell 440 A	1.703	0.094 (5.52%)	0.0240
Bosch 440 A	1.483	NA	0.021

As the diffusion models available in the PEM fuel cell stack model were created for Nafion membranes instead of reinforced membranes, a multiplier was imposed on the diffusive crossover rate in the model. This multiplier serves as a correction factor for the presence of a reinforcement structure in the membrane used by PowerCell. A multiplier of 0.5 was taken as suggested by Ye & Wang. [34] As the mechanism of electro-osmotic drag is unaffected by the reinforcement structure, it was represented by a model created for Nafion membranes. The model chosen here was the Springer model as it was the only option.

The water crossover rates predicted by the Springer, Vetter, Motupally, Nguyen, and Kulikovsky models did not match the measured crossover rate for the 25 random datapoints from T0042. Therefore, another approach of modeling the stack and the water crossover from the cathode to the anode is presented in the next chapter.

7 Methodology anode subsystem modelling

In order to gain knowledge on the influence of the system operating parameters on the power density of the stack and degradation processes within, it is of great importance to model the stack behavior with respect to the voltage response and the water crossover phenomena. As capturing the water crossover within the stack through literature models failed, another approach will be taken to integrate the water crossover into the anode subsystem model. The anode subsystem model approaches the anode subsystem in PowerCell's PS-100 system. It consists of a hydrogen feed line, a stack assembly, water injection module, water trap, a recirculation loop powered by a pump, and a mixing chamber. The PEM fuel cell stack model has been abandoned, and only the macroscopic processes occurring in the stack are modelled. The downside of this is the absence of a directly coupled processes within the stack. The PEM fuel cell model integrated in GT-Suite allows for discretizing the stack offering insight in the processes taking place within the stack in great detail. The water crossover in the PEM fuel cell stack model is an accumulation of the crossover in the discretized section. In the approach that will be presented in this chapter, all water which crosses over from the cathode to the anode is injected at once. Monitoring the processes at a small spatial resolution is therefore impossible. Guidelines for proper operation to prevent degradation and maintain power density are therefore drawn from the literature research and will be satisfied by maintaining certain conditions on the boundary of the stack. Examples of these guidelines are maintaining a relative humidity of approximately 60% into the stack and avoiding feeding liquid water to the stack.

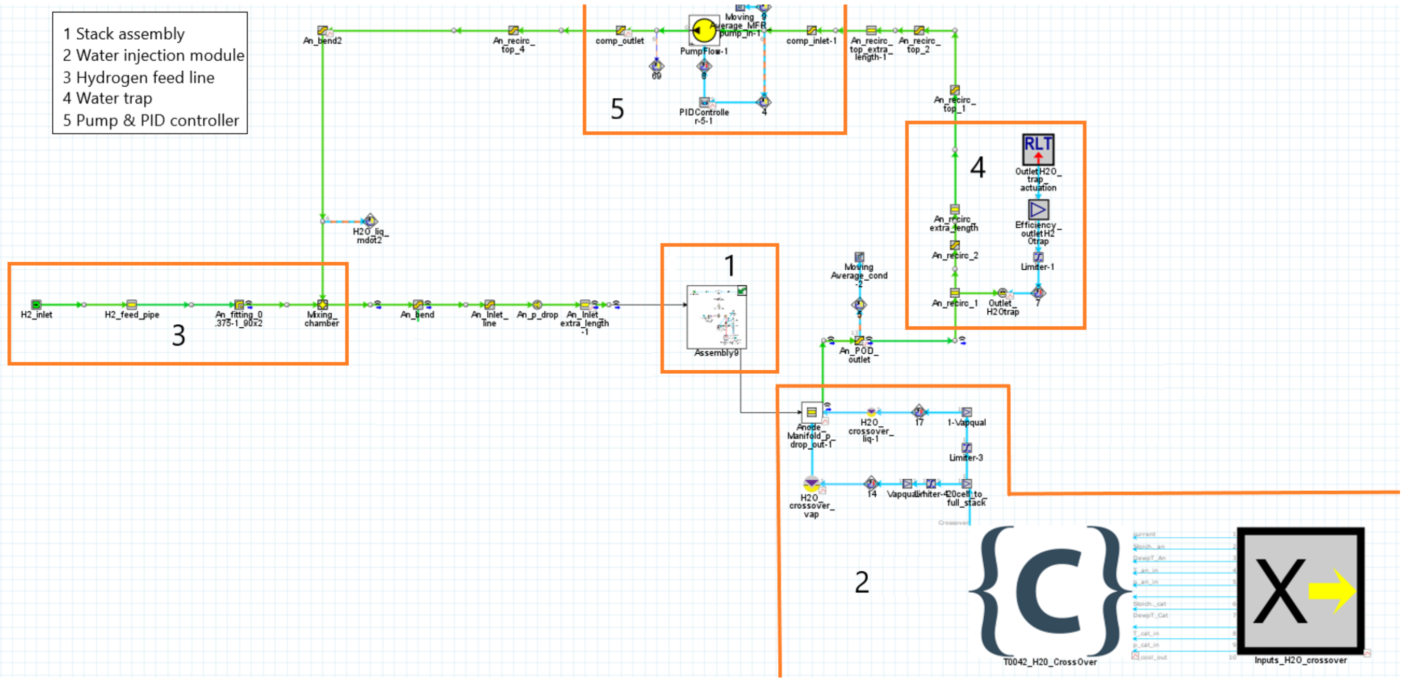

Figure 7.1: An overview of the GT-Suite anode subsystem model

In figure 7.1, an overview of the anode subsystem model in GT-Suite is given. The model is based on mass and energy balances. The roles of the model subsections from 1 to 5 listed in figure 7.1, will be explained in this chapter. As the previous chapter treated the modelling of PowerCell's stack, this subsection of the model will be treated first.

Stack subsection

As the PEM fuel cell stack model was omitted from the anode loop model, the phenomena which occur in PowerCell's stack were simulated with various templates portrayed in figure 7.2. First of all, the pressure at which the stack is operated is maintained by an accumulator tank. (1) This template enforces a certain pressure right after the inlet manifold, set by a boundary condition. (2) The consumed hydrogen in the electrochemical reaction is removed from the pipe with an ejector. (4) In the stack there is a pressure loss across the gas flow channels. As the gas flow channels are parallel to each other, the pressure drop is the same regardless of the number of cells and is imposed by the pressure drop template. (3) The pressure drops over the stack manifolds are larger in a stack with more cells but is negligible compared to the pressure drop over the gas flow channels. The heat transfer which takes place in the stack is emulated by the heat exchanger template. (6) In this template a temperature is imposed on the flow which is taken equal to the coolant outlet of the stack. The coolant outlet temperature diverges slightly from the actual stack temperature but is assumed to approach it. The water which enters the stack is ejected to prevent a build-up. (5)

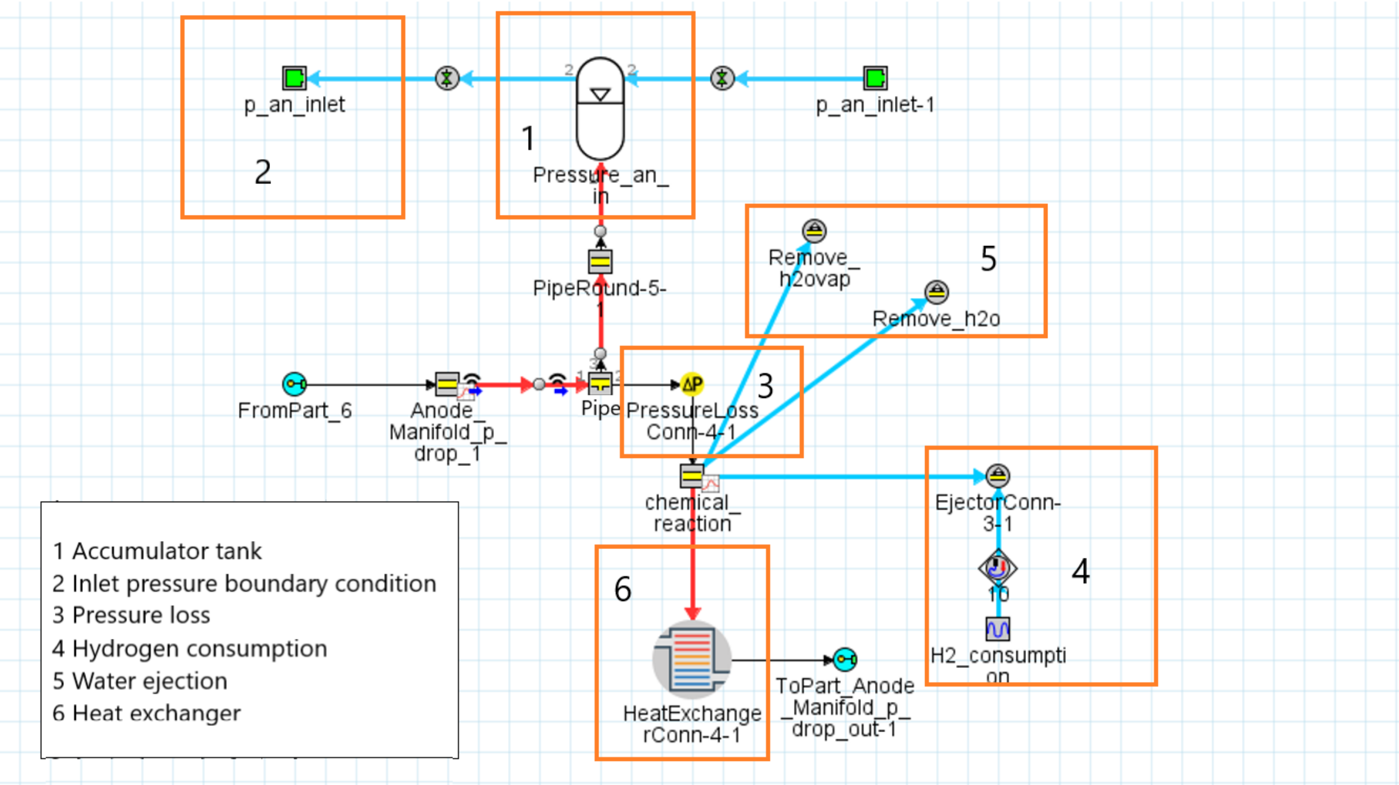

Figure 7.2: Sub-assembly of the stack

It should be noted in figure 7.2 that the water crossover rate is not modelled as part of the stack assembly. This model is introduced in the next section.

Water injection assembly

The water crossover rate in the anode subsystem model is predicted by a function programmed in C. This function is a metamodel. A metamodel is fitted to the input data (the parameters in table 7.1) and the water crossover rates recorded in T0042. [51] The metamodel used for the water crossover is of the Kriging type. A Kriging is a statistical method which predicts the water crossover rate of an unseen data point based on the datapoints fed from T0042. The datapoints that are closest to the unseen datapoints receive the most weight in the prediction. The Kriging was not trained on all 661 crossover rate measurements in the T0042 dataset provided by Bosch. Some of the measurement points with very high stoichiometries at low currents were considered outliers. At low currents it’s complicated to accurately measure the stoichiometry. The Kriging was trained on the remaining 570 experiments. After creation of the Kriging the effect of the input parameters which were also recorded in the T0042 measurements on the water crossover rate was monitored. The input parameters of the metamodel are listed in table 7.1. The expected influence of the input parameters on the water crossover rate and the source are briefly explained. The input parameters are gathered from the case set-up, the design of experiments and sensors in the anode loop. The design of experiments is a method to systematically vary parameters to the be studied. These parameters and their range are listed in table 7.3.

Table 7.1: Input parameters water crossover rate metamodel

Input parameter	**Expected effect**	**Source**
Current	At higher current more water is produced at the cathode, leading to greater crossover of water.	Case set-up
Stoichiometry anode	A higher anode stoichiometry lowers the concentration of water on the anode side of the membrane inducing stronger back-diffusion.	Design of experiments
Dewpoint temperature anode inlet	A higher dewpoint temperature at the anode inlet indicates a higher content of water in the flow going into the stack. This lowers the potential for crossover to the anode.	Sensor in circuit
Temperature anode inlet	Higher temperatures give rise to increased water transport over the membrane	Sensor in circuit
Pressure anode inlet	A higher anode inlet pressure could lower the water crossover to the anode resulting from hydraulic permeation.	Design of experiments
Stoichiometry cathode	A higher cathode stoichiometry lowers the concentration of water on the cathode side of the membrane. This leads to less diffusion to the anode side.	Design of experiments
Dewpoint temperature cathode inlet	A higher dewpoint temperature at the cathode inlet indicates a higher concentration of water going into the stack on the cathode side. This raises the potential for crossover to the anode.	Design of experiments
Temperature cathode inlet	Higher temperatures give rise to increased water transport over the membrane	Design of experiments
Pressure cathode inlet	A higher cathode inlet	Design of experiments

	pressure could increase the water crossover to the anode resulting from hydraulic permeation.	
Temperature Coolant outlet	The temperature of the coolant leaving the stack can approximately be taken equal to the stack temperature. At higher temperatures, water transport across the membrane faces less resistance.	Design of experiments

The measurements in the T0042 dataset were taken on a 20-cell stack in a test station. All the input parameters listed in table 7.1 are intensive parameters and therefore do not scale with the number of cells in the stack. The current is also an intensive parameter as the cells in the stack are connected in series. The water crossover rate is, however, an extensive parameter. It scales with the number of cells. Although the current is an intensive parameter, a certain amount of hydrogen is required to maintain the current in every cell. This means that the mass flow rates in the stack scale with the number of cells. The Kriging for the water crossover rate was integrated in the anode subsystem model (5) as shown in figure 7.3. A constant gain (7) was applied to the predicted water crossover to scale from the 20-cell stack to the full-size stack.

After multiplication of the output of the function with the gain, a limiter (1) was put in place to prevent injection of negative mass flow rates which would cause failure of the model run. A negative prediction for the water crossover rate was not expected. This limiter was integrated as a safety mechanism, however. the predicted mass flow rate is injected into the anode loop. As the injectors in GT-Suite (4) could only inject fluid mixtures in a single phase, the injection of water was split in two branches feeding liquid water and water vapor. The injection of water occurs at the inlet of the outlet manifold of the stack. A vapor quality of 0.8 was assumed in the gain block. (2) After injection an equilibrium is reached so that the mixture leaving the outlet manifold reaches the actual vapor quality. The condensation rate in the outlet manifold of the stack was monitored with a moving average template. One of the steady-state conditions of the model was for the condensation rate in the outlet manifold to reach an equilibrium value. The input parameters to the Kriging for the water crossover rate held by the C-function block, (5) were read out from a sensor (6) which took them from the sources mentioned in table 7.1.

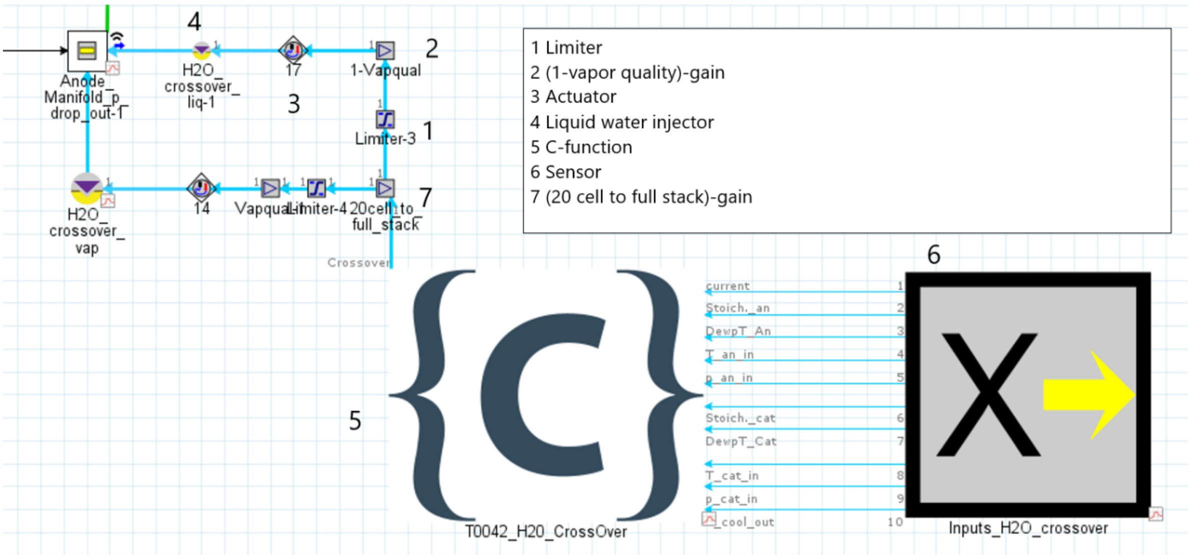

Figure 7.3: Water injection module emulating the membrane water crossover

Hydrogen feed line and mixing chamber

The hydrogen fee line in the model consisted of a Dirichlet boundary condition which set the hydrogen mass flow rate fed to the pipe leading to the mixing chamber. The amount of hydrogen fed to the system was equal to the hydrogen consumed at a certain current in the stack. Equation (4-6) gives the relation between the current and the hydrogen consumption rate per galvanic cell. The temperature at which the hydrogen was fed to the system is also set in the mass flow rate boundary condition template. (Figure 7.4) This temperature was included as a parameter in the design of experiments in table 7.3.

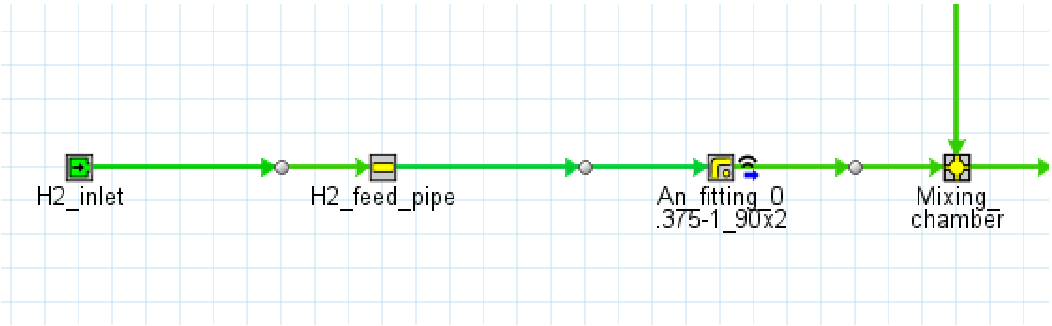

Figure 7.4: Hydrogen supply line in the anode subsystem model

The hydrogen was fed to the system as a dry flow as the anode subsystem system does not include a humidifier. The hydrogen was fed at temperatures varying between 20 ºC and 80 ºC. The freshly fed hydrogen was mixed with a mixture of recirculated hydrogen, water, and nitrogen in the mixing chamber. As the flow of fresh hydrogen could be at a much lower than the recirculated hydrogen due to the design of experiments, condensation of water vapor upon mixing could occur. The condensation rate in the mixing chamber was monitored in the post processing software GT-Post.

Liquid-vapor separator module

The liquid-vapor separator, or water trap, which is located after the stack was modelled by an ejector attached to the recirculation loop as shown in figure 7.5. This ejector removed a fraction of the liquid water condensed after the stack. The mass flow rate of liquid water was measured at the node (1) before the ejector. The liquid water was subsequently purged from the anode loop by an ejector. (6) This ejector was actuated (5) in such a manner that it only removed liquid water. The sensor which recorded the mass flow rate measured in (1), which was multiplied by a gain block (3) allowing for a separation efficiency to be set. In the model a separation efficiency of 95% was assumed. Furthermore, a limiter (4) was placed between the separation efficiency gain block and the ejector to guarantee the ejector was actuated with a positive mass flow rate to prevent failure of the model. One of the convergence criteria determined for the model was for the mass flow rate of liquid water separated by the ejector to reach a steady state value.

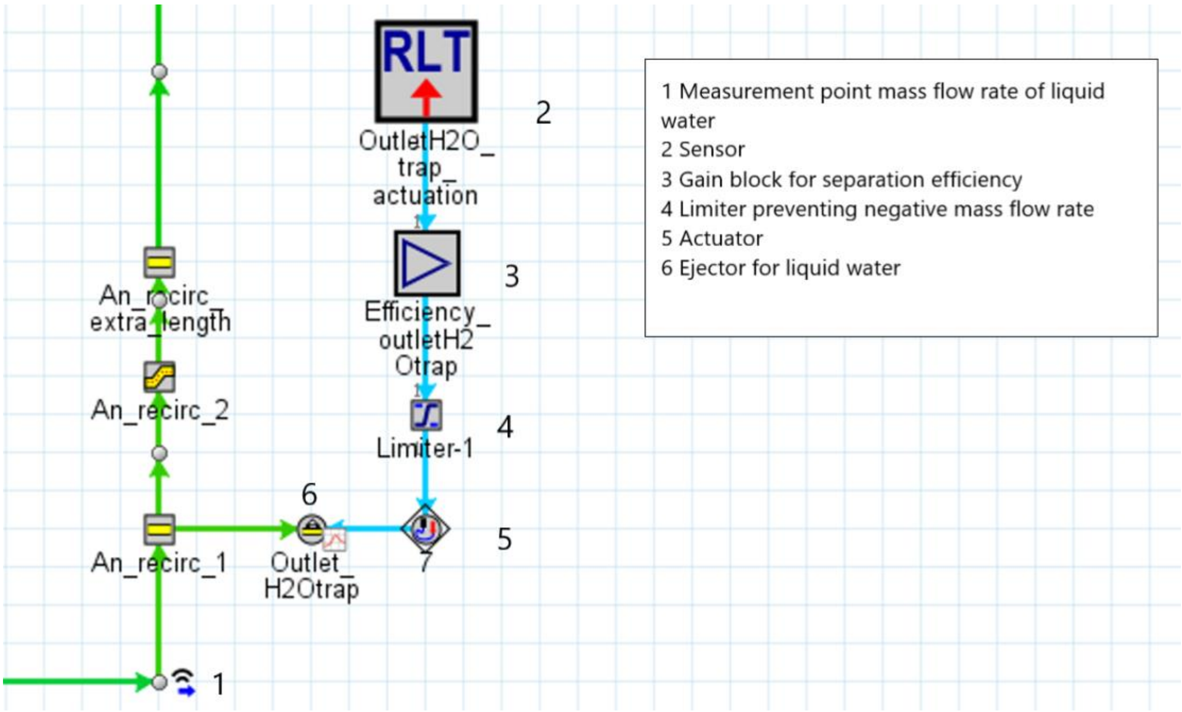

Figure 7.5: Water trap assembly in the recirculation loop

Pump-powered recirculation loop

As in PowerCell's PS-100 system, the recirculation loop in the anode subsystem model was powered by a pump as shown in figure 7.6. The PumpFlow template allowed for the inclusion of an unspecified pump with an isentropic efficiency of 80%. This isentropic efficiency was recommended as an estimate for a well-designed compressor. [49] This approach was taken as it is unsure what compressor will be included in design reiterations of the PS-100. The volumetric flow rate of the recirculation pump was controlled by a PID controller. The species mass flow rate of hydrogen was measured at the node between the inlet of the compressor and the PumpFlow template. The measured value served as the input to the PID controller. The target of the PID controller was the difference between the mass flow rate of hydrogen flowing through the stack at a certain stoichiometry and the consumed hydrogen at a certain current. The error $e(t)$ acted upon in this PID controller was the difference between the targeted mass flow rate of hydrogen and the measured mass flow rate at the inlet of the recirculation pump. The following equation represents the target set in the PID controller.

$$\text{Target} = [\text{Stoichiometry anode -1}] \times [\text{Mass flow rate H}_2 \text{ feed}] \tag{7-1}$$

A PID controller can be used to control a dependent variable in a system, which is referred to as the output. The output of the PID controller is the volumetric flow rate for which the targeted mass flow rate of hydrogen is achieved. The output value determined by the PID controller was used to actuate the PumpFlow template.

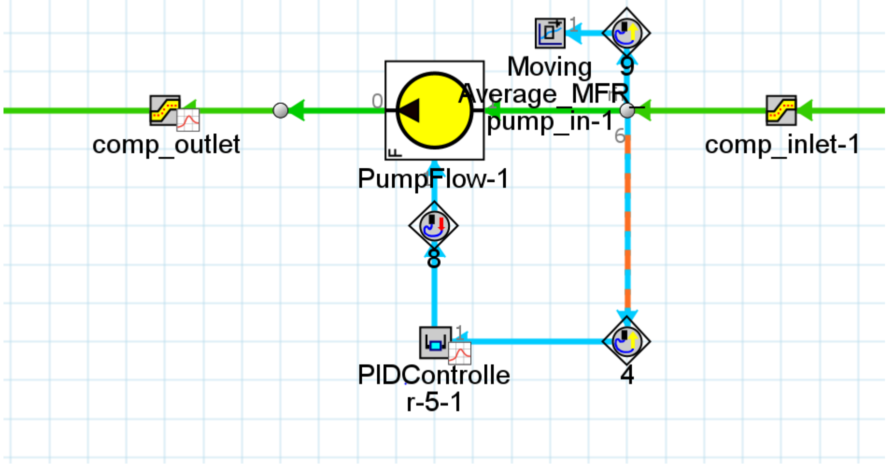

Figure 7.6: Recirculation compressor with PID controller

Suitable gains for the PID controller were determined by trial and error. Eventually, a proportional gain K_p of 10 and an integral gain K_i of 10000 were chosen. The differential gain K_d was set to 0. PID controllers are widely used in process control. In fact, over 95% of controllers applied in process control are of the PID type, only using PI control. [50] The simple structure and maintenance of PID controllers compared to other control systems explains their ubiquity. Increasing K_p leads to a quicker time-response of the controller. When the error $e(t)$ increases, the proportional control value increases. The integral control is meant to bring the steady state of the error $e(t)$ to 0.

Two criteria regarding the PID controller and pump had to be satisfied in order for the model to reach a steady state. First of all, the steady state tolerance on the output of the PID controller was 5%. This criterion had to be valid for two consecutive calculation steps. Furthermore, the moving average of the total mass flow rate into the pump was monitored. A convergence criterion was imposed on this moving average as well. Here the steady state tolerance was only 0.1%. The number of consecutive calculation steps this should hold is calculated by GT-Suite.

Summary of the convergence criteria

The convergence criteria for the model to reach steady state are listed once again in table 7.2.

Table 7.2: Convergence criteria of the anode loop model

Convergence criterion	**Steady state tolerance**
Moving average condensation rate outlet manifold stack	0.1%
Moving average mass flow rate recirculation pump	0.1%
Liquid water ejection rate	0.1%
Condensation rate mixing chamber	1.5%
PID output	5%

The model was run for eight different current levels ranging from 45A to 400A in increments of 50A to cover the full operating range of the PS-100. The maximum run time of every simulated experiment was set to 6 seconds. Whenever the model satisfied all convergence conditions listed in table 7.2, the simulation was cut off instantaneously. In cases where not all convergence conditions were satisfied after the maximum runtime, the simulation was cut off. These simulations were earmarked and not included in the postprocessing of the acquired data.

Design of experiments

For every current level 700 experiments were simulated in which the operating conditions were varied. The operating parameters which were varied are presented in table 7.3. For the design of experiments the Latin hypercube method was used to generate 700 random experiments for every current level. The purpose of simulating these experiments was to single out the operating parameters over the entire operating range of the system which have an influence on the relative humidity of the flow into the stack, the mass flow rates of water in and out of the stack, the condensation rate in the mixing chamber, and the inlet temperature of the stack. The range over which the parameters were varied in the design of experiments is documented in table 7.3.

Table 7.3: Parameters varied in the design of experiments

Parameter	**Unit**	**Minimum**	**maximum**
Anode inlet pressure	bar	1.2	3.5
H_2 feed temperature	ºC	20	80
Dewpoint temperature cathode stack inlet	ºC	20	55
Temperature cathode stack inlet	ºC	20	80
Stoichiometry cathode	-	1.2	2
Stoichiometry anode	-	1.2	2
N_2 fraction in the loop	-	0	0.05
Δp over membrane	bar	0.1	0.5
Temperature of the coolant outlet	ºC	65	80

The parameters listed in table 7.3 have in common that they can all be externally controlled. At the dewpoint temperature the flow has a relative humidity of 100%. The higher the dewpoint, the more moisture is contained in the flow. The N_2-fraction in the loop was included to verify whether the assumption that the anode subsystem purge does not greatly influence the responses is valid as the runtime of the experiments was very brief in case they reached a steady state. The N_2-fraction was included as an initial condition and did not change over the runtime of the simulations. The pressure difference set the cathode inlet pressure in an indirect way as it was subtracted from the anode inlet pressure. The cathode was operated at a slightly lower pressure as this reflects real operating conditions. This is done in order to prevent too much nitrogen from crossing over to the anode subsystem. The pressure difference between the anode and the cathode is limited by the mechanical stability of the membranes.

Metamodels and optimization

After running the 5600 experiments, the converged simulations were used to construct metamodels for the following responses: the relative humidity at the anode inlet of the stack, the temperature at the anode inlet of the stack, the mass flow rates of liquid water into and out of the stack, the mass flow rates of water vapor into and out of the stack, and finally the condensation rate in the mixing chamber. The constructed metamodels were of the Kriging and the multilayer perceptron (MLP) type. Krigings were briefly explained before when the water crossover rate function was described. MLPs are artificial neural networks with an input layer, an output layer, and at least one hidden layer. [53] The input layer handles the input parameters as specified in table 7.3. The hidden layers enable the MLP to learn patterns in the input data. MLPs are feedforward meaning the input information passes through in one direction to the output layer. The output layer gives a prediction for the response the MLP was created for based on the input parameters.

The simulated experiments were divided into training, validation, and test datapoints. The training datapoints were used to construct the metamodels with. The validation and test sets served to test how well the constructed metamodels perform on unseen datapoints and to refine the model, respectively. Of all converged experiments, 75% were assigned as training datapoints and 15% were assigned as test and validation datapoints each as recommended by Gamma Technologies. When a metamodel was built to predict the anode inlet temperature based on the parameters listed in table 7.3, 15 % of the simulated experiments were used to compare and validate the predicted temperature by the metamodel with the temperature determined in the simulation. GT-post slightly altered the hyperparameters of the Kriging or MLP and compared the performance of the tweaked metamodel by inserting the next validation point. The hyperparameters of a metamodel are characteristics that define its functioning. They are set before the training process of the metamodel is initiated. Hyperparameters determine how well and quickly a metamodel fits to the input data. [54] A hyperparameter of a MLP is for instance its number of hidden layers. The model that was best based on the set of validation datapoints was then used to insert the test datapoints for an unbiased evaluation of the model fit. The comprehensive procedure of training, validating, and testing the metamodels is schematically shown in figure 7.7. The schematic overview of the creation of metamodels was made based on internal communication with Gamma Technologies.

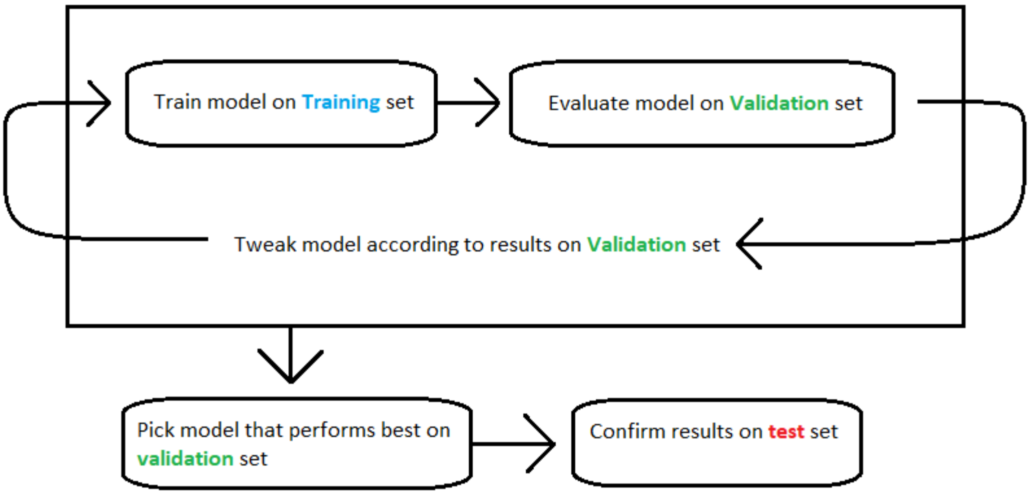

Figure 7.7: Training, validating and testing a metamodel

After the construction, the quality of the metamodels was assessed in the postprocessing software provided by Gamma Technologies. Good indicators for the quality of a metamodel are the root means square (RMS) errors and the coefficients of determination (R^2) of the training, test, and validation sets. When the MLP and Kriging metamodels were compared, the one with the lowest RMS error on the validation set was superior. The RMS error for the test set was required to be not significantly higher, meaning within one order of magnitude. The root mean square error was defined as: [55]

$$\mathrm{RMSE} = \sqrt{\frac{\sum_{n=1}^{N}(\hat{y}_n - y_n)^2}{N}} \tag{7-1}$$

In equation (7-1), N is the number of simulations, $\hat{y}_n$ is the simulated response, and $\hat{y}_n$ is the predicted response by the metamodel.

The coefficient of determination indicates the proportion in the variance of the predicted response which can be attributed to the fit of the model to the input data. The coefficient of determination can be between 0 and 1. The closer to 1 this coefficient is, the better the fit of the metamodel to the data generated with the simulations. An acceptable value for the coefficient of determination depends on the context, but in the natural sciences it should be close to 1. [56] In this thesis a value between 0.85 and 1 was considered acceptable.

The postprocessing software provided by Gamma Technologies came with an optimizer tool which allowed for multi-objective pareto optimization. In this tool, multiple metamodels could either be minimized, maximized, or targeted at a certain value. In the multi-objective pareto optimization the objectives set for the metamodels in the tool were fulfilled in such a manner that the best compromise between the objectives was found. Each included metamodel was made to fulfill its objective set in the tool to the extent that no better outcome could be achieved without obstructing the other metamodels in attaining their objectives. The optimizer tool was used to recommend system operating parameters at two operating currents facilitating proper anode water management. In the optimizer tool the MLP for the mass flow rate of liquid water at the anode inlet of the stack was minimized and the condensation rate in the mixing chamber was targeted at 0 g/s at 100 A. Furthermore, at 300 A, a target value for the relative humidity at the anode inlet of the stack was set at 60% whereas the condensation rate in the mixing chamber was targeted at 0 g/s. For both operating points, a number of combinations of system operating parameters were found to reach the pareto optimum.

III

Results:

Modelling the PowerCell stack and anode subsystem

8 Results GT-Suite PEM fuel cell stack model

In this chapter, the results of GT-Suite's PEM fuel cell stack model fitted on the recorded voltages of the T0042 dataset are presented. The data in T0042 was gathered on a 20-cell stack with the same MEAs as those in PowerCell's stack. As noted in chapter 6, the PEM fuel cell model with its water crossover models was unable to capture the water crossover rates measured in the test station by both Bosch and PowerCell.

Predicted voltage by GT-Suite's PEM fuel cell stack model

As the PEM fuel cell stack model was fitted targeting the recorded voltage in 25 random measurement points of the T0042 dataset, the model's performance in predicting the voltage will be evaluated first. The values for the tortuosity, catalyst specific surface area, and Springer's b11 coefficient were: 1.2397866, 698.9053, and 0.004505361 respectively. After fitting the PEM fuel cell stack model using the optimizer tool, it was run in a test station model in GT-Suite. In this model the stack was isolated from the rest of the system, including only the hydrogen and air supply, and electrical connection. The simulation of the fitted PEM fuel cell stack model in GT-Suite resulted in predictions of voltages for the 25 operating points stored in the case set-up based on their recorded operating parameters in the T0042 dataset. The predicted voltages by the PEM fuel cell stack model with respect to the corresponding measured voltages in T0042 are portrayed in figure 8.1.

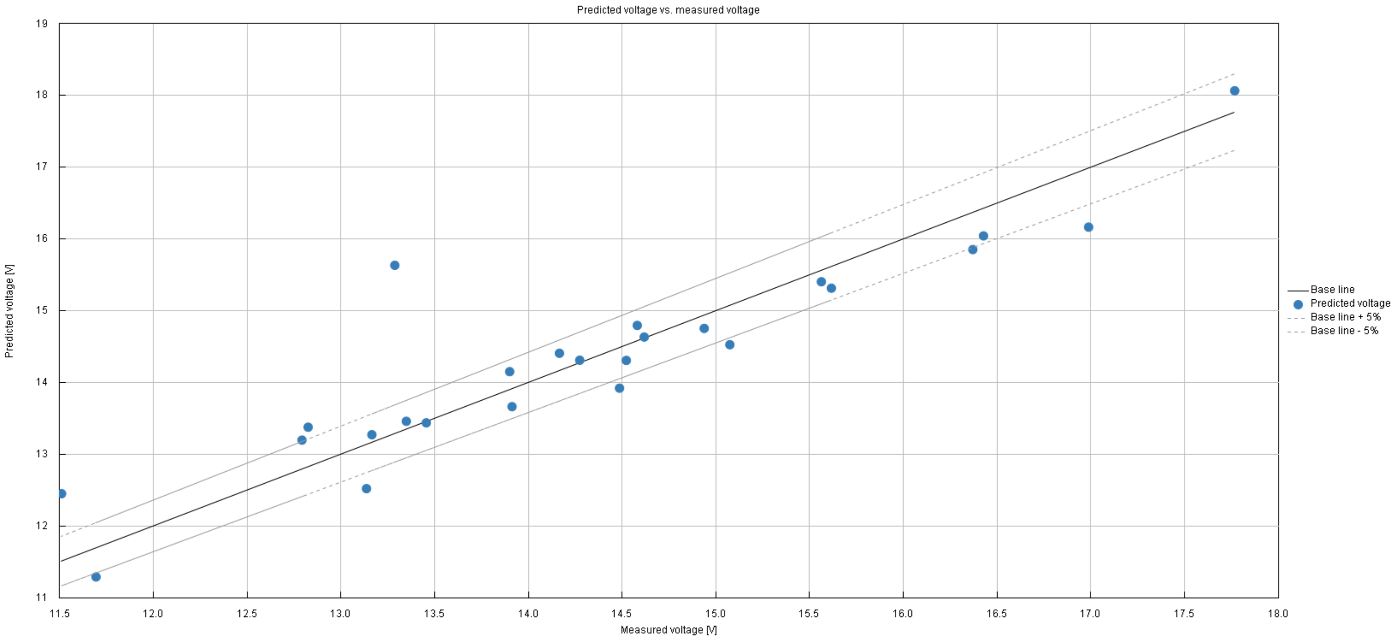

Figure 8.1: Predicted voltage vs. measured voltage in Bosch's 20-cell stack

In figure 8.1, the black uninterrupted line indicates a perfect match between a predicted voltage by the PEM fuel cell stack model and the corresponding measured voltage. The voltages predicted by the PEM fuel cell stack model are listed on the y-axis. The T0042 measured voltage is on the x-axis. The closer the blue dots are located to the black line, the better the prediction. Two dotted black lines indicate when the predictions are within a range of ± 5% of the measured voltages. The PEM fuel stack model was able to capture the voltage in the majority of cases within this range. The values of the predicted voltages are recorded in Appendix 1.

Predicted water crossover rate by GT-Suite's PEM fuel cell stack model

Simultaneously, the water crossover rate from the cathode to the anode predicted by the PEM fuel cell model was monitored. The water crossover rates predicted by the PEM fuel cell stack model with five different diffusion models (Springer, Vetter, Kulikovsky, Nguyen, and Motupally) are shown in comparison to the corresponding measured voltages in T0042 in figure 8.2.

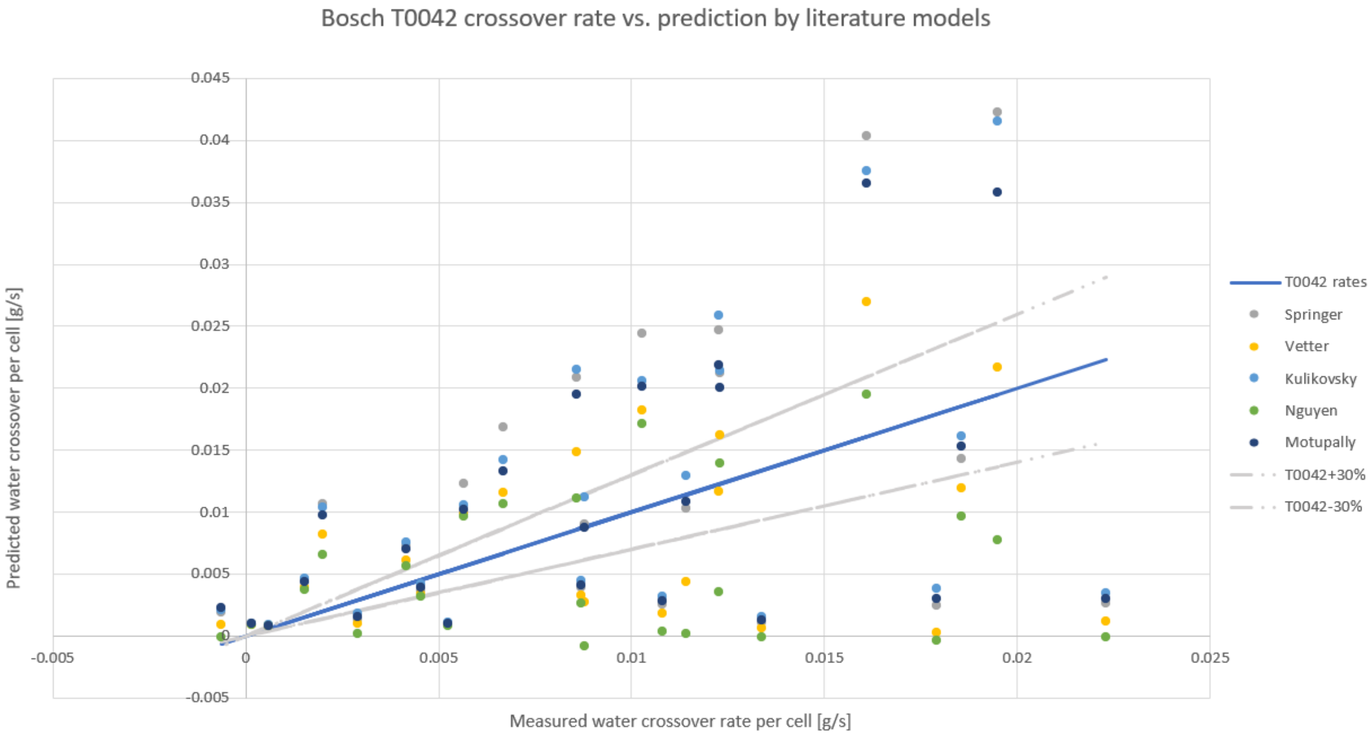

Figure 8.2: Predicted water crossover rate vs. measured rate in Bosch's 20-cell stack

This plot in figure 8.2 follows the same principle as the plot in figure 8.1. The closer the simulated crossover rates are to the uninterrupted blue line, the better the approximation. As the measurement error on the water crossover rates recorded in T0042 was unknown, two lines indicating a deviation of 30% from the measured crossover rates were included in figure 8.2. This margin was chosen as the greatest deviation for identical crossover measurements in Bosch's and PowerCell's test station was 30%. It should be noted in figure 8.2 that the predicted water crossover rates by the PEM fuel cell stack model showed a great deviation from the measured voltages in the test station by Bosch for the 25 experiments. Moreover, the predicted water crossover rates were significantly influenced by the diffusivity model. As predicted in chapter 5, Nguyen's model predicted the lowest crossover rates as it is a conservative diffusion model. The predicted crossover rates by the PEM fuel cell model were not accurate at all with deviations up to 400%. In only a minority of predictions, the water crossover rate was within the 30% deviation zone.

Next, the eleven experiments conducted in PowerCell's test station were inserted in the case set-up of the GT-Suite test station model. The PEM fuel cell stack model which was used was the model which was fitted on the T0042 datapoints. The predicted water crossover rates for these experiments with the five different diffusion models are compared to the corresponding measured voltages in figure 8.3. The literature models predicted crossover rates which were off by an order of magnitude compared to the measured water crossover rate in PowerCell's 71-cell stack.

Moreover, the water crossover occurred from the anode to the cathode in many cases. It is likely irregularities occurred in inserting the case set-up of the model.

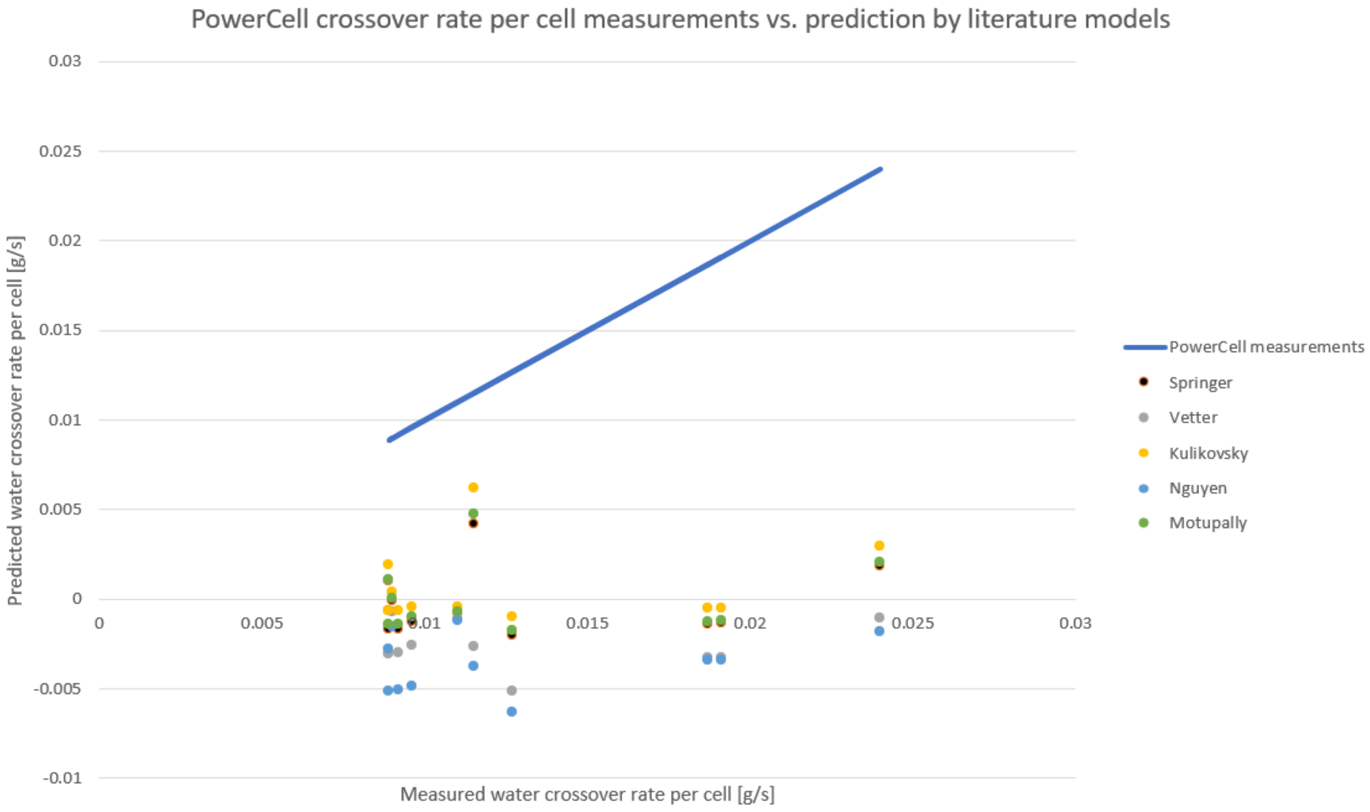

Figure 8.3: Predicted water crossover rate vs. measured rate in Powercell's 71-cell stack

Upon examination of the predicted water crossover rates, it appeared that the literature models which were discussed in chapter 5 and integrated in the PEM fuel cell model did not accurately reflect the measured water crossover rates observed in Bosch's measurements on the 20-cell stack. The PEM fuel cell model integrated in GT-Suite was abandoned as predicting the water crossover rate within reasonable bounds was of vital importance for further proceedings. The coupling between the system operating parameters specified in table 7.3 and processes occurring within the stack was lost as a consequence. Additionally, the discretized nature of the PEM fuel cell stack model allowed for monitoring of processes occurring within the stack in great detail. Abandoning the PEM fuel cell model implied that the anode water management could only be monitored from a system viewpoint by setting requirements on the boundary conditions of the stack based on the literature research.

9 Results anode subsystem modelling

In this chapter the results are presented which were acquired through evaluation of the anode subsystem model described in chapter 7. First of all, the water crossover function which was constructed based on the T0042 dataset provided by Bosch will be evaluated. The influence of the input parameters on the output value of the function, and its capacity to predict the water crossover rate are discussed. Additionally, the influence of the parameters listed in table 7.3 on the responses mentioned in the previous chapter will be evaluated. The quality of the metamodels will be assessed and finally two cases will be treated where the optimizer tool integrated in GT-Suite was used to find suitable operating parameters considering multiple objectives regarding the anode water management.

Membrane crossover Kriging

The first step in modelling the anode subsystem was to replace the PEM fuel cell stack model mentioned in chapter 6 with stand-alone templates that could approach the processes occurring in the stack. As mentioned in chapter 8, the water crossover phenomena were modelled with a lumped function fitted on water crossover rates recorded in the T0042 dataset.

The factors listed in table 7.1 were the input parameters for the function predicting the water crossover rate from the cathode to the anode. Figure 9.1 displays the main effects magnitude plots (MEMP) for the water crossover rate function. In this plot the linear effect of the factors denoted in table 7.1 on the predicted water crossover rate are portrayed. E.G., if the value of the water crossover rate is equal to -0.4 g/s for the anode inlet temperature, this is the difference in the water crossover rate for the lowest temperature and the highest temperature recorded in T0042. This indicates that a higher anode inlet temperature led to a lower water crossover rate from the cathode to the anode. This could possibly be a consequence of thermos-osmosis.

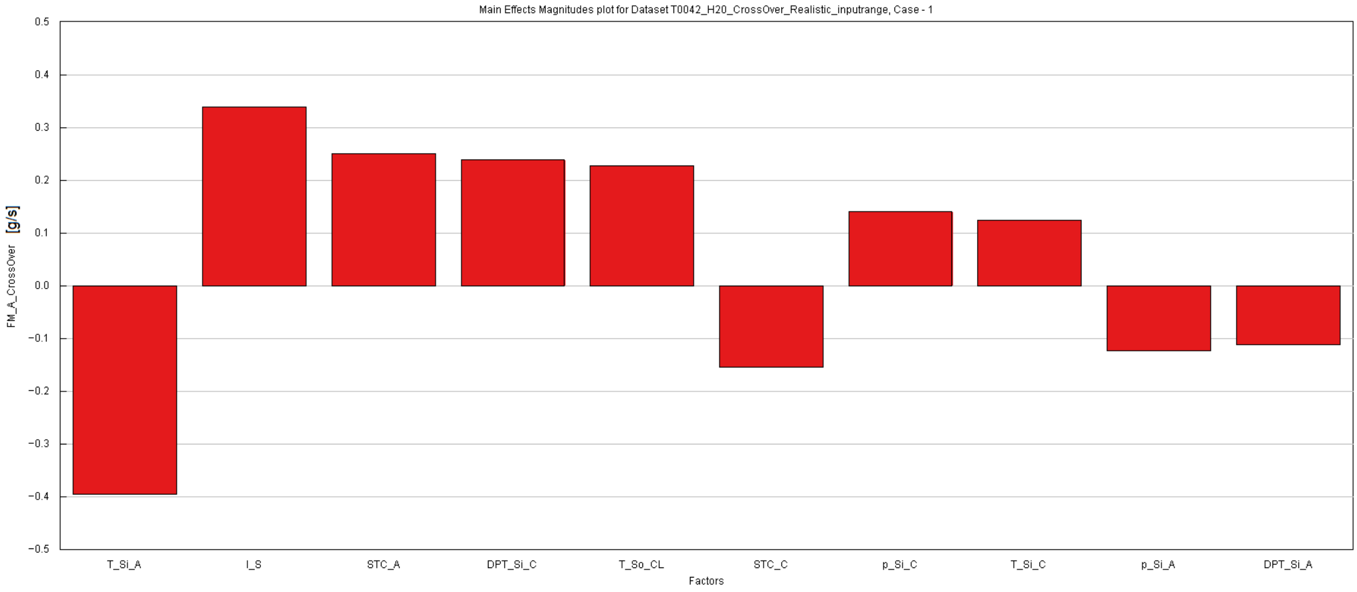

Figure 9.1: Linear influence of the factors on the magnitude of the water crossover

As shown in figure 9.1, a higher operating current gave rise to a greater water crossover rate. This effect was expected as the water production in the stack increases with the operating current. The anode stoichiometry was positively related to the water crossover rate as well. When the stack is operated at a higher anode stoichiometry, the gas flow channels on the anode side are drained of water. This leads to a lower water concentration on the interface of the membrane and the anode catalyst layer which stimulates back-diffusion from the cathode to the anode. Furthermore, a higher cathode dewpoint temperature increased the water crossover rate to the anode as well due to a higher water concentration on the cathode side of the membrane. A higher coolant outlet temperature led to an increased water crossover as well. This temperature was assumed to approximate the average stack temperature. A higher temperature facilitates diffusive water transport in membranes, which explains a greater flux of water from the cathode to the anode. The cathode stoichiometry showed a negative relation to the water crossover rate from the cathode to the anode. The same reasoning can be followed here as for the anode stoichiometry. A higher cathode stoichiometry lowers the water concentration on the interface of the membrane and the cathode catalyst layer which lowers the diffusive flux of water to the anode. It appears the anode and cathode inlet pressures did have some influence on the water crossover rate from the cathode to the anode, albeit relatively small compared to the other parameters. The positive relation between the cathode pressure and negative relation of the anode inlet pressure gives rise to the suspicion that hydraulic permeation might have played a role in the water transport through the membranes. The hydraulic permeation mechanism might play a bigger role in thin reinforced membranes than in the thicker membranes the water transport models treated in chapter 5 were created on. The temperature of the cathode inlet flow had a positive influence on the water crossover rate to the anode. The anode inlet temperature had a negative influence on the water crossover rate to the anode. This might be due to water crossing from the hot to the cold side of the membrane as a result of thermos-osmosis. The anode inlet temperature could have a greater influence on the water crossover rate as there is less heat production in the anode catalyst layer than in the cathode catalyst layer, meaning the temperature of the inlet flow influences the temperature at the interface between the membrane and the catalyst layer to a greater degree. Finally, the dewpoint temperature of the anode inlet flow was negatively related to the water crossover rate. This is not surprising as the driving force for crossover to the anode is lower if the water concentration is higher at the interface of the anode catalyst layer and the membrane.

In figure 9.2, the performance of Kriging made for the water crossover rate based on the T0042 dataset is shown. The error is the relative difference in the water crossover rate predicted by the Kriging based on the training data and the corresponding crossover rate recorded in T0042. The relative error was within 5% in the vast majority of cases and always within 15%. It should be noted however that no measurement error on the crossover rate was provided for the T0042 dataset. The values determined by PowerCell and Bosch differed 30% at 300A and 14.3% at 440 A in identical experiments as shown in table 6.1. It should be kept in mind that an error on the mathematical model smaller than the possible measurement error is not meaningful.

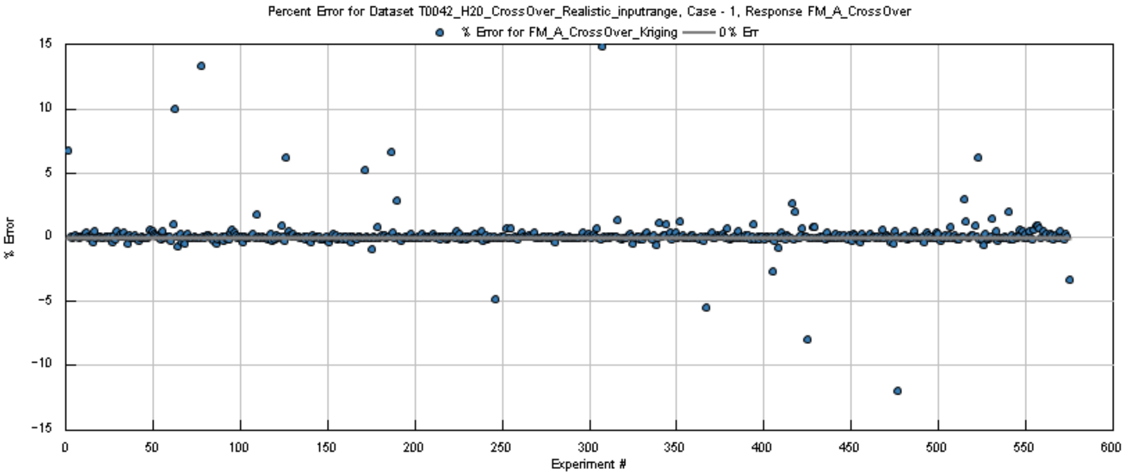

Figure 9.2: Percent error of the predicted values by the Kriging vs. simulated value

Simulation run of the anode subsystem model

Running the anode subsystem model with the design of experiments as specified in table 7.3 resulted in a large set of simulated experiments. For all eight current levels from 45 A to 400 A, 700 experiments were simulated. Not all simulations reached a steady state in accordance with the criteria listed in table 7.2 within the maximum runtime of 6 seconds. In table 9.1 the number of simulated experiments which converged are listed for every current level.

Table 9.1: Number of converged simulations per current level

Current level [A]	**Number of converged simulations [-]**
45	553
100	682
150	637
200	603
250	601
300	573
350	568
400	525

Based on the simulated experiments in table 9.1, metamodels were built for various responses. The responses included the relative humidity at the anode inlet of the stack, the temperature at the anode inlet of the stack, the condensation rate in the mixing chamber, the liquid water mass flow rates into and out of the anode side of the stack, and the water vapor mass flow rates into and out of the anode side of the stack. The influence of the parameters of the design of experiments listed in table 7.3 on the responses as determined in the simulations will now first be evaluated through MEMPs.

MEMP for the relative humidity at the anode inlet of the stack

The relative humidity at the anode inlet of the stack is the first response to be evaluated. The linear influence of all parameters listed in table 7.3 on the relative humidity is portrayed in the MEMP in figure 43. As 700 experiments were simulated over eight current levels from 45A to 400A, the influence of the factors on the response was captured over the whole operating range of the system.

From the MEMP in figure 9.3 two factors clearly stand out in their effect on the relative humidity at the anode inlet of the stack. First of all, the hydrogen feed temperature was strongly negatively related to the inlet relative humidity. This can be explained by the fact that a higher hydrogen feed temperature leads to a smaller temperature drop when recirculated and fresh hydrogen mix. The flow which has passed through the mixing chamber will thus reach the stack at a higher temperature. This in turn means that the saturation pressure at the inlet of the stack will be higher and the relative humidity lower. A higher anode stoichiometry resulted in a lower relative humidity as well. This can be explained by the fact that the flow leaving the stack is at a relatively high temperature. The greater the portion of recirculated hydrogen in the mixing chamber, the higher the temperature of the flow leaving the chamber will be. This flow subsequently reaches the anode inlet of the stack at a lower relative humidity. Furthermore, a higher anode stoichiometry dilutes the flow by adding more hydrogen. This also lowers the relative humidity at the inlet of the stack.

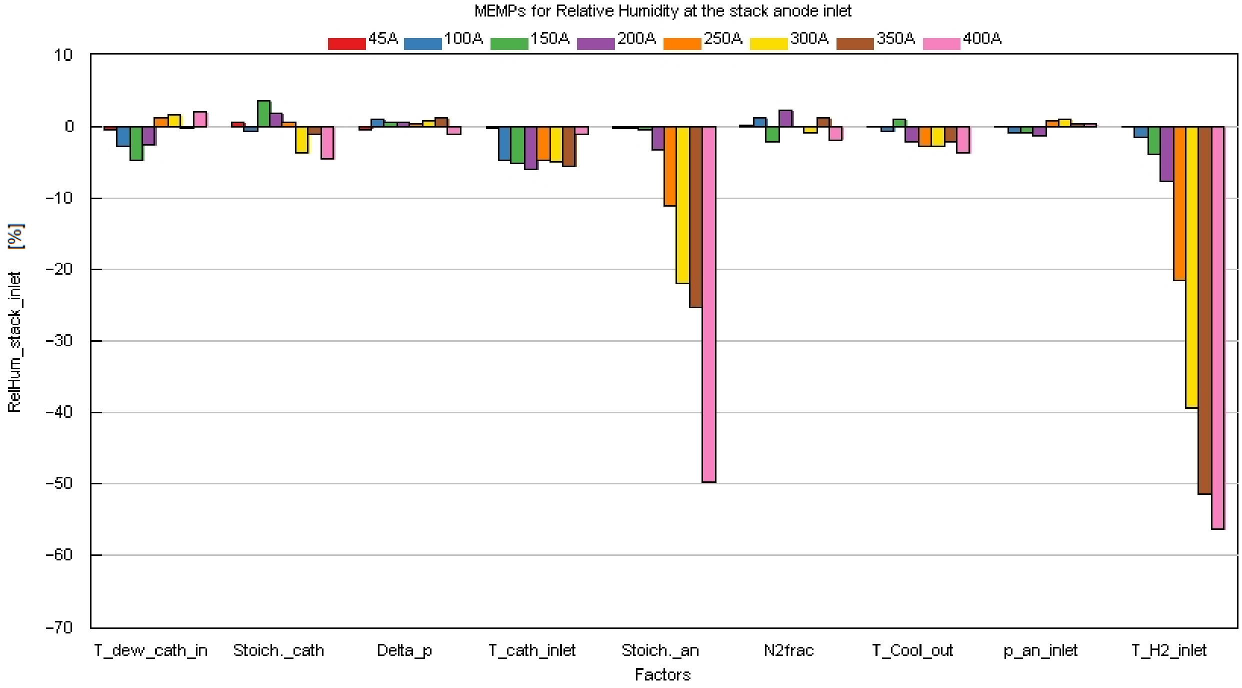

Figure 9.3: Linear influence of DoE factors on the stack inlet relative humidity

The cathode inlet temperature of the flow had a negative effect on the relative humidity at the anode inlet. This can be explained by the cathode flow being in thermal contact with the anode flow through the MEA. When the cathode flow enters the stack at a higher temperature it heats up the anode flow through conduction and convection. When the hydrogen leaves the stack at higher temperature the temperature at the inlet of the stack will rise and the relative humidity will decrease.

MEMP for the temperature at the anode inlet of the stack

As shown in figure 9.4, the parameters with the greatest influence on the temperature at the anode inlet of the stack were the anode stoichiometry, the coolant outlet temperature, and the hydrogen feed temperature. None of these parameters are surprising. As explained earlier in the section on the relative humidity MEMP, a higher anode stoichiometry increases the portion of hot recirculated hydrogen in the mixing chamber. This raises the temperature of the flow arriving at the anode inlet of the stack. At currents of 300 A and above this effect becomes less pronounced. One could speculate that at such high operating currents the recirculated hydrogen will be of such a high temperature that this alone will be enough to raise the temperature at the anode inlet. Therefore, additionally raising the anode stoichiometry would be of less influence than at lower operating currents around 200 A.

The same holds when the temperature of the hydrogen fed to the system is raised instead. When the coolant outlet temperature is higher, the recirculated hydrogen is of a higher temperature as well. This in turn gives rise to a higher temperature at the anode inlet. A parameter which had a surprising effect on the anode inlet temperature was the cathode inlet temperature. In the simulated experiments raising the cathode inlet temperature led to a decrease in the anode inlet temperature. This appears to be in contradiction with the effect of the cathode inlet temperature on the anode inlet relative humidity seen in the MEMP in figure 9.3. The effect became increasingly stronger at higher operating currents.

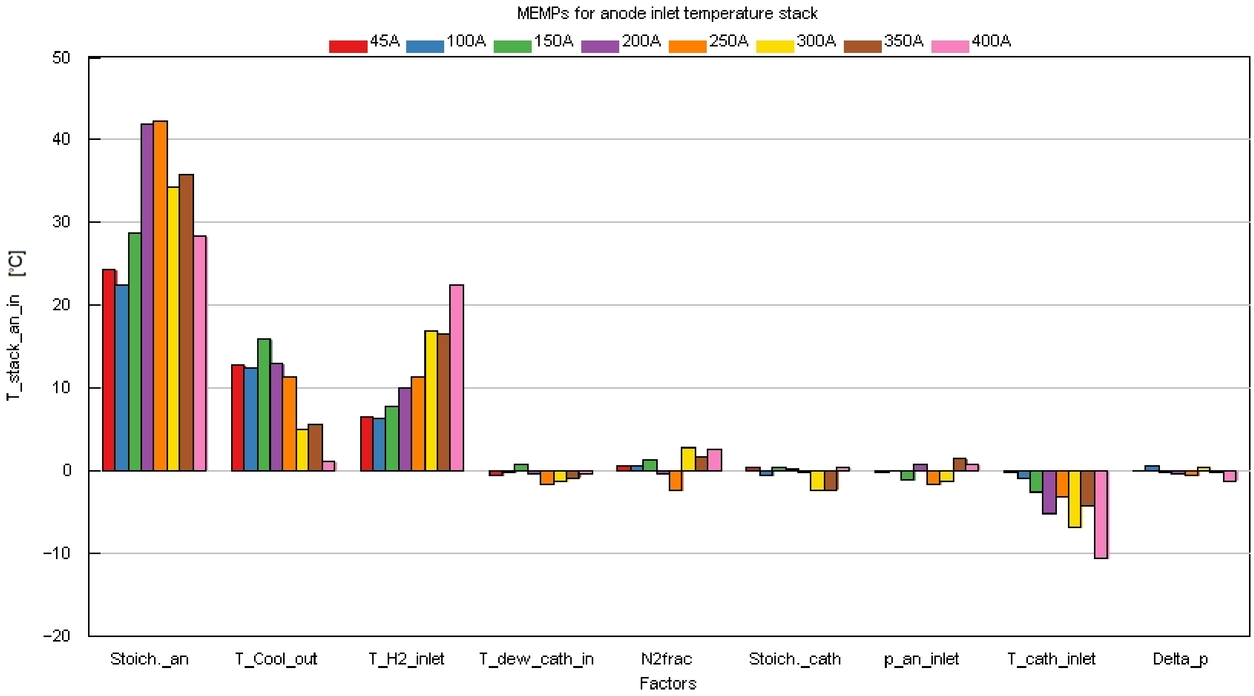

Figure 9.4: Linear influence of DoE factors on the stack inlet temperature

MEMP for the mass flow rate of liquid water into the stack anode inlet

The mass flow rate of liquid water into the anode inlet of the stack was most strongly affected by the cathode inlet temperature, the hydrogen feed temperature, and the anode stoichiometry in the simulated experiments as shown in figure 9.5. The cathode inlet temperature was negatively related to the mass flow rate of liquid water at the anode inlet of the stack, which is in agreement with the MEMP for the relative humidity shown in figure 9.3.

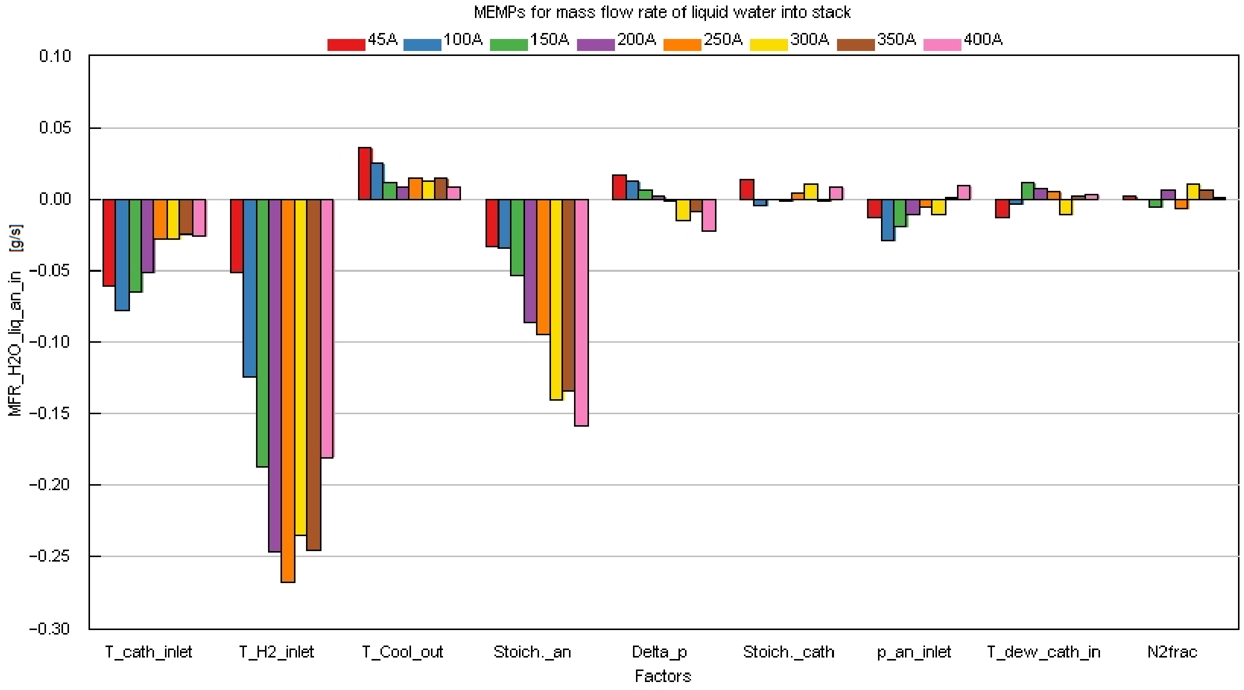

Figure 9.5: Linear influence of DoE factors on the inlet mass flow rate of liquid water

MEMP for the mass flow rate of water vapor into the stack anode inlet

The mass flow rate of water vapor at the anode inlet was strongly affected by the anode stoichiometry. (Figure 9.6) This was unsurprising as the stoichiometry directly influences the recirculation mass flow rate. When a greater mass flow rate is recirculated, naturally more water vapor will appear at the anode inlet of the stack. The coolant outlet of the stack was positively related to the water vapor mass flow rate at the anode stack inlet. A higher coolant outlet temperature implies that the recirculated flow leaves the stack at a higher temperature. This in turn leads to a higher temperature after the mixing chamber, raising the saturation pressure which means more water can remain in the vapor phase. This effect was the strongest at the midrange operating currents. At low currents there is simply less water in the anode subsystem. The hydrogen feed temperature had a similar effect on the mass flow rate of water vapor at the inlet of the stack over the current range. The cathode inlet temperature was increasingly negatively related to the mass flow rate of water vapor at the stack inlet.

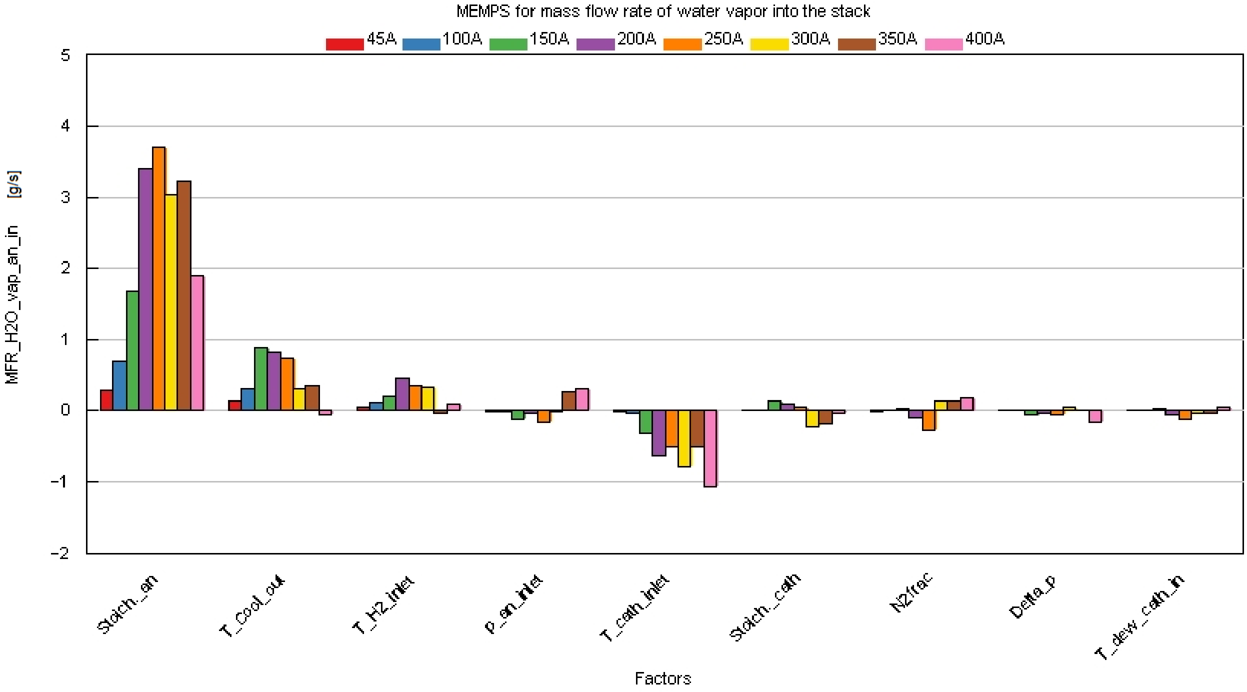

Figure 9.6: Linear influence of DoE factors on the inlet mass flow rate of water vapor

MEMP for the condensation rate in the mixing chamber

Condensation in the mixing chamber occurs when dry hydrogen meets with recirculated hydrogen carrying away water from the stack. The feed temperature of dry hydrogen was negatively related to the condensation rate in the mixing chamber as shown in figure 9.7. Condensation occurred at a greater rate when the recirculated flow experienced a greater temperature drop. When the dry hydrogen is fed at a low temperature, the temperature of the hot recirculated flow and the saturation pressure will decrease leading to condensation. The anode stoichiometry was positively related to the condensation rate in the mixing chamber with the greatest effect seen in the midrange current levels. The coolant outlet temperature showed the same pattern, but the effect was less pronounced. The cathode inlet temperature was negatively related to the condensation rate in the mixing chamber.

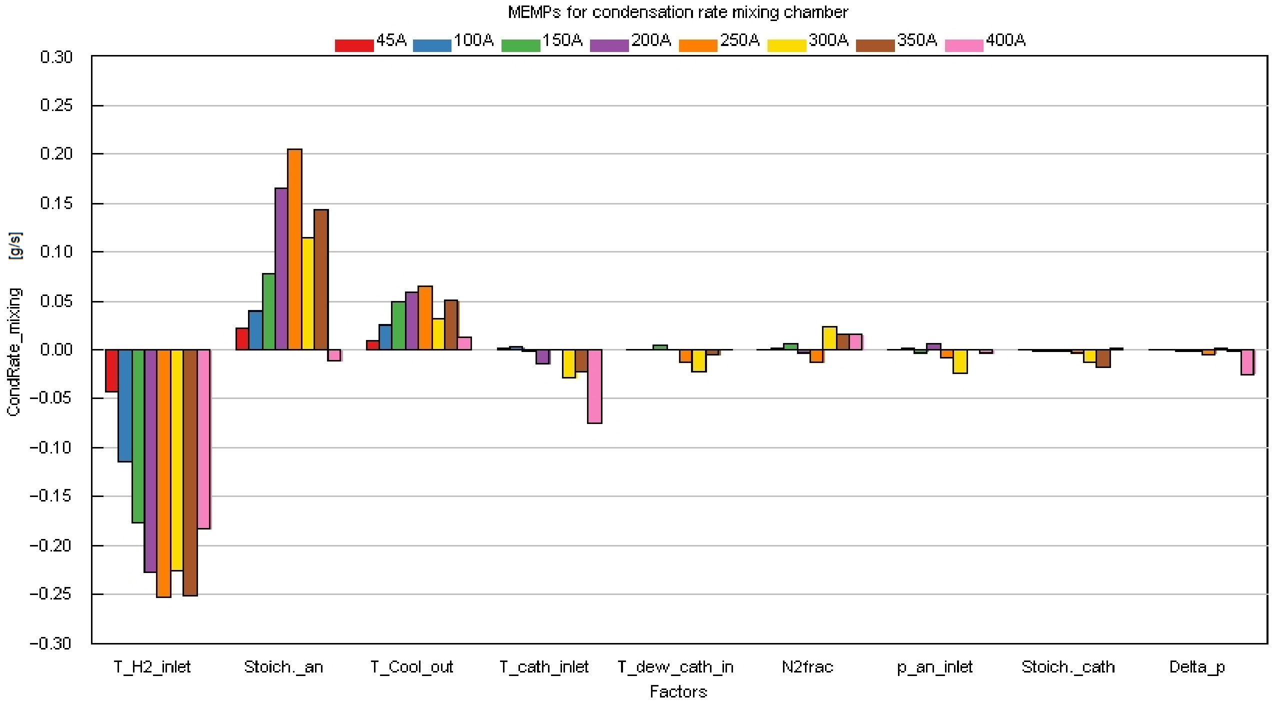

Figure 9.7: Linear influence of DoE factors on the condensation rate in the mixing chamber

MEMP for mass flow rate of water vapor out of the stack anode outlet

The factors which had the strongest linear influence on the mass flow rate of water vapor at the outlet of the stack were the anode stoichiometry, the coolant outlet temperature, and the cathode inlet temperature as portrayed in the MEMP in figure 9.8. The anode stoichiometry being positively related to the mass flow rate of water vapor at the anode outlet was unsurprising as the stoichiometry is directly related to the recirculation mass flow rate. Furthermore, a higher stoichiometry lowers the water concentration at the interface of the membrane and anode catalyst layer stimulation water crossover to the anode. This in turn increases the mass flow rate of water at the anode outlet of the stack. The coolant outlet temperature had a positive influence on the mass flow rate of water vapor at the anode outlet of the stack. Up till 250A, the effect increased. This is due to enhanced diffusion in the membrane at higher temperatures. At higher currents the water concentration gradient becomes greater due to the water production in the cathode catalyst layer. Here the anode stoichiometry and coolant outlet temperature had less added value in increasing the water crossover rate. Therefore, they also had a smaller influence on the water vapor mass flow rate at the anode outlet.

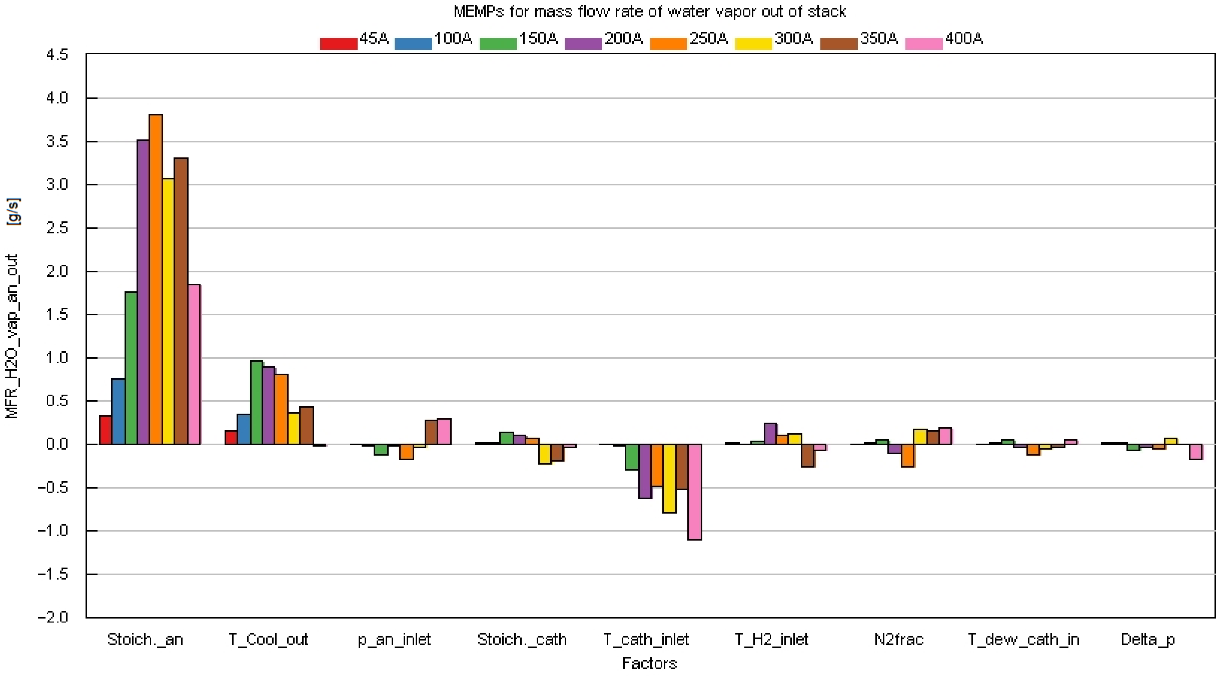

Figure 9.8: Linear influence of DoE factors on the outlet mass flow rate of water vapor

The negative relation between the cathode inlet temperature and the mass flow rate of water vapor at the anode outlet of the stack, raises the suspicion that thermos-osmosis in the membrane might play a role in suppressing the water crossover from the hot side of the membrane to the cold side as found by Kim, [46] especially at higher operating currents.

MEMP for the mass flow rate of liquid water out of the stack anode outlet

Once again, the factors which had the strongest linear influence on the mass flow rate of liquid water at the outlet of the stack were the anode stoichiometry, the coolant outlet temperature, and the cathode inlet temperature. The MEMP for the mass flow rate of liquid water at the outlet of the stack is shown in figure 9.9. The same reasoning can be followed here as for the mass flow rate of water vapor at the anode outlet of the stack.

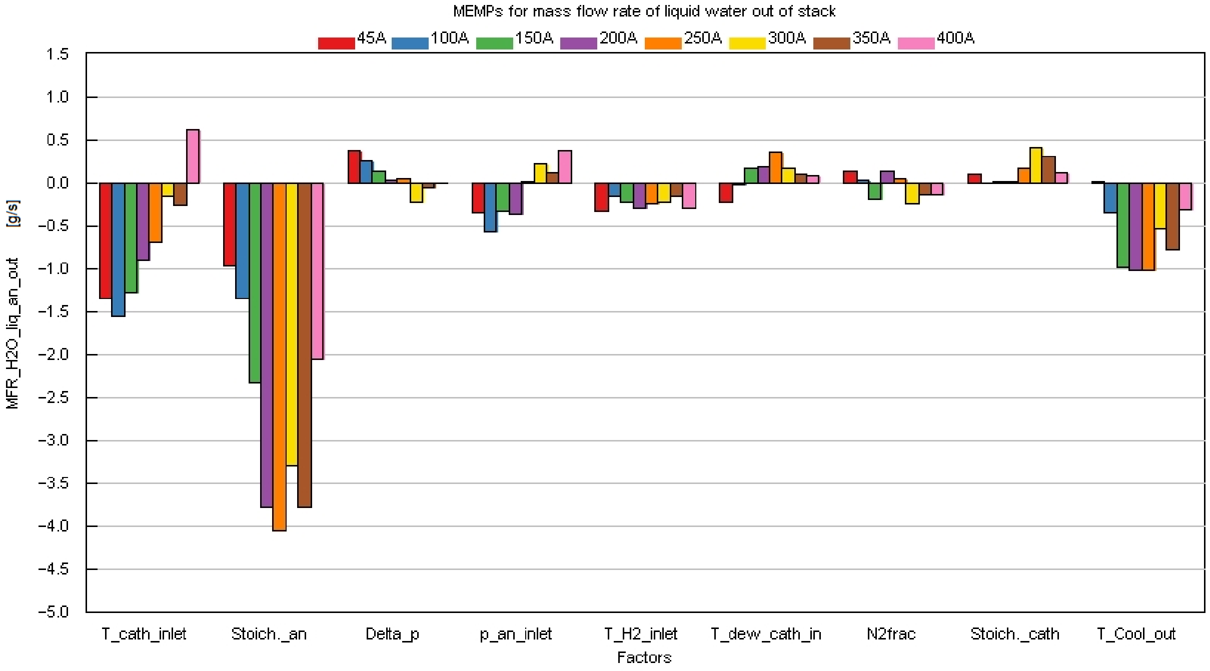

Figure 9.9: Linear influence of DoE factors on the outlet mass flow rate of liquid water

Creation and quality of metamodels

Based on the experiments listed in table 9.1, MLP and Kriging metamodels were created for several responses. The responses included: the relative humidity at the anode inlet of the stack, the temperature at the anode inlet of the stack, the mass flow rate of water vapor into and out of the stack, the mass flow rate of liquid water into and out of the stack, and the condensation rate in the mixing chamber where recirculated hydrogen mixes with the newly introduced hydrogen.

For the sake of clarity, the metamodels will only be evaluated at two current levels in this work. First, the operating point of 100 A will be considered and secondly the operating point of 200 A and finally the operating point of 400 A. The metamodels for the other current levels were evaluated but not included in this chapter. Some brief remarks on those metamodels will be included in the discussion.

Kriging and MLP metamodels for responses at 100 A

Now the quality of the metamodels made for the responses at a current level of 100 A will be evaluated. A comprehensive overview of the quality metrics for the metamodels is included in Appendix 3. For the operating current of 100 A, both the Kriging and MLP metamodel captured the generated data for the condensation rate in the mixing chamber well. For both metamodels the R-squared values for the training, validation, and test sets were above 0.9. The MLP outperformed the Kriging slightly, however. Unfortunately, both the MLP and the Kriging performed poorly for the relative humidity at the anode inlet of the stack. The MLP performed much better in the validation set than the Kriging. In the test phase both metamodels had a very low R-squared value with absolute errors for the predicted relative humidity as high as 97 percent point. The metamodels for the anode inlet temperature of the stack were both of good quality. The MLP outperformed the Kriging once again. For the mass flow rate of water vapor into the anode inlet the MLP outperformed the Kriging in validation and testing. The R-squared value was smaller for the training set, however. This was true for virtually all metamodels. The metamodels for the mass flow rate of liquid water into the anode inlet of the stack had somewhat lower R-squared values than their counterparts for water vapor. The R-squared values of the MLP were still 0.75 for the validation set and 0.87 for the test set. The metamodels for the mass flow rate of water vapor at the anode outlet of the stack were of high quality. For the MLP all R-squared values were above 0.9. The same was true for the MLP for the mass flow rate of liquid water at the anode outlet. All R-squared values were above 0.87 in this case.

It should be noted that for every response at 100 A, metamodels of the MLP type outperformed those of the Kriging type. Although, the training R-squared value was close to 1 for the Krigings, they lacked in the validation and testing process. Typically, Krigings perform very well on the training set, however. A likely cause for the poor fit of the metamodels is the skewed dataset. As it turns out, in the simulated experiments the relative humidity at the anode inlet of the stack was 100% in most cases. Only for some outliers of the 637 datapoints, the relative humidity was not equal to 100% as displayed in figure 9.10. Obviously, there is little point in creating metamodels for a response which always has the same value except for outliers. The metamodels created for the anode inlet relative humidity at 100 A did not reflect the values predicted in the simulated experiments as shown in figure 9.10, however. The metamodels often predicted lower relative humidities than 100%. In the simulated experiments assigned to the validation set were depicted using green points and in the simulated experiments assigned to the testing set using red points. Judging from the simulated experiments, operating the stack at an inlet relative humidity of 60% was not attainable at 100 A. Therefore, at this current level it was of greater relevance to minimize the mass flow rate of liquid water into the stack at the anode inlet and the condensation rate in the mixing chamber to minimize the risk of flooding.

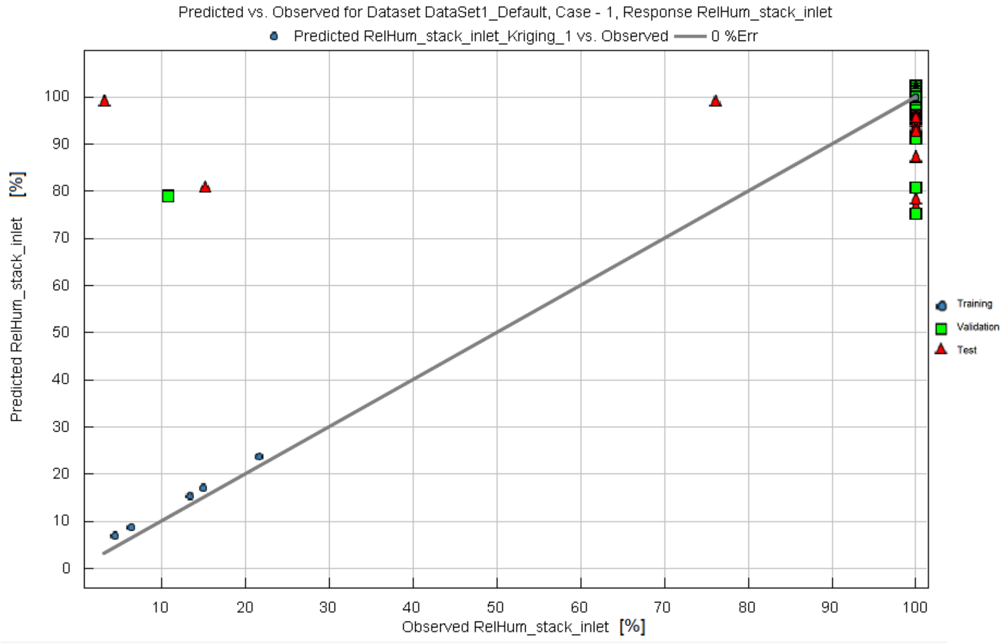

Figure 9.10: Simulated relative humidity vs. predicted relative humidity by the MLP

At 100 A the factors affecting the condensation rate in the mixing chamber and the mass flow rate of liquid water at the anode inlet of the stack the most were the hydrogen feed temperature, the anode stoichiometry, the cathode inlet temperature, and the coolant outlet temperature as shown in figures 9.5 and 9.7. As discussed before, the quality of the MLP for the condensation rate was very high. The MLP for the mass flow rate of liquid water at the inlet was of somewhat poorer quality. The R-squared values for the validation set and test set were still 0.75 and 0.87, respectively.

When evaluating the plot of the simulated condensation rate values versus the condensation rate predicted by the MLP at 100 A in figure 9.11, it is striking that the condensation rates are evenly distributed over the entire range.

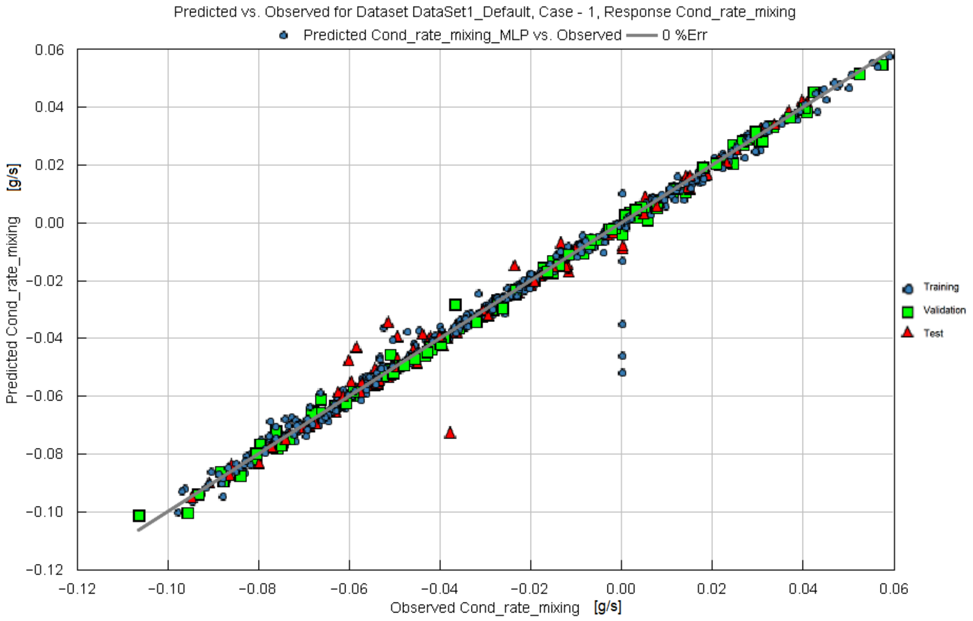

Figure 9.11: Simulated condensation rate vs. predicted condensation rate by the MLP

A visualization of the MLP metamodel for the condensation rate in the mixing chamber was rendered through a 2D contour in figure 9.12. The two most influential input parameters at 100 A on the condensation rate were the anode stoichiometry, and the hydrogen feed temperature. These were varied on the axes of the plot. The other input factors were fixed in the middle of their range specified in table 7.3.

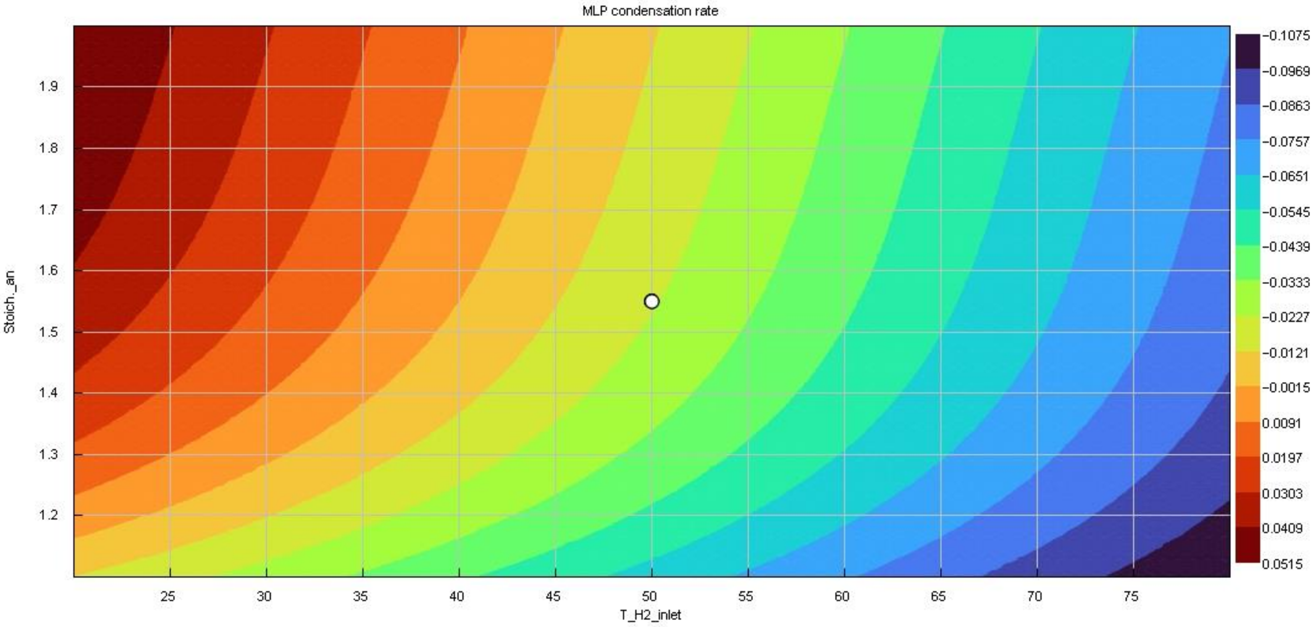

Figure 9.12: Visualization of the condensation rate MLP against the anode stoichiometry and hydrogen feed temperature

In figure 9.13, the simulated mass flow rates of liquid water at the anode inlet of the stack are plotted against the predicted mass flow rates by the MLP at 100 A. It is clear that most values of the mass flow rate of liquid water at the anode inlet in the simulated experiments at 100 A were in the range of 0.10 g/s to 0.25 g/s. At both ends of the range less data points were available.

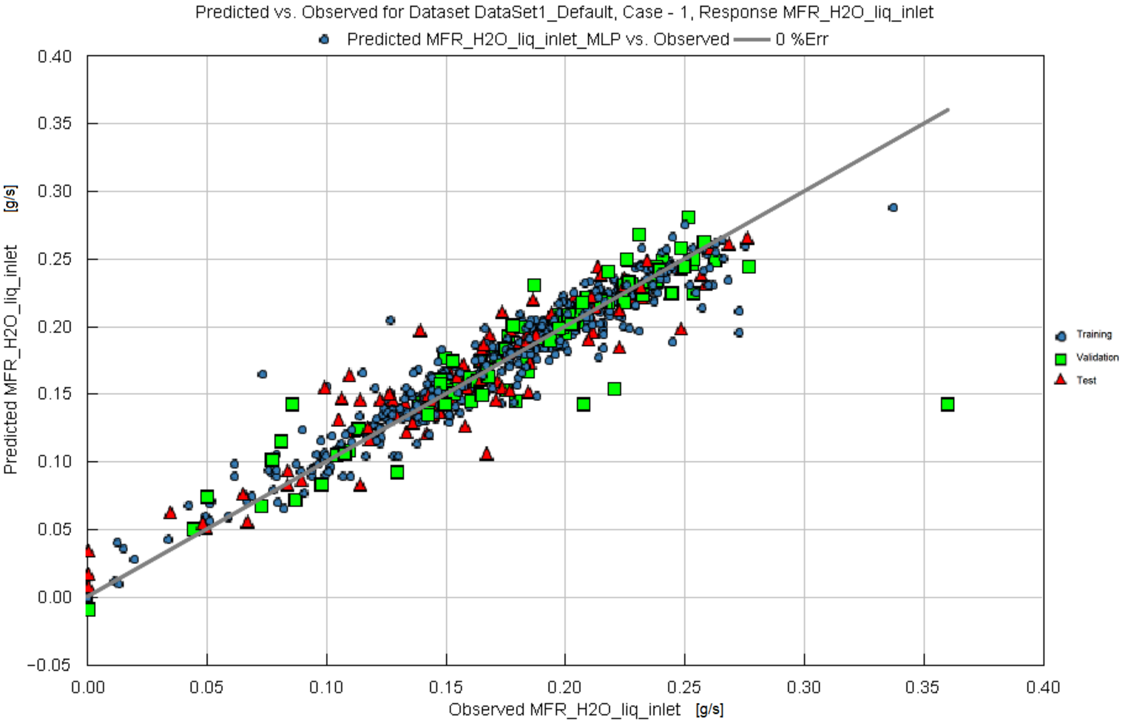

Figure 9.13: Simulated mass flow rate of liquid water at inlet vs. prediction by the MLP

Comparing figures 9.10, 9.11 and 9.13 it appears that a more evenly distributed values for a response in the simulated experiments allowed for the creation of more accurate metamodels. The R-squared values of those metamodels were higher and the RMS-errors were lower.

Optimization of MLP metamodels for responses at 100 A

As the MLP metamodels were of higher quality than their Kriging counterparts, they were chosen for further use in the optimizer tool. The simulated experiments in figure 9.10 showed that the relative humidity at the anode inlet of the stack was 100% regardless of the system operating parameters. Regarding the water management of the anode subsystem, minimizing the mass flow rate of liquid water at the anode inlet of the stack was therefore one of the objectives in the pareto multi-objective optimization. Furthermore, the condensation rate was targeted at 0 g/s as an objective. In this manner, no energy was wasted on evaporating water in the mixing chamber. The metamodels used in the optimizer tool were the MLP for the condensation rate and the MLP for the mass flow rate of liquid water at the anode inlet of the stack. The multi-objective pareto optimization for these two metamodels resulted in the following operating points in table 9.2.

Table 9.2: System operating parameters corresponding to pareto points at 100 A

Cond. Rate [g/s]	**MFR H_2O liq. [g/s]**	**Anode p_{inlet} [bar]**	**$T_{H2,inlet}$ [ºC]**	**$T_{cat.,dew.}$ [ºC]**	**$T_{cat.,in.}$ [ºC]**	**Stoich. Cat.**	**Stoich. An.**	**N_2 frac.**	**Δp [bar]**	**$T_{cool.,out.}$ [ºC]**
-2.5E-5	0.02	2.83	52.4	38.7	78.3	1.71	1.88	0.045	0.40	79.7
2.9E-4	7.7E-4	2.62	48.8	37.1	79.8	1.95	1.87	0.044	0.45	77.4
4.7E-5	0.01	2.52	50.2	36.9	77.8	1.73	1.65	0.034	0.16	77.7
6.9E-7	0.03	2.84	52.3	37.8	78.2	1.71	1.88	0.045	0.38	79.7
6-5E-3	9.4E-5	2.76	46.5	39.0	78.6	1.91	1.86	0.045	0.42	78.2
-7.5E-3	2.0E-5	2.62	52.2	36.9	79.8	1.93	1.85	0.044	0.45	77.4
-1.5E-3	8.1E-3	2.62	49.1	36.9	78.3	1.89	1.85	0.032	0.38	77.6
1.7E-4	6.2E-3	2.39	51.2	37.5	79.5	1.71	1.85	0.044	0.43	79.3

It should be noted that in order to minimize the mass flow rate of liquid water, the hydrogen fed to the system should be heated to a temperature of 48-53 ºC. Furthermore, the air at the cathode inlet should be fed at 78-80 ºC with a dewpoint temperature of 36-38 ºC. This corresponds to a relative humidity of approximately 15% at the anode inlet. The cathode stoichiometry should be between 1.7-1.9 and the anode stoichiometry should be between 1.8-1.9. The anode inlet pressure is between 2.3-2.8 bar with the cathode inlet pressure being approximately 0.4 bar lower. The coolant outlet temperature was about 77-80 ºC.

Kriging and MLP metamodels for responses at 300 A

The quality metrics of the metamodels created for the responses at 300 A are included in Appendix 4. Some of the most important findings from the evaluation of those metamodels are condensed in the subsequent paragraph.

The first metamodels to be evaluated were created for the mixing chamber condensation rate response. The MLP for the condensation rate was of very high quality with R-squared values above 0.9 for the training, validation, and test sets. The Kriging fared notably worse when the validation and test datasets were evaluated to assess the metamodel quality. The R-squared were below 0.7 for both sets. The Kriging and the MLP for the relative humidity at the anode inlet of the stack were of comparable quality. They outperformed the corresponding metamodels at 100 A, however. The metamodels for the temperature at the anode inlet, the mass flow rate of water vapor at the anode inlet, and the mass flow rate of liquid water at the anode outlet were all of mediocre quality with the MLPs consistently outperforming the Krigings. The metamodels for the mass flow rate of water vapor at the anode outlet of the stack were of low quality with the MLP still outperforming the Kriging. The kriging had R-squared values as low as 0.587 for the validation set and 0.496 for the test set. In contrast, the MLP for the mass flow rate of liquid water at the anode inlet was of high quality, with R-squared values above 0.9 for all sets. The Kriging performed reasonably as well with R-squared values above 0.84 in every set.

In figure 9.14, the relative humidity at the anode inlet of the stack in the simulated experiments is portrayed against the value predicted by the MLP at 300 A based on the parameters in table 7.3. Although in many simulations the relative humidity was 100%, the datapoints were more evenly distributed at 300 A than at 100 A. The R-squared values for this MLP were 0.871 for the training set, 0.605 for the validation set, and 0.759 for the test set.

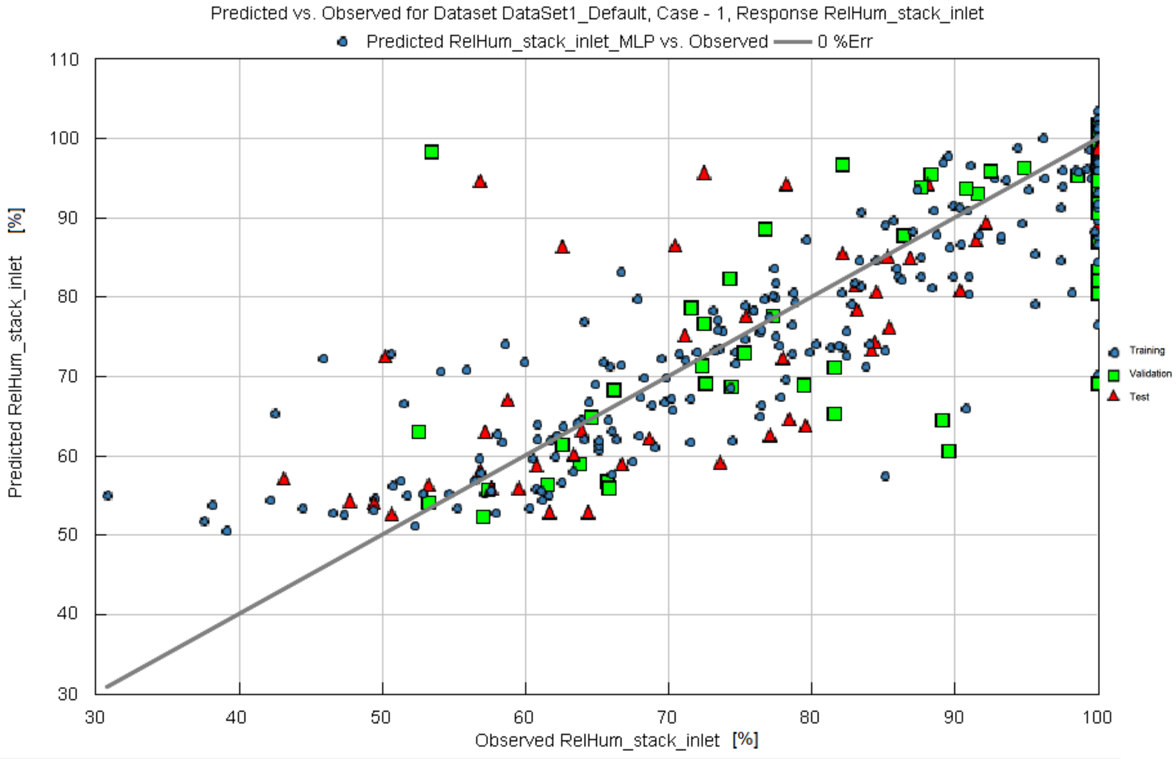

Figure 9.14: Simulated relative humidity vs. prediction by MLP at 300 A

The condensation rate in the mixing chamber in the simulated experiments at 300 A was plotted against the condensation rate predicted by the MLP in figure 9.15. The data is rather evenly distributed over the range from -0.3 to 0.3 g/s. The R-squared values for this MLP were 0.985 for the training set, 0.981 for the validation set, and 0.988 for the test set.

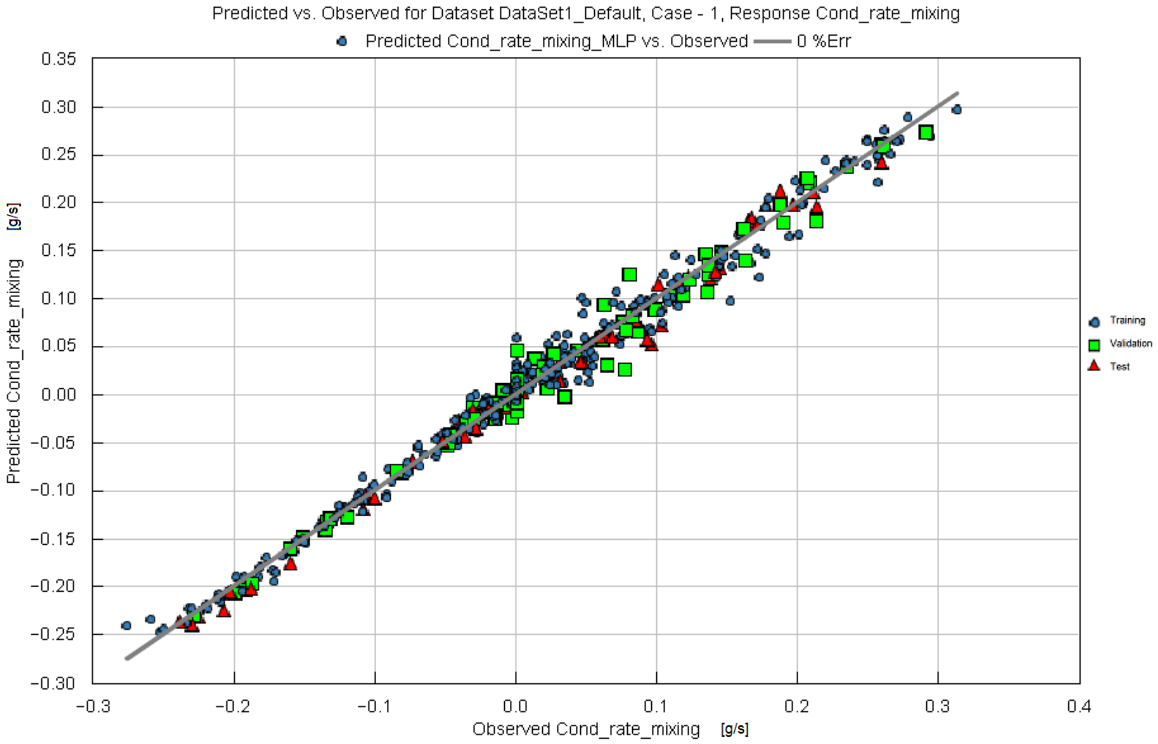

Figure 9.15: Simulated condensation rate vs. prediction by MLP at 3080 A

Optimization of MLP metamodels for responses at 300 A

Attaining a relative humidity of 60% at the anode inlet of the stack appeared attainable evaluating the simulated experiments in figure 9.15. The MLP for the anode inlet relative humidity was included in the optimizer tool and targeted at 60%. The R-squared values of this MLP were not very high. However, at a relative humidity around 60% an error not greater than 15 percent point was to be expected judging from figure 9.15. Furthermore, a condensation rate in the mixing chamber of 0 g/s was targeted. At a relative humidity of 60% no liquid water is present in the flow at the inlet of the stack. When no condensation occurs in the mixing chamber, the fresh hydrogen arrives at the right temperature to prevent condensation of water, but no energy is wasted on heating the hydrogen feed to a too high temperature leading to evaporation in the mixing chamber.

Table 9.3: System operating parameters corresponding to pareto points at 300 A

Rel. Hum. An. Inlet [%]	Cond. Rate [g/s]	Anode p_{inlet} [bar]	$T_{H2,inlet}$ [ºC]	$T_{cat.,dew.}$ [ºC]	$T_{cat.,in.}$ [ºC]	Stoich. Cat.	Stoich. An.	N_2 frac.	Δp [bar]	$T_{cool.,out.}$ [ºC]
60.0	8.9E-5	2.73	66.5	26.7	53.3	1.21	1.88	0.028	0.44	73.1
60.0	3.5E-4	2.01	56.6	29.3	60.1	1.24	1.99	0.028	0.23	77.9
59.9	3.1E-5	2.02	56.6	29.3	60.1	1.21	1.99	0.026	0.23	77.9
60.1	6.8E-7	2.74	66.4	26.6	53.3	1.21	1.88	0.028	0.45	73.1
60.0	9.9E-3	2.67	61.7	39.1	45.3	1.31	1.93	0.038	0.39	75.2
59.8	6.8E-3	2.01	56.6	28.8	76.7	1.25	1.99	0.028	0.23	78.0

In table 9.3, the pareto optimal operating points of the system are shown for the targets set in the optimizer. In these points the anode inlet pressure of the stack was in the range of 2.0-2.75 bar. The cathode inlet pressure was 0.2-0.4 bar lower than anode inlet pressure. The hydrogen was fed to the system at a temperature of 56-66 ºC. The temperature at which the air was fed to the stack showed a wide range from 45 to 76 ºC. The cathode inlet dewpoint was in the range of 26 to 30 ºC. The anode was operated at a high stoichiometry between 1.85 and 2.00. The cathode was operated at a relatively low stoichiometry between 1.20 and 1.35. The coolant outlet temperature was between 73 and 78 ºC.

10 Discussion of the results

The aim of this study was to identify in what manner the operating parameters and design of the PS100 system´s anode subsystem could be altered to improve its water management. This would result in a prolonged system lifetime and greater instantaneous power density. The purpose of this chapter is to interpret the results discussed in chapter 8 and 9 and to evaluate their significance. First the results regarding the metamodel for the water crossover will be discussed. Next, the effect of the system operating parameters on the responses in chapter 9 will be held under scrutiny. Here the method of evaluating the quality of the metamodels will be held under a light as well.

Water crossover mechanisms and modelling

In chapter 8, the results of the PEM fuel cell stack model regarding the predicted voltage and water crossover rate were presented. The T0042 dataset was used to insert 25 random measurement points into the case set-up of the PEM fuel cell stack model. The PEM fuel cell stack model was fitted to the measured voltages in these experiments using three parameters. These parameters were the tortuosity of the GDL, the catalyst specific surface area, and Springer's b_{11} coefficient. A multiplier of 0.5 as mentioned by Ye and Wang [34] was applied to the diffusive flux as a blanket solution to account for the reinforcement structure in the membranes used by PowerCell. The PEM fuel cell stack model did not allow to set different types of membrane or include a volume fraction of the reinforcement structure in the membrane. Even though the Vetter diffusion model should allow for a correction of the diffusion coefficient by the volume fraction of ionomer in the membrane, the PEM fuel cell stack model in GT-Suite had no such option. The water crossover models created on Nafion membranes assumed back-diffusion and electro-osmotic drag to be the dominant water transport mechanisms across membranes. These were also the only transport mechanisms included in the PEM fuel cell stack model. Further literature research pointed to the transport mechanism of thermo-osmosis to play a significant role in thin reinforced membranes, especially at higher currents. Perhaps, fitting the PEM fuel cell stack model both to the measured voltages and the measured water crossover rates could improve results regarding the predicted water crossover rates. As the relative humidity at the anode inlet of the stack was 100% at all times at 100 A, some liquid water was present in the stack at all times. In the water crossover models discussed in chapter 5, the assumption was made that little to no liquid water was present in the galvanic cell. This could make these models fundamentally unsuitable to describe the water crossover in a working fuel cell stack.

Upon evaluation of the T0042 dataset through the MEMP presented in figure 9.1, the anode inlet temperature had the greatest linear influence on the water crossover rate. It was negatively related to the water crossover rate, meaning a higher anode inlet temperature tended to imply a lower water crossover rate to the anode. The cathode inlet temperature was positively related to the water crossover rates recorded in T0042. In the water crossover models treated in chapter 5, the galvanic cell was considered isothermal. Unfortunately, the temperature difference between the anode and the cathode inlet flows was not taken as a parameter. This parameter would have provided more information about the influence of a temperature gradient across the membrane on the water crossover rate. The anode inlet being negatively related to the water crossover rate is however a strong indication that thermos-osmosis played a significant role in the experiments conducted by Bosch. In no other water transport mechanism a higher temperature would lead to a lower crossover rate. Additionally, the anode inlet pressure and the cathode inlet pressure had a positive and a negative relation to the water crossover rate, respectively. These parameters had a relatively small influence on the water crossover rate compared to the other parameters in table 7.1. Their influence was not negligible however. This gives rise to the suspicion that hydraulic permeation of water through the membranes could have played a role. To confirm this, the influence of the pressure difference between the anode and cathode inlet on the water crossover rate should be evaluated. The water crossover models discussed in chapter 5 were created on much thicker membranes than those used in the T0042 experiments. This could be a reason for the greater permeability of water in those membranes.

In figure 9.2, the quality of the Kriging created for the water crossover rate based on the T0042 dataset was evaluated. The predicted water crossover rates by the Kriging were plotted against the measured water crossover rates in T0042. This Kriging was trained on all the measurements in the T0042 dataset, except for the datapoints that were considered outliers. In discussion with the support engineers of Gamma Technologies it turned out that this was not the correct approach. Not all data should have been used as training data in the construction of the Kriging. It is common practise to assign 15% of the available data to a validation set and another 15% to a test set. These two sets are used to improve and finally test the created metamodel as shown in figure 7.7. When the Kriging was created assigning all datapoints as training points, the maximum percent error was approximately 15%. When the Kriging was retrained using the proper method, the validation and test set indicated that the metamodels performed worse than previously thought. In figures 10.1 and 10.2, the performance of the training set (blue), validation set (green) and the test set (red) are depicted.

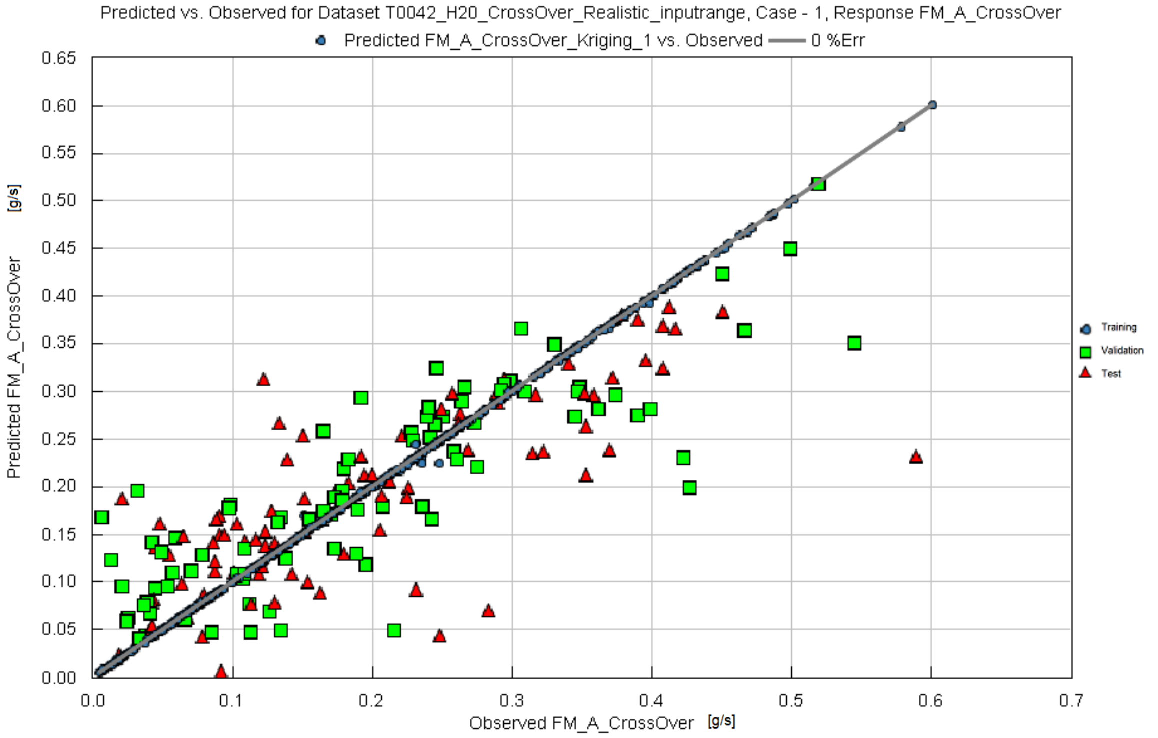

Figure 10.1: Measured crossover versus prediction by Kriging

In figure 10.2, it is shown that the crossover rates predicted by the Kriging often fall in a range which is 50% smaller to 100% greater than the crossover rate recorded in T0042. This is still a better performance than the literature water crossover models of the PEM fuel cell stack model provided as shown in figure 8.2 and Appendix 2. Some of the outliers had a much greater percentage error but these crossover rates were close to 0 g/s.

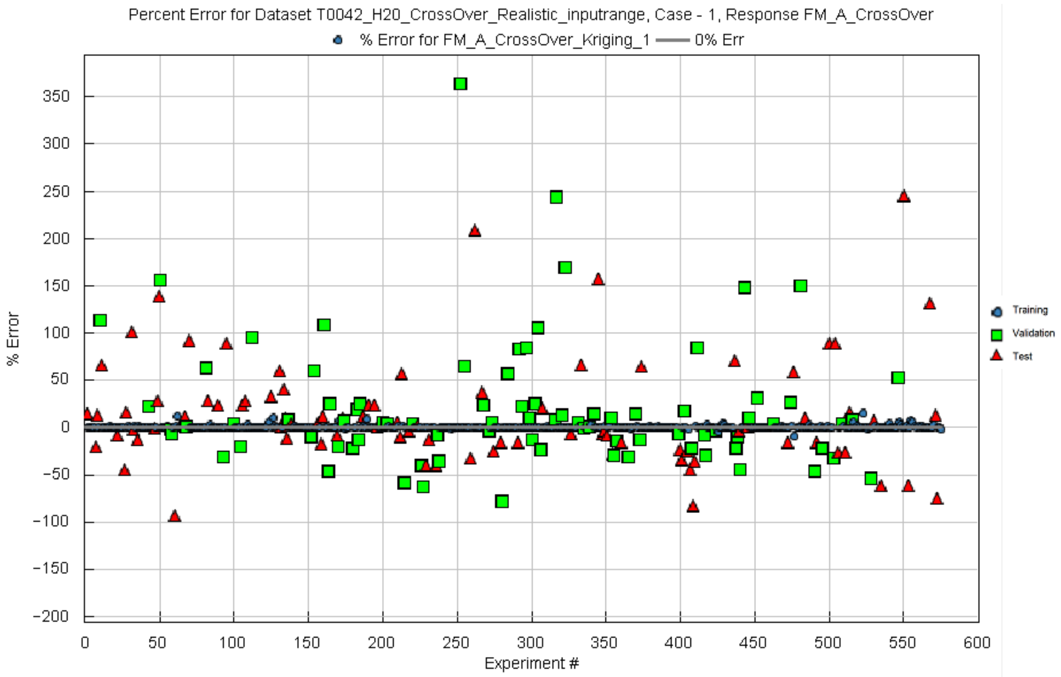

Figure 10.2: Percent error of measured crossover versus prediction by Kriging

The quality metrics of the Kriging for the water crossover rate are given in table 10.1. The Kriging was not able to capture the dataset well over the entire range as shown in figure 10.1.

Table 10.1: Quality metrics Kriging for water crossover rate

	R-squared	**RMS-error**	**Max. absolute error**	**Max. % error**
Training	0.999	0.00196	0.0226	15.4
Validation	0.709	0.0707	0.228	2656.7
Test	0.588	0.0784	0.356	812.4

Subsequently an MLP was created for the water crossover rate using the same method for comparison. The performance of this metamodel is visualized in figures 10.3 and 10.4.

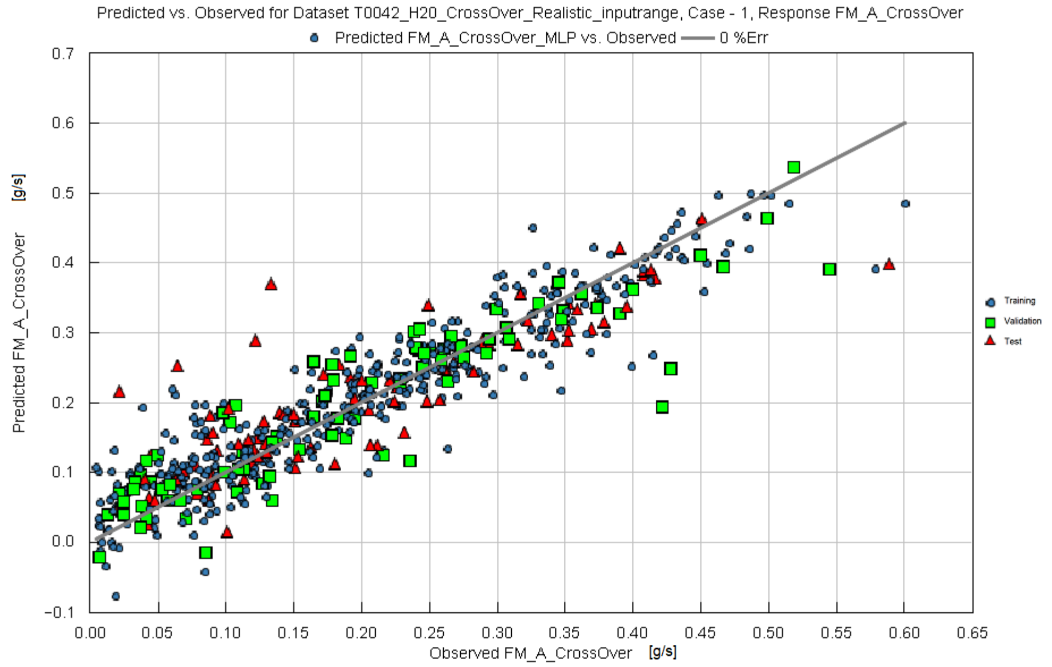

Figure 10.3: Measured crossover versus prediction by MLP

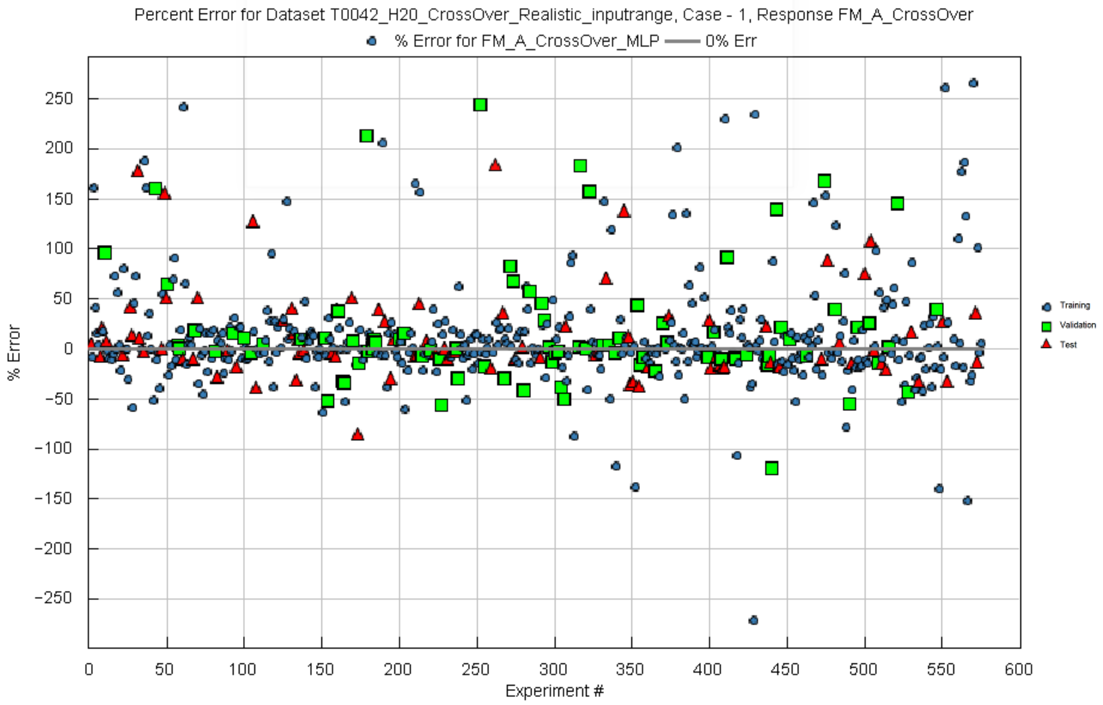

Figure 10.4: Percent error of measured crossover versus prediction by MLP

Comparing figure 10.1 to figure 10.3 it should be noted that the Kriging performed a lot better on the training set. The high performance on the training set is typical for Krigings, however. The MLP had higher values for the coefficient of determination in the validation and the test sets. The performance metrics of the MLP are given in table 10.2. It should be noted that the MLP performed a lot better than the Kriging in capturing the measured crossover rates in T0042. Also for the MLP the R-squared value for the test set was still rather low.

Table 10. 2: Quality metrics MLP for water crossover rate

	R-squared	**RMS-error**	**Max. absolute error**	**Max. % error**
Training	0.867	0.0471	0.188	2318.86
Validation	0.820	0.0555	0.228	446.96
Test	0.739	0.0624	0.238	953.15

The reason for the poor performance of both metamodels could be a large measurement error on the water crossover rates recorded in the T0042 dataset. When comparing the only two T0042 measurements which PowerCell had replicated, differences of 12.9% and 30% in the water crossover rate were observed. Unfortunately, no measurement error on the water crossover rate was provided by Bosch. A large error in the underlying water crossover data would also make it difficult to fit a metamodel on it. It is therefore recommended to conduct more experiments in which the water crossover rate is measured with greater accuracy. A literature study into water crossover measurement techniques should be conducted. As little recent research has been published on water crossover in reinforced membranes, a lumped model based on a dataset such as T0042 can give insight in the magnitude of the crossover to be expected at certain system operating conditions.

If a coupling between the processes within the stack and the system operating parameters were to be established, experiments on the material properties of PowerCell's membranes would be necessary as well. An example would be experiments in which the water sorption of the membranes used by PowerCell are related to the proton conductivity of the membranes. In this light, it would also be recommended to investigate the influence of the temperature difference on both sides of the membranes on the crossover rate. Especially in transient operation thermos-osmosis might play a greater role because the cathode catalyst layer will heat up or cool down due to the change in heat production. This heat will take some time to propagate, causing a greater thermal gradient at first.

Interpretation of the coefficient of determination

In assessing the quality of the metamodels the assumption was made that metamodels with T-squared values above 0.85 were of satisfactory quality. Now the water crossover metamodel integrated in the anode subsystem model was of lower quality than initially thought, there is reason to be suspicious of metamodels for responses with very high R-squared values such as the condensation rate in the mixing chamber. The responses such as the relative humidity at the anode inlet, the condensation rate, and the mass flow rates of water at the stack boundaries were dependent on the predicted water crossover rate by the Kriging. This means a high metamodel quality for these responses is meaningless as it just means that the metamodels were unaffected by the uncertainty in the output of the response. As the water crossover rate measurement recorded in T0042 had an unknown but likely great uncertainty, only indicative conclusions can be drawn from this study. The optimizations of the metamodels carried out in chapter 9 therefore have little value in establishing the actual operating parameters required but they do provide an indication of how the parameters can be tweaked to reach certain outcomes.

It seemed that metamodels built on a more evenly distributed dataset had higher coefficients of determination. A way to improve the metamodels could be by simulating additional operating points that will likely give results for responses in a sparse data zone.

Anode subsystem model improvements

Another source of uncertainty in the results presented in chapter 9, is the unknown separation efficiency of the vapor-liquid separator. This uncertainty affected the outcome of the mass flow rate of liquid water and water vapor at the anode inlet of the stack, the condensation rate in the mixing chamber, and the anode inlet relative humidity in simulated operating points. A constant high separation efficiency of 95% was assumed for the separator in the anode subsystem model. In reality, the separation efficiency depends on the geometry of the vapor-liquid separator and the operating parameters of the system. The model likely overestimated the separation efficiency of the separator when the anode subsystem was simulated at lower currents. At lower operating currents less hydrogen and water passed through the vapor-liquid separator. At lower mass flow rates, vapor-liquid separators are less successful in separating out liquid water. [12] This in turn, led to an underestimation of the liquid water mass flow rate and relative humidity at the inlet of the stack. A computational fluid dynamics (CFD) study on the vapor-liquid separators integrated in the anode subsystem should be carried out to achieve a more accurate representation of the composition of the flow further downstream.

For further improvement of the model as shown in figure 7.2 the cathode subsystem should be integrated as well to understand the influence of the operating parameters of the auxiliary systems in the cathode subsystem. The cathode operating parameters affect the water crossover rate and therefore also the water management of the anode subsystem. Vice versa, the anode operating parameters affect the water management of the cathode. Additionally, the influence of transient operation of the system should be investigated. When ramping up from a low to a high current, more hydrogen enters the anode subsystem. This pulse of hydrogen could carry away water from the stack but also decrease the humidity temporarily. When going from a high to a low current, water could aggregate in the gas flow channels of the stack. In these instances the stoichiometry could play role in alleviating potential flooding. In this capacity, it might also be relevant to investigate the purge strategy. The purge can also be used to drain water from the stack by suction. Perhaps the purge strategy could be optimized to prevent flooding at 100 A where the relative humidity of the anode inlet always appeared to be 100%.

Influence of the operating parameters on the responses

The influence of the system operating parameters specified in table 7.3 on the condensation rate in the mixing chamber, the relative humidity at the stack anode inlet, the temperature at the anode inlet of the stack, and the mass flow rate of water through the boundaries of the stack was assessed using MEMPs. A shortcoming of the MEMPs was that they only showed the linear effect of the system operating parameters on the corresponding response. No information could be about extracted from the MEMPs about the nature of the relationship between an operating parameter and the response. Furthermore, some parameters are not independent. A high coolant outlet temperature goes together with a high operating current for instance. It would be interesting to investigate the relationship between the operating parameters with respect to the responses.

The cathode inlet temperature had a surprising effect on the anode inlet temperature of the stack. It was increasingly negatively related to the anode inlet temperature with the current level. On the other hand the cathode inlet temperature was negatively related to the anode inlet relative humidity as well. This appears to be in conflict with the effect of the cathode inlet temperature on the anode inlet temperature of the stack. The cathode inlet temperature had a negative relationship with the mass flow rate of liquid water into the stack. This appears to contradict the positive relationship with the water crossover rate. The negative relationship became decreasingly pronounced with the current level. This does not support the hypothesis that thermos-osmosis would play a greater role at higher current levels.

From the MEMPs it became clear that the hydrogen feed temperature has a significant influence on the conditions at the anode inlet of the stack and the mixing chamber. Raising the hydrogen feed temperature lowered the relative humidity and decreased the mass flow rate of liquid water at the anode inlet. In order to prevent liquid water from entering the stack it would be beneficial to raise the temperature of the hydrogen before feeding it to the system. As seen in the optimizations at 100 A and 300 A, the temperature should be raised to 48-66 ºC. Assuming a constant heat capacity for hydrogen and a hydrogen storage temperature of 20 ºC, the heat requirement for heating the hydrogen to a certain temperature can be calculated with the following formula:

$$\dot{Q} = \dot{m}_{\mathrm{H}_2} c_p \Delta T \tag{10-1}$$

In relation (10-1), $\dot{m}_{\mathrm{H}_2}$is the mass flow rate of hydrogen fed to the system. c_p and ΔT are the heat capacity of hydrogen at constant pressure and the temperature rise, respectively. In case hydrogen would be fed at 2 g/s, which corresponds to operating the stack at the maximum current of 400 A, the heat requirement for heating the hydrogen feed from 20 ºC to 60 ºC, would be approximately 1.1 kW. This heat could be transferred to the hydrogen either by applying a heater on the hydrogen feed pipe or utilizing the waste heat of the stack in a heat exchanger. The most suitable heat exchanger would be a plate heat exchanger for its compactness. The heat exchanger could either use the coolant outlet of the stack or a compressor bleed in the cathode subsystem to bring the hydrogen to a higher temperature. A drawbacks of integrating a heat exchanger in the anode subsystem would be that it would complicate the system and the high capital cost of a heat exchanger. Furthermore, controlling the heat flow would not be easy. Furthermore, the plate heat exchanger would have a gas on one side of the plates and a liquid in case the coolant outlet is used. In case the cathode compressor bleed would be used this two-phase interface would be avoided. Plate heat exchangers with a gas on one side of the plates and a liquid on the other side are typically less durable. The drawback of a heater is the parasitic power loss but the benefit is the easy control of the amount of heat transferred to the hydrogen. The heat demand to heat up the hydrogen is small in comparison with the maximum power rating of the PS-100 system. Therefore, avoiding the cost of integrating a heat exchanger and the accompanying control structure in the anode subsystem might be a sensible choice. In the anode subsystem model in GT-Suite a heat supply can easily be added to the hydrogen feed pipe to evaluate the effect on the responses discussed in chapter 9. Subsequently, experiments should be carried out in which the hydrogen is heated to temperatures in the range specified in table 7.3 to monitor the effect on the dewpoint temperature at the inlet of the stack and the presence of liquid water at the inlet of the stack.

Improvements of the stack model

Another perspective from which the water crossover rate should be investigated is the stack design. An aspect which is not considered in the PEM fuel cell stack model in GT-Suite is the clamping force holding the cells of the stack in place. The clamping force does influence the water transport phenomena however as observed by Cha et al. [57] A higher clamping force gives rise to a more even water content distribution in the membrane, a lower contact resistance, and a lower Ohmic resistance as a consequence. The mass transfer potential loss also increases due to the reduced porosity of the electrodes under higher compression. Also the dimensions of the gas flow channels in the bipolar plates influence their ability to drain water. Furthermore, the physics of condensation in the pores of the gas diffusion layers should be investigated more thoroughly.

11 Conclusion and recommendations

In this chapter an answer to the research question posed in the introduction will be formulated. The aim of the research conducted in this thesis was to enhance the water management of the anode subsystem of PowerCell's PS-100 system. Proper water management of a PEM fuel cell system is twofold. On one hand the auxiliary systems should be operated in such a way that a sufficient relative humidity at the anode inlet of the stack is maintained for the membranes to be sufficiently hydrated to minimize the Ohmic losses during operation. On the other hand, minimizing the amount of liquid water entering the stack or forming in the stack is of vital importance to prevent flooding. When the auxiliary systems are not operated to facilitate sound water management, not only the stability of instantaneous operation is affected. In the long term, operating a PEM fuel cell system with the auxiliary system improperly adjusted leads to degradation of the stack. When the hydrogen is fed to the stack at too low of a relative humidity, cracks and pinholes can form in the membranes. When the electrodes are flooded on the other hand, liquid water enters the pores giving rise to corrosion of the carbon backbone of the MEAs.

Water crossover modelling

The aim in the literature review was to gain an understanding of the relevant principles and models regarding water crossover over the membranes. A number of water crossover models retrieved from literature sources were evaluated. These models took into account two transport mechanisms: electro-osmotic drag and back-diffusion. Both these transport mechanisms are affected by the cell temperature. A higher temperature induced a greater water flux for both mechanisms. Additionally, both mechanisms were affected by the membrane water content. The electro-osmotic drag coefficient and the diffusion coefficient increase with a greater membrane water content. This in turn gives rise to a higher flux for both mechanisms. The diffusive flux was furthermore affected by the thickness of the membrane. A thin membrane has a greater water concentration gradient than a thick membrane, which stimulates back-diffusion. Ye and Wang [34], found that a membrane reinforcement structure did not affect the electro-osmotic drag mechanism whereas back-diffusion was hampered by a reinforcement structure. The water flux as a consequence of electro-osmotic drag was also proportional to the current density. The models differed slightly in their approach to calculating the diffusion coefficient in the membrane, electro-osmotic drag coefficient, and the membrane water content.

Of the water crossover models discussed in the literature research, Nguyen's model incorporated the most conservative diffusion coefficient as it used the water activity on the interface of the anode catalyst layer and the membrane in calculating the membrane water content. This assumption was made because in the thick Nafion membranes the anode side of the membrane would dry at high currents. Ye and Wang [34] found that operating at higher currents increased the membrane hydration as a consequence of increased back-diffusion. Kulikovsky's [42] model appeared to describe water transport through the MEA in greatest detail. In the catalyst layer and the microporous layer of the MEA, Knudsen diffusion was considered unlike in other models. It should be noted that the models retrieved from the literature were all created with Nafion membranes as a basis. Little literature was found on the water transport in reinforced membranes such as those in use in PowerCell's stacks. Ye and Wang proposed correcting Zawodzinski's diffusion coefficient [20] with a correction factor accounting for the reinforcement structure which was 0.5. Barbir [9] proposed multiplying the diffusion coefficient of water in Nafion with a factor accounting for the ionomer volume fraction in reinforced membranes. The water crossover models of Springer, Vetter, Nguyen, Motupally and Kulikovsky were evaluated against 25 random datapoints from the T0042 dataset provided by Bosch and 11 datapoints measured in a test station at PowerCell's facilities. It turned out that the measured crossover rates and the predicted crossover rates by the literature models corrected for the reinforcement structure differed by 400% at times.

As a consequence of the poor performance of the models in predicting the crossover rates in PowerCell's stack, another approach towards predicting the crossover rate was taken. The T0042 dataset provided by Bosch was used to create a C-function which predicted the water crossover rate based on 10 input parameters. Analysing the T0042 dataset using a MEMP as shown in figure 9.1 it turned out that the current, anode stoichiometry, the cathode inlet dewpoint temperature, the coolant outlet temperature, the cathode inlet pressure of the stack, the cathode inlet temperature were positively related to the water crossover rate from the cathode to the anode. The anode inlet temperature of the stack, the cathode stoichiometry, the anode inlet pressure and the anode inlet dewpoint temperature were negatively related to the water crossover rate. The great linear influence of the anode inlet temperature gives rise to the suspicion that thermos-osmosis might play an important role in the water crossover in the MEAs used in PowerCell's stack. The negative linear effect of the anode inlet temperature on the water crossover rate agrees with Kim and Mench's [45] conclusion that thermos-osmosis occurs from the cold side of the membrane to the hot side. It also appeared that hydraulic permeation of water across the membranes cannot be neglected.

By analysing the effect of the temperature difference on the water crossover rate in the T0042 dataset, more insight can be on the thermos-osmosis. As the water crossover models investigated in the literature research are not capable of capturing the water crossover rates observed in the test station, creating metamodels on data acquired through crossover measurements in PowerCell's test station seems a viable way forward. The quality of the metamodel for the water crossover rate applied in the anode subsystem model in this study was not that high. This is in agreement with the great and unknown measurement error on the measured water crossover rates as recorded by Bosch in T0042. Likely, conducting water crossover measurements in PowerCell's test station with a known and small measurement error could aid in constructing better metamodels.

Influence of system operating parameters on water management

As proper anode water management entails maintaining sufficient humidification at the inlet of the stack while preventing flooding of the stack, the effect of the system operating parameters on the water management was investigated. In all responses which were held under scrutiny the effect of four system operating parameters stood out in the simulated experiments. These parameters were the hydrogen feed temperature, the coolant outlet temperature, the cathode inlet temperature, and the anode stoichiometry. The operating parameters were the most potent in the regulating the water management of the anode subsystem.

The relative humidity at the anode inlet of the stack was predominantly affected by the hydrogen feed temperature, the anode stoichiometry, and the cathode inlet temperature. These parameters were all negatively related to the relative humidity. At currents up till 150 A, the cathode inlet temperature had the strongest linear influence on the relative humidity. At higher currents, the anode stoichiometry and the hydrogen feed temperature had a much stronger negative relationship with the relative humidity. The anode stoichiometry, coolant outlet temperature, and cathode inlet temperature also had a negative influence on the mass flow rate of liquid water at the anode inlet of the stack. The hydrogen feed temperature had the strongest negative effect however.

The temperature at the anode inlet of the stack was mostly affected by the anode stoichiometry, the coolant outlet temperature, and the cathode inlet temperature. The anode stoichiometry and the coolant outlet temperature had a positive effect on the anode inlet temperature, whereas the cathode inlet temperature was negatively related to the anode inlet temperature.

The mass flow rate of water vapor at the anode inlet of the stack was positively related to the hydrogen feed temperature, the coolant outlet temperature and negatively related to the cathode inlet temperature. The mass flow rates of liquid water and water vapor at the anode outlet of the stack were most strongly affected by the anode stoichiometry, the coolant outlet temperature, and the cathode inlet temperature. The anode stoichiometry had a positive on the mass flow rate of water vapor at the outlet, whereas the effect on the liquid water mass flow rate was negative. The cathode inlet temperature had a negative effect on both the mass flow rate of liquid water and water vapor at the anode outlet of the stack. The coolant outlet temperature was negatively related to the mass flow rate of liquid water at the anode outlet and positively related to the mass flow rate of water vapor at the anode outlet.

Finally, the influence of the system operating parameters on the condensation rate in the mixing chamber was investigated. It turned out that the hydrogen feed temperature was increasingly negatively related to the condensation rate with the current level. The coolant outlet temperature and the anode stoichiometry were positively related to the condensation rate.

Upon evaluation of influence of the system operating parameters on the responses, it was discovered that the hydrogen feed temperature is a very potent operating parameter in regulating the anode subsystem water management which is currently not utilized in the PS-100 system. It can be used to prevent condensation in the mixing chamber and in controlling the relative humidity at the anode inlet of the stack. The system operating parameters were optimized in an optimizer tool for two operating points. In both the optimization at 100 A and the optimization at 300 A, the hydrogen feed temperature was at an elevated temperature compared to the storage temperature which is usually room temperature. It is therefore recommended to include an auxiliary system in the anode subsystem to heat the hydrogen fed to the PS-100. This could either be a simple heating element or a plate heat exchanger in which the waste heat of running the system is harvested.

Additionally, the anode stoichiometry had a great effect on the water management. This parameter is controlled through the mass flow rate of the recirculation compressor. The coolant outlet temperature can be controlled through the mass flow rate of the coolant circuit. Currently it is impossible to recommend a set of operating parameters for every operating current with accuracy due to the uncertainty in the water crossover rate measurements in T0042 and the low quality of the metamodels constructed on the simulated experiments.

Literature

[1] Katz, E. (2021). Electrochemical contributions: Christian Friedrich Schönbein (1799–1868). *Electrochemical Science Advances*, 2(1), https://doi.org/10.1002/elsa.202160007

[2] APS Physics. (2019). *October 1842: William Grove's letter to Faraday Describing a Fuel Cell*. https://www.aps.org/publications/apsnews/201909/history.cfm

[3] National Museum of American History. (2004). *Fuel Cell Origins: 1840-1890*. https://americanhistory.si.edu/fuelcells/origins/origins.htm

[4] National air and space museum. (n.d.). *Fuel Cell, Gemini*. https://airandspace.si.edu/collection-objects/fuel-cell-gemini/nasm_A19660646000

[5] Grubb, W. T. & Niedrach, L.W. (1960). Batteries with Solid Ion-Exchange Membrane Electrolytes: II. Low-Temperature Hydrogen-Oxygen Fuel Cells. *Journal of the Electrochemical Society, 107*

[6] Hall, E. (2019). *Powering Apollo 11: the fuel cell that took us to the moon*. University of Cambridge, Department of Chemical Engineering and Biotechnology. https://www.ceb.cam.ac.uk/news/powering-apollo-11-fuel-cell-took-us-moon

[7] NASA. (2010). *Fuel Cell Use in the Space Shuttle*. https://www.nasa.gov/topics/technology/hydrogen/fc_shuttle.html

[8] Wang, Y., Diaz, D.F.R., Chen, K.S., Wang, Z., Adroher, X.C. (2020). Materials, technological status, and fundamentals of PEM fuel cells – A review. *Materials Today, 32*, 178-203

[9] Barbir, F. (2013). *PEM Fuel Cells: Theory and Practise* (2nd edition). Academic Press

[10] Wei, H., Du, C. (2023). Active Disturbance Rejection-Based Performance Optimization and Control Strategy for Proton-Exchange Membrane Fuel Cell System. *Electronics*, 12(6), 1393

[11] Jenssen, D., Berger, O., Krewer, U. (2015) Anode flooding characteristics as design boundary for a hydrogen supply system for automotive polymer electrolyte membrane fuel cells. *Journal of Power Sources, 298*. 249-258

[12] Han, J., Feng, J., Chen, P., Liu, Y., Peng, X. (2022). A review of key components of hydrogen recirculation subsystems for fuel cell vehicles. *Energy Conversion and Management.*

[13] Wang, Y., Pellerin, M., Mohanty, P., Sengupta, S. (2017). Investigation of the flow phenomenon inside gas ejectors with moist gas entrainment. *Journal of Thermal Science and Engineering Applications*. *9*

[14] PowerCell Group. (n.d.). *Powercellution P stack*. Retrieved December 21, 2022, from https://powercellgroup.com/product/p-stack/

[15] Nafion. (n.d.). *Nafion™ sulfonic membranes*. Retrieved December 22, 2022, from https://www.nafion.com/en/products/sulfonic-membranes

[16] Fuller, T.F., Harb, J.N. (2018). *Electrochemical Engineering* (1st edition). Wiley

[17] Springer, T.E., Zawodzinski, T.A., Gottesfeld, S. (1991). Polymer Electrolyte Fuel Cell Model. *Journal of the Electrochemical Society, 138,* 2334-2342

[18] Mauritz, K.A., & Moore, R.B., State of understanding of nafion, *Chemical Reviews*, (10), 4535–4586 https://doi.org/10.1021/cr0207123

[19] Hsu, W.Y., & Gierke, T.D., Ion transport and clustering in nafion perfluorinated membranes, *Journal of Membrane Science*. (3), 307-326 https://doi.org/10.1016/S0376-7388(00)81563-X

[20] Zawodzinksi, T., Neeman, M., Sillerud, L., Gottesfeld, S. J. Phys. Chem., Submitted

[21] Weber, A.Z., & Newman, J., Transport in Polymer-Electrolyte Membranes: II. Mathematical Model, *Journal of the Electrochemical Society*, (151), A311 https://doi.org/10.1149/1.1639157

[22] Cleghorn, S., Kolde, J., Liu, W. (2003). *Catalyst coated composite membranes*. Wiley & Sons

[23] Bratsch, S.G., (1989), Standard Electrode Potentials and Temperature Coefficients in Water at 298.15 K, *J. Phys. Chem. Ref. Data., 18*(1) page 14

[24] Hołyst, R., Poniewierski, A. (2012). *Thermodynamics for Chemists, Physicists and Engineers*. Springer

[25] Zhang, J., Zhang, H., Wu, J., Zhang, J. (2013). *PEM fuel cell testing and diagnosis*. Burlington: Elsevier Science

[26] Wang, Y., Chen, K.S. (2013). *PEM Fuel Cells: Thermal and Water Management Fundamentals*. Momentum Press

[27] Zhao, J., Tu, Z., Chan, S.H. (2021). Carbon corrosion mechanism and mitigation strategies in a proton
exchange membrane fuel cell (PEMFC): A review. *Journal of Power Sources*. *488*. 1-14

[28] Sim, J., Kang, M., Min, K, Lee, E., Jyoung, J. (2022). Effects of carbon corrosion on proton exchange membrane fuel cell performance using two durability evaluation methods. *Renewable Energy*. *190*. 959-970

[29] O’Rourke, J., Ramani, M., Arcak, M. (2009). In situ detection of anode flooding of a PEM fuel cell. *International Journal of Hydrogen Energy, 34, 6765-6770*

[30] Zawodzinski, T.A, Davey, J., Valerio, J., Gottesfeld, S. (1995). The water-content dependence of electroosmotic drag in proton-conducting polymer electrolytes. *Electrochem. Acta. 40*, 297

[31] Janssen, G.J.M., Overvelde, M.L.J. (2001). Water transport in the proton exchange membrane fuel cell: measurements of the effective drag coefficient. *Journal of Power Sources*. *25*. 101-117

[32] DuPont. (n.d.) Product information DuPont™ Nafion® PFSA Membranes N-112, NE-1135, N-115, N-117, NE-1110 perfluorosulfonic acid polymer

[33] Büchi, F.N., Scherer, G.G. (2000). Investigation of the transversal water profile in Nafion™ membranes in polymer electrolyte fuel cells. *Journal of the Electrochemical Society. 148*. A181

[34] Ye, X., Wang, C. (2007). Measurement of Water Transport Properties Through Membrane-Electrode Assemblies: I. Membranes. *J. Electrochem. Soc*. 154 B676

[35] Vetter, R., Schumacher, J.O. (2019). Free open reference implementation of a two-phase PEM fuel cell Model. *Computer physics communications*. *234*. 223-234

[36] Mittelsteadt, C.K., Staser, J. (2011). Simultaneous Water Uptake, Diffusivity and Permeability Measurement of Perfluorinated Sulfonic Acid Polymer Electrolyte Membranes. *ECS Trans. 41*. 101-121

[37] Nguyen, T.V., White, R.E. (1993). A Water and Heat Management Model for Proton-Exchange-Membrane Fuel Cells. *Journal of the Electrochemical Society*. *140*. 2178-2186

[38] Fuller, T.H. (1992). Ph.D. Thesis. University of California, Berkeley, CA

[39] Motupally, S., Becker, A.J., Weidner, J.W. (2000). Diffusion of Water in Nafion 115 Membranes. *Journal of the Electrochemical Society*. *147*. 3171-3177

[40] Hinatsu, J.T., Mizuhata, M., Takenaka, H. (1994). *J. Electrochem. Soc.*, 141, 1493

[41] Activation energy. (2022, September 29). In *Britannica*. https://www.britannica.com/science/activation-energy

[42] Kulikovsky, A. A. (2019). *Analytical Modelling of Fuel Cells* (2^{nd} edition). Elsevier

[43] van Bussel, H.P.L.H., Koene, F.G.H., Mallant, R.K.A.M. (1998). Dynamic model of solid polymer fuel cell water management. *Journal of Power Sources*. 71. 218-222

[44] Manthiram, A., Zhao, X., Li, W. (2012). Functional Materials for Sustainable Energy Applications.

[45] Kim, S., Mench, M.M. (2009). Investigation of Temperature-Driven Water Transport in Polymer Electrolyte Fuel Cell: Phase Change-Induced Flow. *Journal of The Electrochemical Society*, 156 (3). B353-B362

[46] Kim, S., Mench, M.M. (2009). Investigation of temperature-driven water transport in polymer electrolyte fuel cell: Thermo-osmosis in membranes. *Journal of Membrane Science*. 328. 113–120

[47] Huang, K. J., Hwang, S.J., Lai, W.H. (2015). The influence of humidification and temperature differences between inlet gases on water transport through the membrane of a proton exchange membrane fuel cell. *Journal of Power Sources*. 284. 77-85

[48] Kim, Y.B. (2011). Study on the effect of humidity and stoichiometry on the water saturation of PEM fuel cells. *International Journal of Energy Research*. 36. 509-522

[49] Das, S. (n.d.). *Compressor Isentropic Efficiency: What, How, Several Types, Examples*. Lambda Geeks. https://lambdageeks.com/compressor-isentropic-efficiency/

[50] Díaz-Rodríguez, I.D., Han, S., Bhattacharyya, S.P. (2019) *Analytical design of PID controllers*. Springer

[51] Kleijnen, J.P.C. (2007). Kriging metamodeling in simulation: A review, *European Journal of Operational Research*, 192, 707–716

[52] Arrhenius equation. (2023, July 14). In *Brittanica*. https://www.britannica.com/science/Arrhenius-equation

[53] Tamouridou, A.A., Pantazi, X.E., Alexandridis, T., Lagopodi, A., Kontouris, G., Moshou, D. (2018). Spectral Identification of Disease in Weeds Using Multilayer Perceptron with Automatic Relevance Determination. *Sensors*. 18(9), 2770

[54] C3.ai. (n.d.). *Hyperparameters*. https://c3.ai/glossary/data-science/hyperparameters/

[55] C3.ai. (n.d.). *Root mean square error*. https://c3.ai/glossary/data-science/root-mean-square-error-rmse/

[56] Coefficient of determination. (2023, August 18). In *Brittanica*. https://www.britannica.com/science/coefficient-of-determination

[57] Cha, D., Ahn, J.H., Kim, H.S., Kim, Y. (2015). Effects of clamping force on the water transport and performance of a PEM (proton electrolyte membrane) fuel cell with relative humidity and current density. *Energy*. 93. 1338-1344

Appendix 1: Predicted voltage with optimized PEM fuel cell stack model

In table A1.1 below, the voltages predicted with the optimized PEM fuel cell stack model for the 25 data points from Bosch's T0042 dataset are compared against the measured voltages in the test station. The operating conditions at which the voltage measurements were taken, were inserted into the PEM fuel stack model in GT-Suite. In the final column the relative difference between the measured and the predicted voltage is given. This table holds the data which is represented visually in figure 8.1.

Table A1.1: Predicted voltage with Springer diffusivity model versus measured voltage

Experiment	**Current density [A/cm^2]**	**Measured voltage [V]**	**Predicted voltage [V]**	**Relative difference [%]**
1	0.018	17.76597	18.06078	1.659408
2	0.118	16.98651	16.1645	-4.83919
3	0.182	16.42583	16.0729	-2.14863
4	0.202094	16.36869	15.92594	-2.70486
5	0.277	13.28523	15.55039	17.05021
6	0.468	15.61409	15.25819	-2.27935
7	0.489	15.56085	15.36126	-1.28264
8	0.512992	15.07267	14.58432	-3.23997
9	0.546579	14.61579	14.58051	-0.24138
10	0.635474	14.48394	13.94892	-3.69388
11	0.686	14.93582	14.85927	-0.51253
12	0.785661	14.5203	14.1861	-2.30161
13	0.837	13.91058	13.56513	-2.48336
14	0.887115	14.57864	14.73809	1.093723
15	0.999	14.27162	14.22095	-0.35504
16	1.147	14.16342	14.49675	2.353457
17	1.161	13.45312	13.2462	-1.53808
18	1.19	13.89792	13.96804	0.504536
19	1.207	13.16278	13.36534	1.538885
20	1.341	13.34666	13.21167	-1.01141
21	1.388	13.13414	12.41874	-5.44687
22	1.492	11.69122	12.11407	3.616817
23	1.647	12.78995	12.84695	0.445662
24	1.741	11.50751	12.21036	6.107751
25	1.757	12.8228	13.09047	2.087454

Appendix 2: Predicted water crossover rate with the PEM fuel cell stack model

The water crossover rate predicted by the PEM fuel stack model with the five different diffusion coefficients is represented in table A2.1. It is compared with the measured value in for the water crossover rate in the test station by Bosch. The relative difference of the predicted value and the recorded value in the test station is given for every predicted value of the water crossover.

Table A2.1: Predicted water crossover per cell with Springer, Kulikovsky, Vetter, Nguyen, and Motupally diffusion coefficient compared to measured values by Bosch

Experiment	Bosch [g/s]	Springer [g/s]	Vetter [g/s]	Kulikovsky [g/s]	Nguyen [g/s]	Motupally [g/s]
1	0.00017	0.001027 (504.04 %)	0.000932 (447.84 %)	0.000955 (461.31 %)	0.000854 (402.10 %)	0.000967 (468.82 %)
2	0.000593	0.000843 (42.19 %)	0.000806 (36.00 %)	0.000864 (45.84 %)	0.00081 (36.65 %)	0.000843 (42.17 %)
3	0.005644	0.01228 (117.56 %)	0.009817 (73.92 %)	0.010561 (87.11 %)	0.009618 (70.40 %)	0.010221 (81.09 %)
4	0.006669	0.016826 (152.31 %)	0.011523 (72.79 %)	0.014206 (113.02 %)	0.010638 (59.51 %)	0.01332 (99.74 %)
5	-0.00062	0.001908 (-406.52 %)	0.000913 (-246.60 %)	0.002075 (-433.26 %)	-9E-05 (-85.51 %)	0.002247 (-460.88 %)
6	0.005245	0.000987 (-81.19 %)	0.000885 (-83.12 %)	0.001106 (-78.92 %)	0.000838 (-84.02 %)	0.001023 (-80.50 %)
7	0.001538	0.004431 (188.15 %)	0.003895 (153.31 %)	0.004662 (203.19 %)	0.003726 (142.32 %)	0.004394 (185.73 %)
8	0.001986	0.010617 (434.58 %)	0.008147 (310.20 %)	0.010397 (423.54 %)	0.006507 (227.65 %)	0.00976 (391.44 %)
9	0.004167	0.007253 (74.04 %)	0.006056 (45.32 %)	0.007525 (80.58 %)	0.005655 (35.70 %)	0.007018 (68.39 %)
10	0.00454	0.003612 (-20.43 %)	0.003383 (-25.48 %)	0.004181 (-7.90 %)	0.00318 (-29.96 %)	0.003921 (-13.63 %)
11	0.010274	0.024399 (137.49 %)	0.018209 (77.23 %)	0.020544 (99.97 %)	0.017128 (66.72 %)	0.020151 (96.15 %)
12	0.002914	0.00133 (-54.37 %)	0.000963 (-66.95 %)	0.001795 (-38.41 %)	0.000149 (-94.88 %)	0.001505 (-48.36 %)
13	0.008712	0.003871 (-55.56 %)	0.003247 (-62.73 %)	0.004482 (-48.56 %)	0.00261 (-70.04 %)	0.00405 (-53.52 %)
14	0.012287	0.021231 (72.79 %)	0.016193 (31.79 %)	0.021422 (74.34 %)	0.013949 (13.53 %)	0.020018 (62.91 %)
15	0.008591	0.020859 (142.79 %)	0.014869 (73.07 %)	0.02147 (149.90 %)	0.01106 (28.74 %)	0.019502 (127.00 %)
16	0.016091	0.040315 (150.54 %)	0.02691 (67.24 %)	0.037484 (132.95 %)	0.019518 (21.30 %)	0.036523 (126.98 %)
17	0.008771	0.009029 (2.95 %)	0.002685 (-69.39 %)	0.011239 (28.14 %)	-0.00079 (-108.97 %)	0.00873 (-0.46 %)

18	0.010795	0.002571 (-76.18 %)	0.001844 (-82.92 %)	0.003217 (-70.20 %)	0.000325 (-96.99 %)	0.002795 (-74.11 %)
19	0.012268	0.02467 (101.09 %)	0.011622 (-5.27 %)	0.025826 (110.51 %)	0.00353 (-71.23 %)	0.021881 (78.36 %)
20	0.013378	0.001122 (-91.62 %)	0.000582 (-95.65 %)	0.001556 (-88.37 %)	-0.0001 (-100.75 %)	0.001301 (-90.27 %)
21	0.018554	0.014294 (-22.96 %)	0.011955 (-35.56 %)	0.016132 (-13.05 %)	0.009604 (-48.23 %)	0.015309 (-17.49 %)
22	0.019487	0.042254 (116.83 %)	0.021704 (11.38 %)	0.041569 (113.32 %)	0.007723 (-60.37 %)	0.035813 (83.78 %)
23	0.01791	0.002409 (-86.55 %)	0.000232 (-98.70 %)	0.003805 (-78.76 %)	-0.00035 (-101.97 %)	0.002956 (-83.50 %)
24	0.011413	0.010297 (-9.79 %)	0.004318 (-62.16 %)	0.01288 (12.85 %)	0.000154 (-98.65 %)	0.010821 (-5.19 %)
25	0.022305	0.002668 (-88.04 %)	0.00115 (-94.85 %)	0.00347 (-84.44 %)	-0.00011 (-100.51 %)	0.002964 (-86.71 %)

In table A2.2, the measured water crossover rate per cell in the PowerCell test station is compared to the predicted values with the PEM fuel cell stack model.

Table A2.2: Predicted water crossover per cell compared to measured values by PowerCell

Experiment	**PowerCell [g/s]**	**Springer [g/s]**	**Vetter [g/s]**	**Kulikovsky [g/s]**	**Nguyen [g/s]**	**Motupally [g/s]**
220308 Op.v01 100A	0.011	-0.0008	-0.00109	-0.00046	-0.00122	-0.00069
220308 Op.v01 300A	0.0092	-0.00167	-0.00299	-0.00063	-0.00505	-0.0014
220310 Hot-dry 400A	0.0089	0.001018	-0.00066	0.001936	-0.00279	0.001097
220310 Hot 400A	0.0096	-0.00124	-0.00257	-0.00042	-0.00485	-0.00099
220308 Op.v01 550A	0.0191	-0.00136	-0.0033	-0.0005	-0.00338	-0.00122
220310 Hot 550A	0.0127	-0.00201	-0.00511	-0.00096	-0.00633	-0.00172
220310 Hot-dry 550A	0.0115	0.004194	-0.00263	0.006197	-0.00377	0.004724
220112 Op.v01 550A	0.0187	-0.00138	-0.0033	-0.0005	-0.00338	-0.00123
220112 T0042 440A	0.0240	0.001821	-0.00104	0.002932	-0.00178	0.002061
220112 Op.v01 300A	0.0089	-0.00168	-0.00304	-0.00063	-0.00512	-0.00142
220112 T0042 300A	0.009	-0.000094	-0.00068	0.000391	-0.00154	6.43E-05

Appendix 3: Metamodel quality at 100 A

This appendix holds tables with information regarding the metamodel quality for the following responses at 100 A: the condensation rate in the mixing chamber, the relative humidity at the anode inlet of the stack, the temperature at the anode inlet of the stack, the mass flow rates of water vapor into and out of the stack, and the mass flow rates of liquid water into and out of the stack.

Table A3.1: Metamodel quality for condensation rate mixing chamber

Kriging condensation rate in the mixing chamber				
	R^2	**RMS-error**	**Max. absolute error**	**Max. % error**
Training	0.999	8.45 E-6	5.96 E-5	100.0
Validation	0.951	0.00860	0.0245	309.96
Test	0.922	0.00992	0.0305	231.96
MLP condensation rate in the mixing chamber				
	R^2	**RMS-error**	**Max. absolute error**	**Max. % error**
Training	0.986	0.00430	0.0519	8009.24
Validation	0.997	0.00217	0.00884	290.88
Test	0.980	0.00505	0.0343	125.81

Table A3.2: Metamodel quality for relative humidity at the anode inlet of the stack

Kriging relative humidity at the anode inlet of the stack				
	R^2	**RMS-error**	**Max. absolute error**	**Max. % error**
Training	0.999	0.00225	0.0244	0.56
Validation	0.0944	8.37	82.2	764.27
Test	0.0704	12.3	96.4	3097.78
MLP relative humidity at the anode inlet of the stack				
	R^2	**RMS-error**	**Max. absolute error**	**Max. % error**
Training	0.903	2.80	44.6	707.55
Validation	0.816	3.78	28.3	263.60
Test	0.182	11.5	97.4	3128.84

Table A3.3: Metamodel quality for temperature at the anode inlet of the stack

Kriging temperature at the anode inlet of the stack				
	R^2	**RMS-error**	**Max. absolute error**	**Max. % error**
Training	0.999	0.00203	0.0119	0.0306
Validation	0.895	2.60	10.4	32.1
Test	0.903	2.60	10.7	31.4
MLP temperature at the anode inlet of the stack				
	R^2	**RMS-error**	**Max. absolute error**	**Max. % error**
Training	0.993	0.656	8.68	22.3
Validation	0.990	0.785	6.92	13.9
Test	0.982	1.13	7.76	15.2

Table A3.4: Metamodel quality for water vapor mass flow rate at the anode inlet of the stack

Kriging mass flow rate of water vapor at the anode inlet of the stack				
	R^2	**RMS-error**	**Max. absolute error**	**Max. % error**
Training	0.999	0.00287	0.0176	64.82
Validation	0.767	0.108	0.421	1285.02
Test	0.696	0.138	0.694	6603.55
MLP mass flow rate of water vapor at the anode inlet of the stack				
	R^2	**RMS-error**	**Max. absolute error**	**Max. % error**
Training	0.886	0.0821	0.642	2428.41
Validation	0.908	0.0677	0.477	1480.55
Test	0.883	0.0855	0.675	6419.37

Table A3.5: Metamodel quality for liquid water mass flow rate at the anode inlet of the stack

Kriging mass flow rate of liquid water at the anode inlet of the stack				
	R^2	**RMS-error**	**Max. absolute error**	**Max. % error**
Training	0.999	1.01 E-4	5.04 E-4	100.00
Validation	0.630	0.0332	0.223	100.00
Test	0.757	0.0291	0.100	228.90
MLP mass flow rate of liquid water at the anode inlet of the stack				
	R^2	**RMS-error**	**Max. absolute error**	**Max. % error**
Training	0.922	0.0152	0.0916	221.60
Validation	0.742	0.0277	0.217	100.0
Test	0.876	0.0207	0.0600	100.0

Table A3.6: Metamodel quality for water vapor mass flow rate at the anode outlet of the stack

Kriging mass flow rate of water vapor at the anode outlet of the stack				
	R^2	**RMS-error**	**Max. absolute error**	**Max. % error**
Training	0.999	1.69 E-4	9.69 E-4	1.61
Validation	0.802	0.107	0.426	362.45
Test	0.774	0.121	0.497	201.55
MLP mass flow rate of water vapor at the anode outlet of the stack				
	R^2	**RMS-error**	**Max. absolute error**	**Max. % error**
Training	0.904	0.0788	0.658	1349.89
Validation	0.932	0.0629	0.422	402.65
Test	0.948	0.0579	0.464	191.73

Table A3.7: Metamodel quality for liquid water mass flow rate at the anode outlet of the stack

<table>
<tr><th colspan="5">Kriging mass flow rate of liquid water at the anode outlet of the stack</th></tr>
<tr><th></th><th>R^2</th><th>RMS-error</th><th>Max. absolute error</th><th>Max. % error</th></tr>
<tr><td>Training</td><td>0.999</td><td>3.16 E-4</td><td>0.00187</td><td>100.00</td></tr>
<tr><td>Validation</td><td>0.789</td><td>0.404</td><td>1.72</td><td>220.43</td></tr>
<tr><td>Test</td><td>0.691</td><td>0.545</td><td>1.71</td><td>4699.35</td></tr>
<tr><th colspan="5">MLP mass flow rate of liquid water at the anode outlet of the stack</th></tr>
<tr><th></th><th>R^2</th><th>RMS-error</th><th>Max. absolute error</th><th>Max. % error</th></tr>
<tr><td>Training</td><td>0.937</td><td>0.223</td><td>1.30</td><td>1755.88</td></tr>
<tr><td>Validation</td><td>0.912</td><td>0.261</td><td>0.763</td><td>100.0</td></tr>
<tr><td>Test</td><td>0.866</td><td>0.359</td><td>1.05</td><td>262.78</td></tr>
</table>

Appendix 4: Metamodel quality at 300 A

This appendix holds tables with information regarding the metamodel quality for the following responses at 300 A: the condensation rate in the mixing chamber, the relative humidity at the anode inlet of the stack, the temperature at the anode inlet of the stack, the mass flow rates of water vapor into and out of the stack, and the mass flow rates of liquid water into and out of the stack.

Table A4.1: Metamodel quality for condensation rate mixing chamber

Kriging condensation rate in the mixing chamber &				
	R^2	**RMS-error**	**Max. absolute error**	**Max. % error**
Training	0.999	5.90 E-5	2.13 E-4	100.00
Validation	0.679	0.0603	0.159	8614.07
Test	0.699	0.0565	0.182	1402.93
MLP condensation rate in the mixing chamber &				
	R^2	**RMS-error**	**Max. absolute error**	**Max. % error**
Training	0.985	0.0129	0.0598	861.05
Validation	0.981	0.0147	0.0505	795.56
Test	0.988	0.0112	0.0427	100.00

Table A4.2: Metamodel quality for relative humidity at the anode inlet of the stack

Kriging relative humidity at the anode inlet of the stack &				
	R^2	**RMS-error**	**Max. absolute error**	**Max. % error**
Training	0.999	0.0197	0.102	0.223
Validation	0.527	10.2	40.0	57.3
Test	0.692	9.78	37.7	66.4
MLP relative humidity at the anode inlet of the stack &				
	R^2	**RMS-error**	**Max. absolute error**	**Max. % error**
Training	0.871	6.00	29.7	78.7
Validation	0.605	9.29	45.1	84.4
Test	0.759	8.66	38.1	67.1

Table A4.3: Metamodel quality for temperature at the anode inlet of the stack

Kriging temperature at the anode inlet of the stack &				
	R^2	**RMS-error**	**Max. absolute error**	**Max. % error**
Training	0.999	0.0131	0.0693	0.0951
Validation	0.612	8.67	27.1	76.6
Test	0.581	8.48	24.2	54.8
MLP temperature at the anode inlet of the stack &				
	R^2	**RMS-error**	**Max. absolute error**	**Max. % error**
Training	0.926	3.99	21.2	31.4
Validation	0.827	5.79	23.4	45.8
Test	0.752	6.52	25.0	56.6

Table A4.4: Metamodel quality for water vapor mass flow rate at the anode inlet of the stack

Kriging mass flow rate of water vapor at the anode inlet of the stack &				
	R^2	**RMS-error**	**Max. absolute error**	**Max. % error**
Training	0.999	0.00117	0.00490	0.516
Validation	0.618	0.719	1.61	423.0
Test	0.476	0.813	2.21	338.5
MLP mass flow rate of water vapor at the anode inlet of the stack &				
	R^2	**RMS-error**	**Max. absolute error**	**Max. % error**
Training	0.870	0.438	2.10	160.0
Validation	0.775	0.552	2.02	214.5
Test	0.667	0.648	2.79	311.0

Table A4.5: Metamodel quality for liquid water mass flow rate at the anode inlet of the stack

Kriging mass flow rate of liquid water at the anode inlet of the stack &				
	R^2	**RMS-error**	**Max. absolute error**	**Max. % error**
Training	0.999	4.21 E-5	2.45 E-4	100.0
Validation	0.847	0.0371	0.127	915.1
Test	0.864	0.0308	0.110	3676.6
MLP mass flow rate of liquid water at the anode inlet of the stack &				
	R^2	**RMS-error**	**Max. absolute error**	**Max. % error**
Training	0.940	0.0229	0.0938	11110.2
Validation	0.913	0.0279	0.137	987.0
Test	0.918	0.0240	0.0948	1977.7

Table A4.6: Metamodel quality for water vapor mass flow rate at the anode outlet of the stack

Kriging mass flow rate of water vapor at the anode outlet of the stack &				
	R^2	**RMS-error**	**Max. absolute error**	**Max. % error**
Training	0.999	6.51 E-4	0.00263	0.449
Validation	0.587	0.771	1.90	538.8
Test	0.496	0.826	2.43	363.9
MLP mass flow rate of water vapor at the anode outlet of the stack &				
	R^2	**RMS-error**	**Max. absolute error**	**Max. % error**
Training	0.870	0.452	2.19	204.0
Validation	0.764	0.584	2.33	289.1
Test	0.665	0.673	2.78	337.9

Table A4.7: Metamodel quality for liquid water mass flow rate at the anode outlet of the stack

Kriging mass flow rate of liquid water at the anode outlet of the stack				
	R^2	**RMS-error**	**Max. absolute error**	**Max. % error**
Training	0.999	0.00163	0.00806	0.769
Validation	0.545	0.876	2.88	264.1
Test	0.564	0.851	2.84	160.1
MLP mass flow rate of liquid water at the anode outlet of the stack				
	R^2	**RMS-error**	**Max. absolute error**	**Max. % error**
Training	0.938	0.337	2.14	260.2
Validation	0.802	0.577	2.54	144.1
Test	0.662	0.748	3.34	205.7